3D visualization and characterization of the early bone metastatic niche: from cancer cell homing to small osteolytic lesions

Inaugural-Dissertation
to obtain the academic degree
Doctor rerum naturalium (Dr. rer. nat.)

submitted to the Department of Biology, Chemistry, Pharmacy
of Freie Universität Berlin

by

SARAH ANN ELISABETH YOUNG

2022

The work was performed from the 01.12.2018 until the 22.08.2022 at the

Max-Planck-Institute of Colloids and Interfaces

under the supervision of

Dr. Amaia Cipitria

1st reviewer: Dr. Amaia Cipitria

2nd reviewer: Prof. Petra Knaus

Date of defense: 29.11.22

Acknowledgments

At first I would like to express my gratitude for having the chance to perform my research at the Max Planck Institute of Colloids and Interfaces. I have always valued the interdisciplinary culture of the MPS and it was great to work in such a vibrant and supporting institute during my PhD. I hope that fundamental research, like I was allowed to do, will always have a home in the MPS.

My thanks go to my supervisor Amaia, who came up with this interesting project and supported me in reaching for the stars. It was great to work with you and I hope that you will never loose your passion for research!

I would like to thank Peter for letting me work in his department and being my mentor, as well as Petra for being my university supervisor. My thanks go to Claudia, who took over the role as mentor to support the thesis and to Georg, who was always there for discussions and supported this research by letting us use the facilities of the JWI and BCRT. My thanks also go to Angelo, who supported me with the statistics that always give me a little headache.

I also want to thank Bettina and Anika, my two amazing collaborators. You are both such great role models. It's impressive how much you know and how openly you share this knowledge, while constantly making sure that you keep on encouraging the people you work with. Both of you made me believe in science again, even when I was close to giving up on it sometimes.

As science is always a collaborative effort and gets the best result when working as a team, I would like to thank all the people in the AG Cipitria. Sadra it was great to sit in the office with you, I enjoyed our discussions, scientific, or about god and the world. Thank you for your wisdom and all the great papers you have recommended to me. Of course the discussions were the best, when you, Hubert joined us. Thank you for being such a positive and energetic colleague. My thanks also go to Anna and Aline, you were both great at supporting me in very different phases of this thesis and I couldn't have done it without you. I also want to thank Claudia and Vikki, it was great working with you and all the other people in the team.

Without the support, uplift and commitment of the following two people, I would have never been able to do this PhD. Daniela thank you so much for doing the animal work with me. It is great to know that I could always count on you. And thank you as well Jeannette, for helping me many hours in the lab doing stainings, through very frustrating and successful times. You allowed me to keep going! I

also want to thank Susann, Birgit, Daniel and Christine for teaching me many things and for helping me out during my lab work.

As the mouse work was one of the main challenges during this PhD, I would like to thank Agnes for supporting us. Your direct and open communication was always very appreciated and it was great to learn from you. I also want to thank Katja, Mario and Andrea, who all made this tough work much easier and where always there when I needed a helping hand or a kind word.

My PhD would not have been the same without many people at the MPICI over these four years. Starting with my italian office mates Agnese and Laura, who brought me italian summer vibes every day. Victoria and Max, who spent many Amira breaks and discussions with me. A special thanks to Victoria, who shared her food with me during long confocal nights and I always enjoyed our evening walks. I also want to thank Cathleen and Elisa, who were there for me at the start of my PhD and to Emeline who gave me so much good advice towards the end of my PhD. I am really happy to have worked with Macarena, who I just met recently but I already cannot image my coffee breaks without you anymore. Thanks to all the people in the biomaterials department, especially the PhDs and Postdocs and to some friends from other groups I have made over the years. You make this institute the special place that it is.

Aside from the science, my true passion during this PhD was my work for the Max-Planck PhDnet. I got to know so many amazing people during that time, especially in my second year at the N^2 network. My thanks go to Conny and Lindsey, the PhDnet queen and good cop Lea, my friend from N^2 Ivona and of course to Ilka. I feel so blessed that I got to meet and work with all of you.

I also want to thank my good friends Kathi, Franzi, Inga, Manu, Peter and Simon. Although we are all at different places and points now, I cherish our friendship and I know that I can always count on you.

A special thank you goes to Anna for being my friend in Potsdam from the very beginning, for always having an open ear and supporting me through every crisis.

I want to thank my family, my mum for being my rock, my dad, my brother and my Oma for believing in me and supporting me.

Lastly, my thanks go to Outman. You have been my constant in this stressful, amazing and eventful time. Thank you for cooling me down when I go crazy and for lifting me up when I feel like drowning. It wouldn't have been the same without knowing that you always have my back.

Selbstständigkeitserklärung

zur Abschlussarbeit

Hierdurch versichere ich, dass ich meine Dissertation selbstständig verfasst und keine anderen als die von mir angegeben Quellen und Hilfsmittel verwendet habe.
Diese Arbeit hat in gleicher oder ähnlicher Form noch keiner anderen Prüfungsbehörde vorgelegen und wurde bisher nicht veröffentlicht.

_____

Datum, Name

Contents

List of Figures

List of Tables

Glossary

α-SMA alpha-smooth muscle actin. 87

BMP bone morphogenetic protein. 11

BS/BV bone surface over bone volume. 13, 33, 51

BSA bovine serum albumin. 39

BSE backscattered electron. VIII, 9, 23, 38, 71–73, 88, 137, 140

BV bone volume. 13, 33, 48, 51

BV/TV bone volume fraction. 13, 33

CI confidence interval. 31

CLSM confocal laser scanning microscopy. VIII, IX, XII, 9, 13, 23, 37, 39, 40, 64, 68–73, 85, 86, 88, 93, 137, 140

CTC circulating tumor cell. 80–82, 86

DAPI 4',6-diamidino-2-phenylindole. 39, 64, 68–70, 135

DMEM Dulbecco's Modified Eagle's Medium. 26

DMSO dimethyl sulfoxide. 39

ECM extracellular matrix. IX, 7–9, 19, 69, 71, 75, 86, 87, 91

eGFP green fluorescent protein. XII, 26, 34, 39, 64, 68–70, 85, 135

ER oestrogen receptor. 15

ES_{CB}/BS normalized eroded bone surface-to-constant bone interface. 28–30, 44–46, 50, 54, 76

ES_{ST}/BS normalized eroded bone surface-to-soft tissue interface. 28–30, 44–46, 50, 76

ES/BS normalized eroded bone surface. 14, 56, 77, 134

EV/BV normalized eroded bone volume. 14, 28, 46–48, 52, 54, 56, 134

FN fibronectin. IX, X, XII, 2, 8, 23, 24, 39, 69–71, 75, 86, 87, 91

H&E haematoxylin and eosin. VIII, 36, 71, 72, 137

HER2 human epidermal growth factor receptor 2. 15

HSC haematopoetic stem cell. XI, 6, 7, 19, 20

IF immunofluorescence. VIII, 23, 24, 39, 40, 69, 85, 86

LSFM light-sheet fluorescence microscopy. VIII, IX, XII, 2, 9, 10, 21, 23, 24, 34, 40, 64, 67–69, 84, 90, 93, 140

MAR 3D mineral apposition rate. 14, 28, 48, 50, 52, 54, 56, 76, 78, 79, 134

. 11

MEA 2-methoxyethyl acetate. 36, 37

microCT microcomputed tomography. VII–X, 1, 9, 13, 14, 23–26, 29, 31, 33–35, 40, 43, 46, 48, 50–53, 57, 60, 64, 67, 75–83, 85–89, 91, 93, 121, 122, 124, 126, 128, 130–132, 140

MRR 3D mineral resorption rate. 14, 28, 50–54, 56, 78–80, 134

MS_{CB}/BS normalized mineralized bone surface-to-constant bone interface. 28–30, 44, 45, 50, 51, 54, 56, 76

MS_{ST}/BS normalized mineralized bone surface-to-soft tissue interface. 28–30, 44–46, 51, 54, 56, 76

MS/BS normalized mineralized bone surface. 14, 56, 134

MSC mesenchymal stem cell. XI, 6, 7

MV/BV normalized newly mineralized bone volume. 14, 27, 46–48, 51, 52, 54, 56, 134

OPG osteoprotegerin. 11, 20

PBS phosphate buffered saline. 23, 25–27, 34, 39, 53, 54, 56, 68, 69, 81, 82

PE$_{CV}$ precision error as coefficient of variation. 31

PE$_{SD}$ absolute precision error. 31

PFA paraformaldehyde. 26

PMMA poly(methyl methacrylate). 35–38

PR progesterone receptor. 15

PTHrP parathyroid hormone-related protein. 81

RANK receptor activator of nuclear factor-κB. 11

RANKL receptor activator of nuclear factor-κB ligand. 11, 20, 81

RGD arginine-glycine-aspartic acid. 8

ROI region of interest. XIII, 27, 30, 38, 46, 48, 52, 77, 78, 89, 123–129

ROIs regions of interest. 27, 53

RUNX2 runt-related transcription factor 2. 11, 84

SD standard deviation. 31

SHG second harmonic generation. VIII, 9, 38, 40, 71, 72, 88, 137, 140

TRAP tartrate-resistant acid phosphatase. VIII, 37, 140

TV total volume. 13, 33, 50, 51

Wnt wingless. 11

Abstract

Breast cancer is one of the main cancer-associated causes of death in women. While a primary tumor can often be treated well, metastases have a very poor prognosis and the spread to bones is among the most frequent forms of metastasis with very poor outcome. While the cellular involvement of late-stage metastasis in the bone has been studied frequently, early metastatic lesions and associated structural and biophysical parameters, as well as the dynamic bone (re)modeling behavior are not well understood. We hypothesize, that such structural and biophysical changes in the bone microenvironment, influence the establishment and progression of breast cancer induced osteolytic lesions.

Hence, we aim to develop an experimental mouse model of breast cancer bone metastasis to detect and characterize early osteolytic lesions in 3D.

In order to study the dynamic bone (re)modeling behavior in a pathological model, a physiological baseline has to be established. *In vivo* microCT-based time-lapse morphometry is a powerful tool to study temporal and spatial changes in bone (re)modeling. Here we present an advancement of the method to detect and quantify site-specific differences of bone (re)modeling in 12-week-old female BALB/c nude mice. We establish new bone surface interface parameters and show how they are affected by bone curvature. Significant differences in bone (re)modeling baseline parameters between metaphysis and epiphysis, as well as distal femur and proximal tibia, for both cortical and trabecular bone, are described, with important implications for disease models.

This baseline of physiological bone (re)modeling using our advanced microCT-based time-lapse morphometry method is then used to study changes in the bone dynamics caused by breast cancer cell bone metastasis. For this we inject mice with breast cancer cells and monitor the bone (re)modeling to detect pathological changes.

We show that tumor-injected animals without osteolytic lesions have significantly higher parameters for newly mineralized bone in the trabecular region, compared to healthy control mice and with similar

trends for cortical bone. This indicates an influence of cancer cells on the bone (re)modeling even in the absence of detectable lesions and a possible establishment of a pre- or antimetastatic niche.

In order to study early osteolytic lesions caused by breast cancer cells in the bone, we develop an eroded bone patch analysis tool. This new mathematical tool allows us to detect and quantify cortical osteolytic lesions already two weeks after cancer cell injection, clearly distinguishing the pathological and physiological eroded bone patches. In addition, we visually identify lesions in the primary spongiosa of trabecular bone, sitting directly under the mineralized growth plate, already two weeks after cancer cell injection. MicroCT-based time-lapse morphometry allows us to describe for the first time three different types of early osteolytic lesions in the bone: 1) cortical lesions initiating at the periosteum, 2) cortical lesions at the endocortial site with additional trabecular erosion and 3) trabecular lesions in the primary spongiosa at the growth plate.

We then use our *in vivo* results to study the homing of cancer cells in the bone using light-sheet fluorescence microscopy and confocal laser scanning microscopy, as well as the tissue changes caused by early osteolytic lesions with the help of backscattered electron microscopy and advanced confocal laser scanning microscopy.

We study the size and location of cancer cells in 3D (intact) bones after optical clearing with the help of light-sheet fluorescence microscopy, providing 3D quantification of the homing of cancer cells in the bone marrow and bone surrounding tissue. Within the bone marrow, cancer cells home as small cell clusters close to the endocortical bone, but with no apparent preference for different bone compartments.

Further analysis of cancer cell clusters in the marrow revealed that a significant fraction is not proliferating. Additionally, cancer cell clusters have a strong tendency to home in fibronectin-rich areas, providing new implications for the structural features of the cancer cell niche.

We last perform a multiscale analysis of the early metastatic lesions with various imaging techniques and are able to show the changes in the mineralized tissue, as well as the organic collagen matrix.

To sum up, we use microCT-based time-lapse morphometry to study the dynamics and onset of bone metastasis, including a baseline to differentiate from physiological bone (re)modeling. We quantify changes in pathological bone (re)modeling in the absence of detectable osteolytic lesions. Further, we introduce a new tool to detect and quantify early osteolytic lesions in cortical bone. In addition, we visually detect trabecular lesions and are able to classify three different types of lesions in cortical and trabecular bone. Using advanced *ex vivo* multimodal tissue analyses, we describe the homing of cancer

cells to the bone marrow in 3D and characterize the bone microenvironment in early osteolytic lesion. Our work gives important 3D information and new perspectives on various states of cancer research including the debate on pre- or antimetastatic niches, homing and the onset of metastasis in the long bones.

Zusammenfassung

Brustkrebs ist eine der häufigsten krebsbedingten Todesursachen bei Frauen. Während ein Primärtumor oft gut behandelt werden kann, ergibt sich durch Metastasen eine sehr schlechte Prognose, und die Ausbreitung in die Knochen ist eine der häufigsten Form der Metastasierung mit meist tödlichem Ausgang. Während die zelluläre Beteiligung von Knochenmetastasen im Spätstadium der Metastasierung in den Knochen häufig untersucht wurde, sind frühe metastatische Läsionen und die damit verbundenen strukturellen und biophysikalischen Parameter sowie das dynamische (Re-)Modellierungsverhalten des Knochens nicht gut verstanden. Wir stellen die Hypothese auf, dass solche strukturellen und biophysikalischen Veränderungen in der Knochenmikroumgebung, die Entstehung und das Fortschreiten von brustkrebsinduzierten osteolytischen Läsionen beeinflussen.

Um diese Hypothese zu überprüfen, wollen wir ein experimentelles Mausmodell für die Knochenmetastasierung bei Brustkrebs entwickeln, bei dem wir frühe osteolytische Läsionen in 3D erkennen und charakterisieren können.
Um das dynamische Knochen(re)modellierungsverhalten in einem pathologischen Modell untersuchen zu können, muss zunächst eine physiologische Basislinie geschaffen werden. Die *in-vivo* MicroCT-basierte Zeitraffermorphometrie ist ein leistungsfähiges Instrument um zeitliche und räumliche Veränderungen in der Knochen(re)modellierung zu untersuchen. Hierfür stellen wir eine Weiterentwicklung der Methode zur Erkennung und Quantifizierung ortsspezifischer Unterschiede in der Knochen(re)modellierung bei 12 Wochen alten weiblichen BALB/c-Nacktmäusen vor. In dieser Arbeit bestimmen wir neue Parameter für die Knochenoberfläche und zeigen, wie diese von der Knochenkrümmung beeinflusst werden. Wir beschreiben signifikante Unterschiede bei den Basisparametern der Knochen(re)modellierung zwischen Metaphyse und Epiphyse, sowie zwischen distalem Femur und proximaler Tibia, sowohl für kortikalen als auch für trabekulären Knochen, was wichtige Auswirkungen auf Krankheitsmodelle hat. Diese Basislinie der physiologischen Knochen(re)modellierung, gemessen mit unserer fortschrittlichen

MicroCT-basierten Zeitraffermorphometrie, wird verwendet, um die Veränderungen der Knochendynamik durch Knochenmetastasierung zu untersuchen. Zu diesem Zweck injizieren wir Mäusen Brustkrebszellen und beobachten die Knochen(re)modellierung um pathologische Veränderungen zu erkennen. Wir zeigen in dieser Arbeit, dass tumorinjizierte Tiere ohne nachweisbare osteolytische Läsionen deutlich höhere Parameter für neu mineralisierten Knochen im trabekulären Bereich aufweisen, verglichen mit gesunden Kontrollmäusen und mit ähnlichen Verläufen für kortikalen Knochen. Dies deutet, selbst ohne nachweisbare Läsionen, auf einen Einfluss der Krebszellen auf die Knochen(re)modellierung hin und könnte eine mögliche Etablierung einer prä- oder antimetastatischen Nische bedeuten.

Um frühe osteolytische Läsionen zu untersuchen, die durch Brustkrebszellen im Knochen verursacht werden, entwickeln wir in dieser Arbeit ein Werkzeug zur Analyse erodierter Knochenregionen. Mit diesem neuen mathematischen Werkzeug können wir kortikale osteolytische Läsionen bereits zwei Wochen nach der Injektion von Krebszellen erkennen und quantifizieren, wobei zwischen pathologischen und physiologischen erodierten Knochenregionen unterschieden werden kann. Darüber hinaus identifizieren wir bereits zwei Wochen nach der Injektion von Krebszellen visuell Läsionen in der primären Spongiosa des trabekulären Knochens, die direkt unter der mineralisierten Wachstumsfuge liegt. Mit Hilfe der MicroCT-basierten Zeitraffermorphometrie können wir erstmals drei verschiedene Arten von frühen osteolytischen Läsionen im Knochen beschreiben: 1) kortikale Läsionen, die am Periost beginnen, 2) kortikale Läsionen in der endokortikalen Region mit zusätzlicher trabekulärer Erosion und 3) trabekuläre Läsionen in der primären Spongiosa an der Wachstumsfuge.

Anschließend nutzen wir unsere *in-vivo* Ergebnisse, um die Ansiedlung von Krebszellen im Knochen mit Hilfe der Lichtscheibenfluoreszenzmikroskopie und konfokaler Laser-Scanning-Mikroskopie zu untersuchen, sowie die Gewebeveränderungen, die durch frühe osteolytischen Läsionen entstehen mit Hilfe der Rückstreuelektronenmikroskopie und moderner konfokalen Laser-Scanning-Mikroskopie zu beleuchten.

Wir untersuchen die Größe und Lage von Krebszellen im 3D (intakten) Knochen nach optischer Klärung mit Hilfe von Lichtscheibenfluoreszenzmikroskopie, die eine 3D-Quantifizierung der Ansiedlung von Krebszellen im Knochenmark und dem umgebenden Knochengewebe erlaubt. Im Knochenmark siedeln sich die Krebszellen als kleine Zellhaufen in der Nähe des endokortikalen Knochens an, jedoch ohne erkennbare Präferenz für verschiedene Knochenkompartimente.

Eine weitere Analyse der Krebszellhaufen im Knochenmark ergab, dass ein erheblicher Anteil nicht

proliferiert. Darüber hinaus haben Krebszellhaufen eine starke Tendenz, sich in Fibronektin-reichen Bereichen anzusiedeln. Dies liefert neue Erkenntnisse über die strukturellen Merkmale der Krebszellnische.

Zuletzt führen wir eine multiskalige Analyse der frühen metastatischen Läsionen mit verschiedenen bildgebenden Verfahren durch und sind in der Lage, die Veränderungen im mineralisierten Gewebe sowie in der organischen Kollagenmatrix aufzuzeigen.

Zusammenfassend lässt sich sagen, dass wir die MicroCT-basierte Zeitraffermorphometrie nutzen, um die Dynamik und das Auftreten von Knochenmetastasen zu untersuchen, einschließlich einer Basislinie zur Unterscheidung von der physiologischen Knochen(re)modellierung. Wir quantifizieren Veränderungen bei der pathologischen Knochen(re)modellierung in Abwesenheit von nachweisbaren osteolytischen Läsionen. Außerdem stellen wir ein neues Werkzeug zur Erkennung und Quantifizierung früher osteolytischer Läsionen im kortikalen Knochen vor. Darüber hinaus können wir visuell trabekuläre Läsionen erkennen und sind in der Lage, drei verschiedene Arten von Läsionen in kortikalem und trabekulärem Knochen zu klassifizieren. Mithilfe fortschrittlicher multimodaler *ex-vivo* Gewebeanalysen beschreiben wir die Ansiedlung von Krebszellen im Knochenmark in 3D und charakterisieren die Knochenmikroumgebung bei frühen osteolytischen Läsionen. Unsere Arbeit liefert wichtige 3D-Informationen und neue Perspektiven zu verschiedenen Stadien der Krebsforschung, einschließlich der Debatte über prä- oder antimetastatische Nischen, Ansiedlung und die Entstehung von Metastasen in den Röhrenknochen.

CHAPTER 1

Introduction

1.1 Bone microenvironment

The bone is a highly complex organ with many different essential functions, such as providing mechanical stability and protection, being an important calcium storage and providing a niche for stem cells. In order to fulfill all of these different functions, the bone is build in a diverse cellular and structural composition, giving rise to many different physical and biochemical properties. An overview of these cellular, structural and biophysical microenvironments is provided in the following.

1.1.1 Cellular microenvironment

The bone is comprised of a large number of different cell types, most of them present in the bone marrow (Fig. 1.1A). They interact on different levels and influence their activity and maturation. A broad overview of the different cell types and their roles in the bone is given here.

Three types of cells are mainly involved in building and maintaining the mineralized bone tissue. Osteoblasts are the bone-forming cells that produce the organic bone matrix and are responsible for the mineralization process[1]. If osteoblasts are spared from undergoing apoptosis at the end of a bone formation cycle, they can get incorporated into the mineralized tissue, where they are turned into osteocytes and can have a lifespan of decades. Osteocytes are the most abundant cells in the mineralized bone tissue and account for 95% of all bone cells. During the embedding in the bone, osteocytes change their morphology drastically, lose many cell organelles, as well as cytoplasm and acquire a stellar shape with many thin extension. They remain connected with each other and osteoblasts on the bone surface through these connections[2].

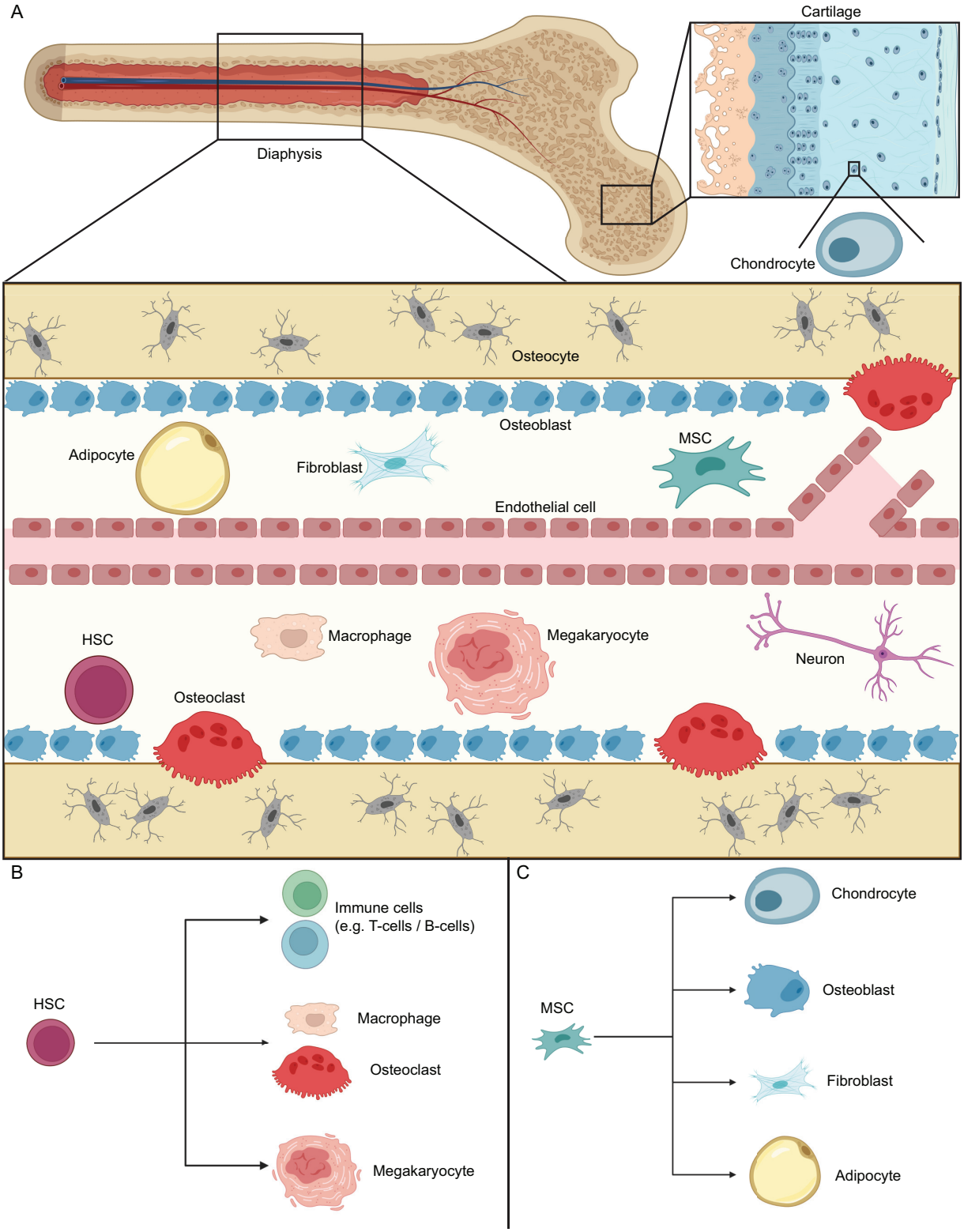

Fig. 1.1: **Schematic of the cellular microenvironment in the bone and simplified depiction of the HSC and MSC lineage.** (A) Schematic of cells in the cartilage (chondrocytes) and diaphysis of the bone including the bone cells (osteocytes, osteoblasts and osteoclasts), endothelial cells and neurons, adipocytes, fibroblasts, macrophages and megakaryocytes as well as HSCs and MSCs. (B) Simplyfied depiction of the general HSC lineage to immune cells, macrophages and osteoclasts, as well as megakaryocytes. (C) Simplified depiction of the MSC lineage to chondrocytes, osteoblasts, fibroblasts and adipocytes. [3] [4] (created with BioRender.com)

The last cell type involved in maintaining the mineralized bone is the bone-eroding osteoclast, a unique type of exocrine cell, that has the ability to dissolve bone mineral and degrade the extracellular matrix (ECM) proteins[5]. Osteoclasts are large cells with multiple nuclei that form by fusion of precursor mononuclear cells[2].

The cortical bone has an outer periosteal and an inner endosteal surface. The periosteum has two layers, an outer fibrous connective tissue layer and an inner cellular layer mostly containing osteoprogenitor (fibroblast-like) cells. The endosteum on the other hand, is a membranous quiescent monolayer mostly covered with flattened osteoprogenitor cells, referred to as bone lining cells[6] [7].

Next to the mineralized tissue, the cartilage is one of the tissues specific to bone, as it can also mineralize, a process known as endochondral ossification. Chondrocytes are the cell type found in cartilage and responsible for providing a template for later ossification. They are also the first skeleton-specific cell type to appear during development and provide several functions such as longitudinal growth or mobility in the joints[1].

Aside from the mineralized tissue and cartilage, the bone marrow homes a large number of different cells with essential functions for the entire body.

The bone is filled with blood vessels that form complex structures and different zones. These blood vessels are lined with endothelial cells that can be sorted into three different categories: arteriolar, sinusoidal and capillary endothelial cells[8]. The perivascular niche is known to be one of the main stem cell niches, but also expected to home different cancer cells.

Next to the highly complex vascularization network, a neural system is spanning the bone with neurons enabling the sensation of pain or pressure[9].

The bone marrow itself is home to additional cells with diverse functions such as adipocytes, known also as fat cells and specialized in storing energy, or megakaryocytes - responsible for the production of thrombocytes - as well as fibroblasts and macrophages[3] [4].

Aside from this complex cellular composition, the bone marrow also provides an important niche for both haematopoetic stem cells (HSCs) and mesenchymal stem cells (MSCs). Both cell types reside in the bone marrow and give rise to a large number of cells, with complex lineage trees that are presented in a simplified version in the following. HSCs can differentiate into immune cells such as T-cells and B-cells, and also give rise to macrophages and osteoclasts, as well as megakaryocytes (Fig. 1.1B). MSCs can differentiate into chondrocytes, osteoblasts, fibroblasts and adipocytes (Fig. 1.1C)[3].

The cellular composition of the bone is highly complex and the types, interactions and control mech-

anisms are still a subject of intense research today.

1.1.2 Structural microenvironment

Next to the cellular components, the bone is build of a complex structural microenvironment. This includes the ECM many different proteins and proteoglycans building both soft and mineralized tissue, as well as a rich vascular and neural network.

Extracellular matrix network

The ECM is a non-cellular, highly dynamic and complex 3D-network, that is composed 1) proteoglycans, 2) fibrous proteins such a collagen and fibronectin (FN) 3) glycosaminoglycans and 4) matricellular proteins like osteocalcin that provide a linkage between ECM proteins and cellular receptors [4] [10] [11]. The most abundant proteins in the ECM of the mineralized bone tissue and bone marrow are FN, collagen type I-X, laminin, tenascin, thrombospondin and elastin [4].

The distribution of ECM components in both the mineralized bone tissue and bone marrow is highly spatially organized [10] [12]. The mineralized bone tissue is mainly built of collagens type I and III, osteocalcin, vitronectin, osteopontin and periostin [4]. The periosteum contains thick collagen type I fibers, called Sherpey's fibers, which extend into underlying bone tissue. The endosteum on the other hand, is a membranous structure mainly containing collagen type III [6]. Cartilage is mainly composed of a network of collagen type II, interlocking with a mesh of other fibrous proteins, proteoglycans and the glycosaminoglycans hyaluronic acid and chondroitin sulfate [13]. Lastly, the bone marrow contains collagen IV, laminin and fibronectin [4].

While the ECM regulates structural scaffolding, stiffness and deformability of tissues, it also serves as a major source of proteases and growth factors [14], linking the biophysical and biochemical cues. Some ECM components also contain direct binding units for cell interactions and mechanotransduction processes. The triple-helical motif of collagen for example, can be bound by cell receptors directly and FN contains an arginine-glycine-aspartic acid (RGD) motif that provides attachment for cells via integrins [4].

The ECM composition, architecture and spatial distribution has mainly been studied with histological and immunostaining of thin and thick tissue sections, combined with (polarized) light microscopy [6] [10] [15]. Although these technique have given many important insights, they rely on the quality of antibodies and limit the 3D information to a few micrometers in depth. The collagen fib-

rils on the other hand, possess a high nonlinear susceptibility and can therefore be studied with the help of second harmonic generation (SHG) microscopy [16]. No additional staining is required with this technique and fibrillar collagen can be studied in a depth of 10 – 100 µm, even in fully mineralized tissue [17]. New imaging tools like light-sheet fluorescence microscopy (LSFM) might be powerful tools to gain further information on the distribution of ECM proteins and components in 3D [18] [19].

Mineralized tissue

The mineralized tissue of the bone is an organic-inorganic composite material. The main building blocks are protein fibrils - predominately collagen type I -, mineral crystals composed of hydroxyapatite and water [20]. The collagen fibrils have a length of around 300 nm, with 1.5 – 4 nm thick hydroxyapatite nanocrystals deposited along them [21] [22]. These fibrils then assemble larger fibers that build the compact bone, embedding osteocytes into their structure. These osteocytes sit in lanunae, with a network of channels referred to as canaliculi, both building the lacunar canaliculi network. This network is known to fulfill several different functions, including intercellular transport and communication, mechanosensation connected to the regulation of bone (re)modeling, as well as endocrine functions and communication with a number of other organs [23]. The mineralized tissue can be studied with various techniques from macro- to nanometer scale. While backscattered electron (BSE) microscopy can be used to study the differences in mineral content at a high resolution [24], microcomputed tomography (microCT) allows a 3D view of the mineralized tissue [25]. In addition, the lacunae canaliculi network can be studied with the help of (advanced) microCT [26], stainings like rhodamine combined with confocal laser scanning microscopy (CLSM) [27] [28] and more advanced electron microscopy methods that allow high resolution imaging [29].

Bone vasculature

Both the periosteum and the bone marrow are highly vascularized tissues (Fig. 1.2). The inflow into the bone marrow is considered to emerge from one or several arteries entering the bone either midway along the shaft or at the epiphysis and link to the dense network of capillaries in the bone marrow [30] [31]. Arterial capillaries are connected to the venous tree by transition zone vessels [32] [33] and connect through sinusoids into a large central sinus [34]. In addition, Grüneboom et al. recently discovered an additional network of trans-cortical vessels, expressing both arterial and venous markers. They showed to carry 80% of arterial and 59% of venous blood and traverse the cortical bone perpendicularly along

the shaft, connecting the bone marrow capillaries to the periosteal circulation [18].

One important technique that was used in this discovery was LSFM of optically cleared bones. In the clearing process, water in the bone tissue is first replace with ethanol and then substituted with the organic solvent ethyl cinnamate without dissolving the mineral, leading to the mineralized tissue becoming transparent as the solvent matches the refractive index of the bone [18] [35] (Refractive indices: water 1.33, ethyl cinnamate 1.56, mineralized bone 1.56 [36]). LSFM, illuminating only a (virtual) thin slice of the fluorescent sample [37], can then be used to study structural and cellular elements of the bone microenvironment in 3D without sectioning.

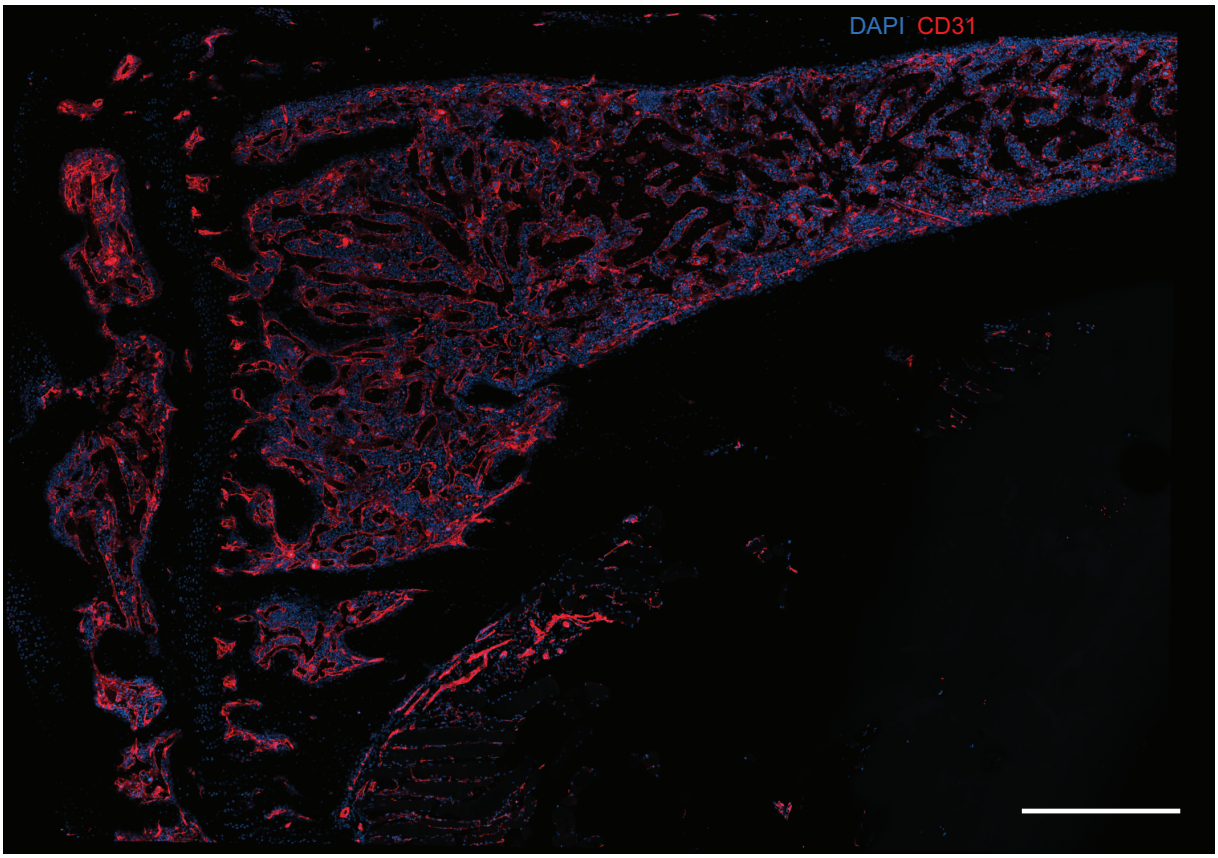

Fig. 1.2: **Highly vascularized bone marrow of the tibia**, stained with DAPI (nucleus) in blue and CD31 (endothelial cells, hence blood vessels) in red. (Scale bar corresponds to 500 µm.)

1.1.3 Biophysical microenvironment

Both cellular and structural components of the bone microenvironment are highly connected to the biophysical properties of the bone. Some parameters like stiffness and tension have been in the focus, as they change dramatically in different compartments of the bone, for example between the mineralized tissue and the bone marrow. Next to mechanical parameters like rigidity, stiffness and

tension[38] [39], people have studied the influence of curvature on tissue growth in the bone[17] or the osmotic pressure induced forces in tendon[40]. Other interesting parameters that connect both the chemical and physical disciplines, are the changes in pH and oxygen levels. All these parameters are often very difficult to study or measure especially in fully or partly intact bones and appropriate tools still need to be developed. More accessible *in vitro* systems have shown though, that the biophysical parameters have an essential influence on both cellular and structural properties, leading to stem cell fate changes[41] [42] [43], cell life and death control via geometrical control[44] and in a more previous *ex vivo* study the loss of tension in cancer infiltrated tissues[45].

1.2 Mineralized bone (re)modeling

In its role as mechanical support system to our body, the bone has to continuously adapt to external stimuli and changes with bone damage repair mechanisms. On the tissue level, two different processes can be described, that are involved in the formation of bone and the adaptation process, describing the dynamic changes in bone structure, referred to as bone modeling and bone remodeling, or in short bone (re)modeling[46] [47] [48]. Bone modeling refers to the process to remove or add bone material with the aim of structural adaptation, without a spatio-temporal connection between new mineralization and erosion[49] (Fig. 1.3A). In bone remodeling (Fig. 1.3B) on the other hand, the purpose is bone maintenance or damage repair and for this osteoclasts are recruited to a specific area for bone erosion, followed by a recruitment of osteoblasts that lead to new mineralization[46].

Two important factors responsible for local osteoblast differentiation and hence new mineralization are bone morphogenetic protein (BMP)[50] and wingless (Wnt)[51]. BMP regulates the expression of runt-related transcription factor 2 (RUNX2), while Wnt signaling is a key pathway in bone formation. In the canonical Wnt pathway, several factors are activated that are crucial for osteoblast differentiation[2], while there is also evidence towards an inhibition of receptor activator of nuclear factor-κB ligand (RANKL), negatively regulating osteoclasts[52]. Osteoclast differentiation on the other hand, is initiated through c-fms, which is a receptor for macrophage colony stimulating factor (MCSF) and upregulates expression of receptor activator of nuclear factor-κB (RANK)[53]. The corresponding ligand RANKL is expressed by osteoblasts and stromal cells. Signaling through c-fms and RANK is the key driver for osteoclast formation and continued signaling is necessary for osteoclast survival. RANK signaling is activated through RANKL, which can on the other hand be blocked by osteoprotegerin

(OPG), inhibiting RANK signaling and hence bone erosion [2] (Fig. 1.3C).

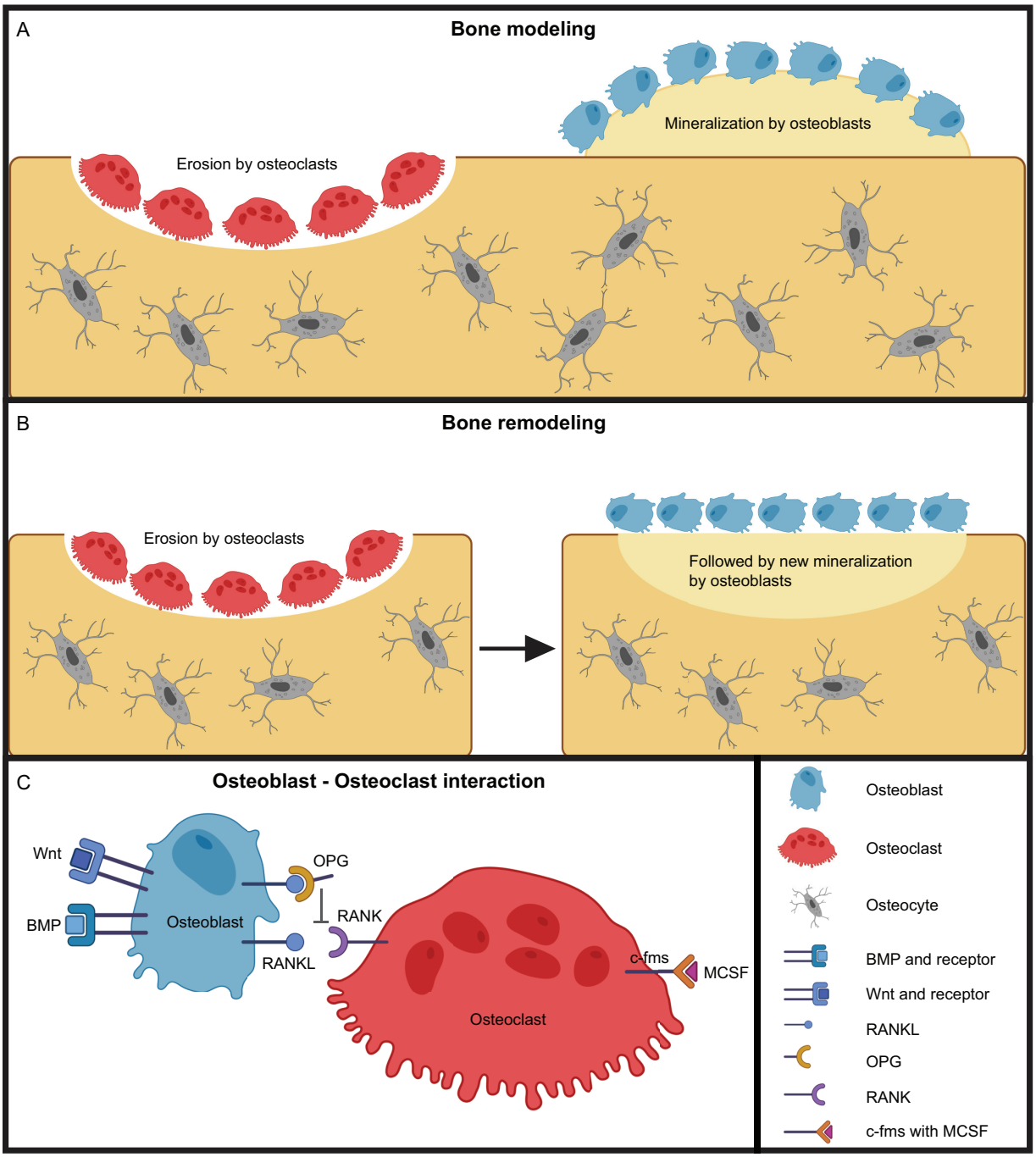

Fig. 1.3: **Schematic of bone modeling and remodeling, as well as the interaction between osteoblasts and osteoclasts.** (A) Depiction of bone modeling with erosion and mineralization spatially and temporally independent, (B) remodeling of bone with erosion followed by mineralization and (C) interaction between osteoblast and osteoclast, as well as differentiation factors (including a legend). (created with BioRender.com)

1.2.1 Methods to study bone (re)modeling

The changes of the mineralized tissue during bone (re)modeling have been studied with several different methods, including advanced *ex vivo* or *in vivo* imaging or a combinations of different techniques.

2D dynamic histomorphometry

The classic method to study bone (re)modeling in mice is 2D dynamic histomorphometry, making use of fluorochrome labeling[47] [48] [54] [55] [56] [57]. For this method, fluorescent dyes like calcein are injected into the living animal and integrate into the bone during new mineralized bone formation. When different or the same dye are injected at different time points, the evolution of new mineralization in between those time points, as well as the bone turnover can be studied (Fig. 1.4A). The animal has to be sacrificed to obtain the information using CLSM, leaving no room for *in vivo* monitoring. The method has been used in many different studies and different models. However, the technical difficulties and errors occurring from complex imaging and frequent injections of the animals make it a very time-consuming method, limited to mainly 2D information obtained *ex vivo*.

Static *in vivo* microcomputed tomography

A different method that gives more flexibility with *in vivo* monitoring and allows the quantification of bulk changes in bone in 3D is static microCT with an exemplary image of one section shown in Fig. 1.4B.

For microCT imaging, an X-ray beam is traversing an object leading to a change in attenuation depending on the nature of the material. Bone can be studied very well with microCT, as the calcium in the mineralized tissue is a higher atomic number structure, absorbing more X-ray photons than the surrounding soft tissue with lower atomic number structures. Within the microCT, the X-ray source and 2D detector are oriented towards each other. Two different instrument configurations have been implemented for *in vivo* microCT imaging vs. *in vitro*/*ex vivo* imaging of samples. The specimen rotates in the *in vitro* systems, whereas the X-ray source and the detector are rotating around the animal in *in vivo* systems. At several positions, a 2D projection image is acquired and the final 3D image is obtained by a full set of 2D angular radiographs recorded usually over 180° or 360°. For the conversion to the 3D image, different reconstruction methods exist, however the most common method is the filtered backprojection[58].

Static microCT has significantly advanced the possibilities to study bone (re)modeling as it allows several *in vivo* measurements at µm resolution. The microstructure and density of the bone at a given time point can be quantified [25] [59] [60] [61] [62] [63]. By comparing different time points, a longitudinal assessment of changes in the bone structure and density is possible [64]. Parameters frequently obtained for cortical bone are: total volume (TV) (describing the total volume of both soft and mineralized tissue), bone volume (BV) (describing the mineralized tissue volume), bone volume fraction (BV/TV) and bone surface over bone volume (BS/BV). For trabecular bone standard parameters are TV, describes the marrow volume containing the trabeculae, BV and BV/TV, as well as the more specific parameters of trabecular number (Tb.N), thickness (Tb.Th) and separation (Tb.Sp) [25]. As limitation, the animals get exposed to high levels of radiation, which can influence the bone (re)modeling and cellular composition of the marrow. Further, the dynamic evolution of the (re)modeled bone over time and the spatial information of specific formation and resorption events, cannot be obtained with static microCT.

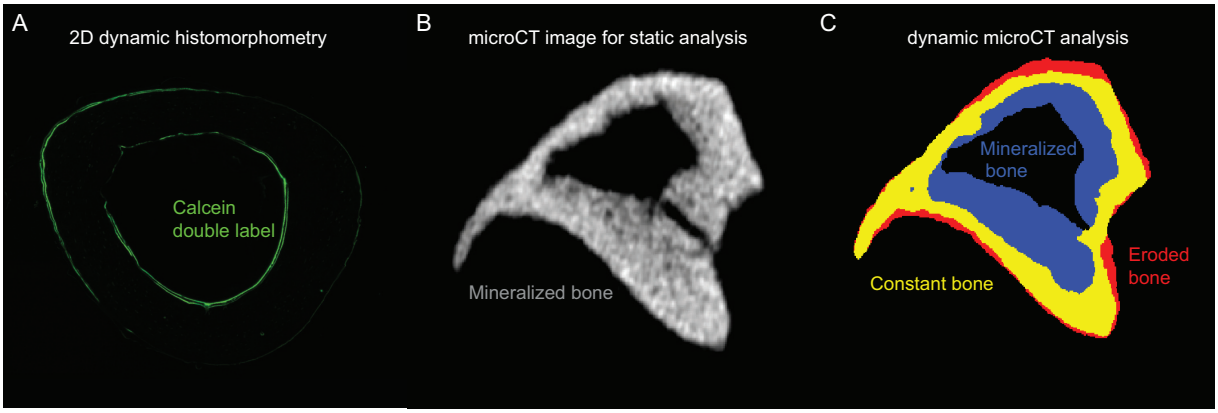

Fig. 1.4: **Different methods to study bone (re)modeling.** (A) Calcein label (we thank Dr. Victoria Schemenz for providing the image), (B) in vivo CT, single time point (C) microCT-based time-lapse morphometry.

Dynamic *in vivo* microcomputed tomography-based time-lapse morphometry

In the past years, several groups have further developed microCT-based bone analysis to acquire more detailed spatio-temporal information. With the help of dynamic *in vivo* microCT-based time-lapse morphometry, temporal and spatial monitoring of both bone mineralization and erosion events becomes possible [65] [66] [67] [68] [69]. MicroCT scans of the same animal are acquired at different time points, repositioning the animal in the same location as well as possible in each scan. The datasets of later time points are then geometrically aligned (registered) to compensate for changes during repositioning. By comparing the well aligned datasets from two different time points, newly mineralized and

eroded bone voxels can be evaluated. The method allows for the quantification of volumes, surfaces, thickness/depth and rates of bone mineralization and erosion, all with respect to the initial bone structure.

Parameters that are frequently acquired with this method are normalized newly mineralized bone volume (MV/BV) and normalized eroded bone volume (EV/BV) (volume parameters), normalized mineralized bone surface (MS/BS) and normalized eroded bone surface (ES/BS) as surface parameters and 3D mineral apposition rate (MAR) as well as 3D mineral resorption rate (MRR) for dynamic analysis. The evaluation of the mineralized and eroded bone surface was based on 2D histomorphometry. The surface of newly mineralized bone was described by looking at the interface between constant and newly mineralized bone - being the original bone surface at the reference day, now covered by newly mineralized bone. The eroded surface was defined as the interface between eroded bone and soft tissue - which also describes the original bone surface at the reference day, now eroded [66] [67]. This analysis leaves room to study two additional interfaces, being the newly mineralized - soft tissue interface and the eroded bone - constant bone interface.

The accuracy of the method was studied and confirmed by comparison with 2D dynamic histomorphometry using fluorochrome labeling for cortical [66] and trabecular [70] bone. Also the precision of the method, depending on the respective instrument used, has been reported in the past [66] [71]. In addition, the method has been used to show differences between (re)modeling at the endosteal and periosteal surface [72], or between different cortical regions (proximal metaphysis and mid-diaphysis) of the same limb [73]. The method can be used to study physiological (re)modeling or (re)modeling in various disease models [74] [75]. One of the main limitations is the exposure of the animals to radiation.

1.3 Breast cancer bone metastasis

Breast cancer is one of the leading causes for cancer-associated deaths among woman worldwide [76]. Often breast cancer metastasizes to bone, where it leads to osteolytic lesions [77] and drastically lowers the prognosis by being considered incurable using currently available therapies [78]. In general, breast cancer is classified into four subtypes: 1) luminal A, 2) luminal B, 3) basal-like and 4) human epidermal growth factor receptor 2 (HER2)-enriched [79]. Some additional histological and molecular characteristics are currently taken into account leading to a distinction between 1) hormone receptor-positive

(tumors expressing oestrogen receptor (ER) and/or progesterone receptor (PR)) and 2) triple-negative (tumors expressing neither ER, PR nor HER2) breast cancer [78].

Human breast cancer cell lines are frequently used in immunodeficient mouse models (xenograft models). ER positive luminal A cell lines like MCF-7 or T47D, only form tumors in the presence of oestrogen, while cell lines from other subtypes for example BT474, MDA-MB-468 or MDA-MB-231 have been shown to be highly tumorigenic. Cell lines from the HER2-enriched subtype like SKBR3 and MDA-MB-453 on the other hand, have only weaker tumorigenic potential [80]. The MDA-MB-231 cell line has proven useful in models of experimental metastasis, where the cells are directly introduced into the blood circulation. Massague's group has performed several rows of selection to develop highly metastatic derivatives for specific organ tropism such as bone and lung [81].

The MDA-MB-231 cell line was established from the adenocarcinoma of a 51-year-old caucasian female and is known to be highly aggressive and invasive in *in vitro* studies. To study bone metastasis via an experimental model with intracardiac injection, a sub-line of the original MDA-MB-231 cell line was used in this study. The sub-line 1833 was derived by intracardiac injection of mice with the parental cell line, followed by harvesting of the metastasized cells from the bone. In comparison to other sub-lines, the 1833-line is still considered parental like in a gene expression experiment, although clear differences can be observed [81].

1.3.1 Mouse models of bone metastasis

As bone metastases are among the most frequent sites of metastasis from breast cancer, animal models are an important tool to investigate the progression of the disease and develop treatment strategies. An ideal model of metastasis should reproduce the genetic and phenotypic changes that occur with human cancers, permitting tissue invasion at the primary site, intravasation as well as extravasation to the secondary site, survival and proliferation in the bone marrow and modification of bone structure and function. As spontaneous bone metastasis in animals is uncommon, most animal models must be derived experimentally. In general, animal models of metastasis can be categorized as follows: 1) spontaneous tumors and metastasis, 2) syngeneic transplantation of spontaneously occurring cancers, 3) chemical induction of cancers, 4) transgenic mouse models and 5) xenografts of human tumors or cell lines to immunodeficient rodents (Fig. 1.5) [82].

Within the xenograft models, different methods can be applied to study specific steps of the metastatic process (Fig. 1.5) [82]. Orthotopic models are used if the intravasation or the pre-metastatic niche are

investigated, injecting cancer cells directly into the mammary gland [82] [83]. To study the metastatic phase, the most direct and reliable form is the injection of cancer cells into the long bones. Advanced metastatic disease can be studied with this model, but a main disadvantage is the bone tissue damage through the injection and consequent alteration in bone (re)modeling, which is directly linked with tumor progression. Therefore, a different model of metastasis makes use of injecting cancer cells directly into the blood stream. With the help of these models, extravasation to the secondary site and early as well as advanced bone metastases can be studied. For lung metastases, an intravenous injection is used, while bone metastases can be achieved by intracardiac injection into the left ventricle or intracaudal arterial injection [84].

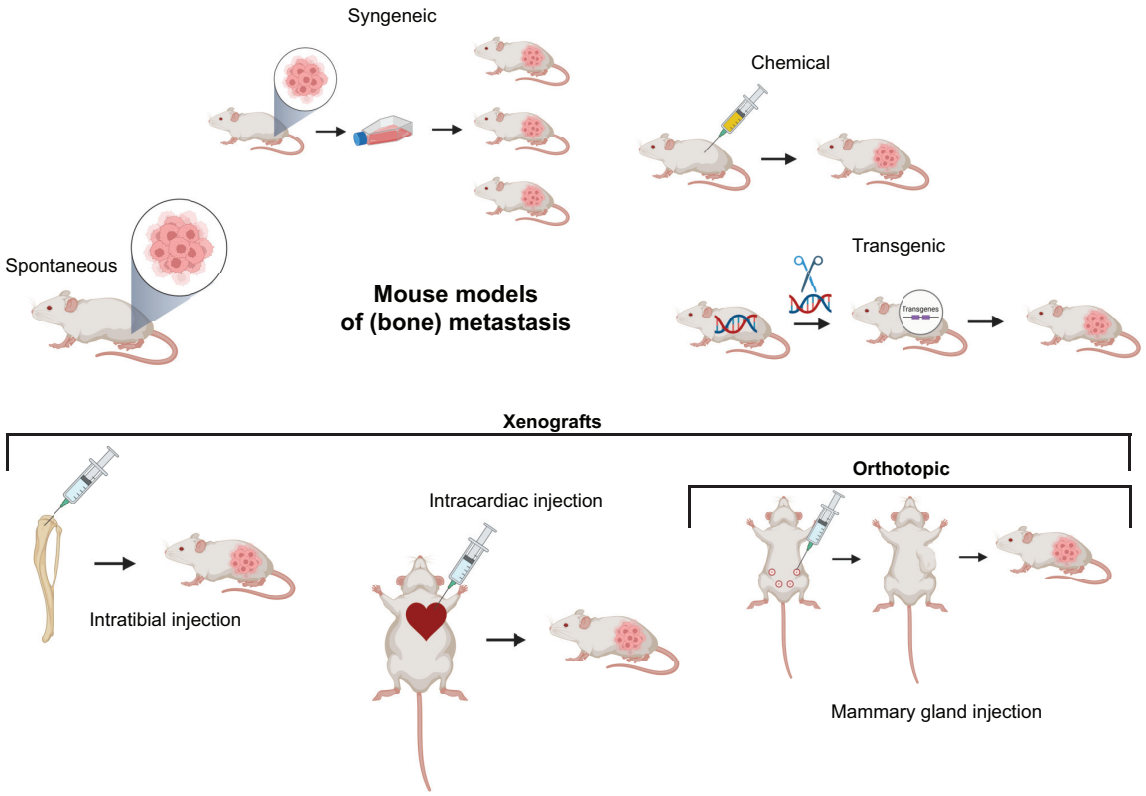

Fig. 1.5: **Mouse models of (bone) metastasis** Depicting spontaneous, syngeneic, chemical and transgenic models as well as the xenograft models using intratibial, intracardiac and mammary gland injections (orthotopic model). [82] (created with BioRender.com)

1.3.2 Bone metastatic niche

Breast cancer frequently metastasizes to the bone, undergoing different stages of activity, from a dormant stage that can last up to decades, to fully active metastases that massively change the bone structure up to skeletal morbidity [85] (Fig. 1.6). Even before the arrival of cancer cells to the

bone, changes in the bone microenvironment have been postulated and described as the premetastatic niche [86].

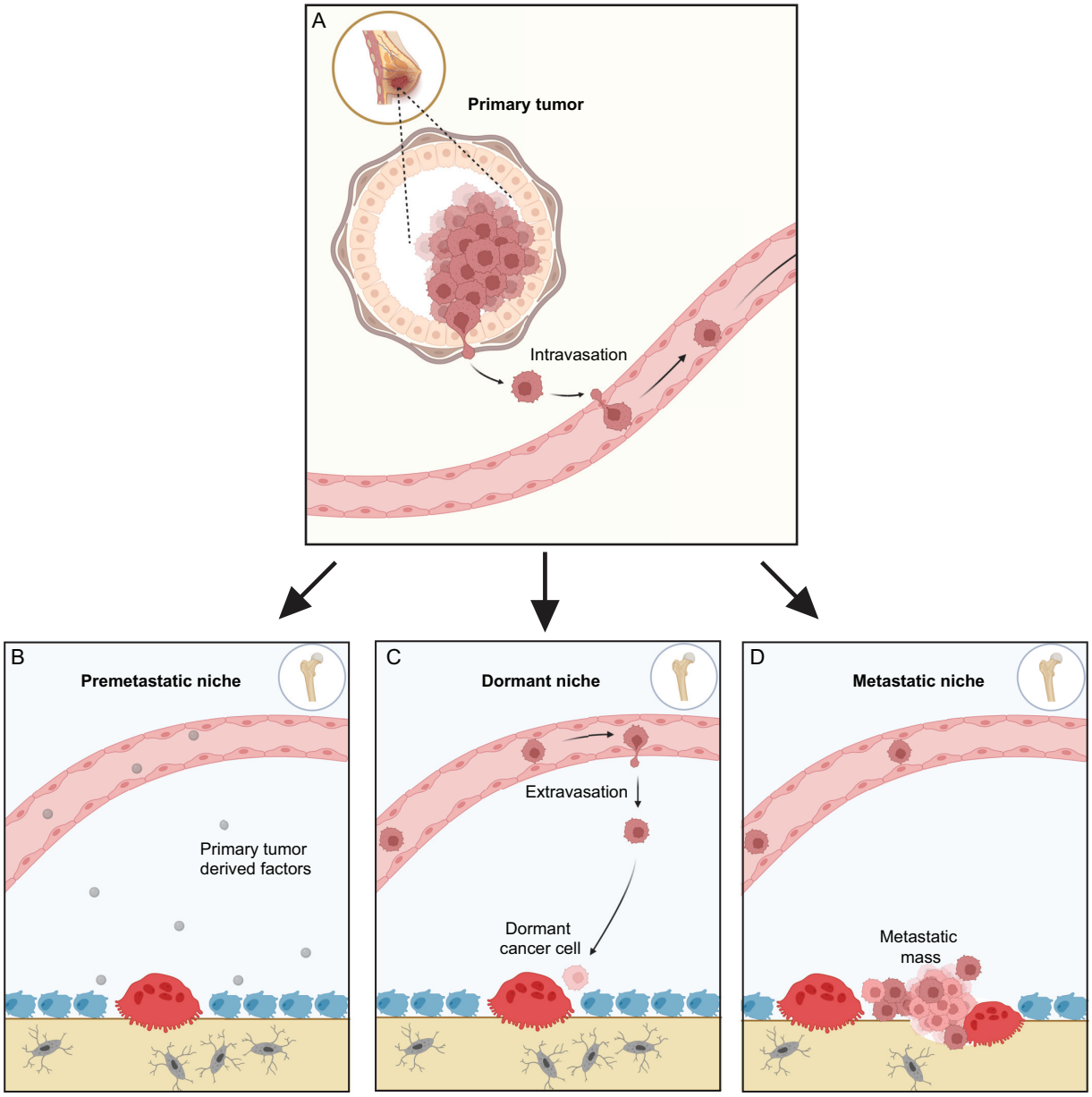

***Fig. 1.6:* Schematic showing the different stages of metastatic outgrowth.** A) The site of the primary tumor in the breast tissue with cells intravasating into the blood stream. B) Premetastatic niche influenced by primary tumor derived factors leading to possible alterations in bone (re)modeling, prior to arrival of cancer cells. C) Dormant breast cancer cell in either the endosteal or perivascular niche. D) Metastatic niche with a growing tumor mass, recruiting cells to form osteolytic lesions. (created with BioRender.com)

Much work has been reported on primary tumor growth, invasion (Fig. 1.6A) and advanced overt metastasis, but less is known about the intermediate stages such as the premetastatic niche (Fig. 1.6B), dormant niche (Fig. 1.6C), early metastasis (Fig. 1.6D) or the antimetastatic niche. Furthermore, in each of these phases, specific changes in the bone cellular, structural or biophysical microenvironment

occur that influence the progression of the disease. Much focus has been put on describing the cellular and molecular environment, while less is known about the structural and biophysical changes occurring.

Premetastatic niche

Fundamental discoveries in the last years have shown, that primary tumors induce changes in the microenvironment of distant organs, making them conducive to the survival and outgrowth of tumor cells, even before they have arrived at these sites (Fig. 1.6B) [87] [86]. Since these first fundamental findings, many studies have explored the complex molecular and cellular changes occurring in the premetastatic niche [88] and it has become clear that remodeling of the ECM is crucial for establishing the premetastatic niche. Important evidence of the premetastatic niches exists for other organs like the lung [86] [89], yet the data for the bone marrow niche is limited to the context of endocrine-like actions [90]. A recent finding by Chiou et al. shows more mineralized bone formation after injection of tumor conditioned media, pointing towards an osteoblastic reaction in the premetastatic niche, preceding late-stage osteolytic disease, although this causality has not been shown for breast cancer bone metastasis [91]. It is clear, that much more research is necessary to understand the dynamic changes occurring in the bone marrow on a cellular, molecular, structural and biophysical level, in response to premetastatic conditioning.

Dormancy inducing niche

The spread of cancer cells to the bone is a multi-step process that begins with the colonization, when circulating tumor cells enter the bone marrow and engage with different bone niches. As a survival mechanism in the new environment, cancer cells might enter a phase of dormancy lasting up to several decades (Fig. 1.6C). Next, cells need to have the ability to escape from dormancy (if they had entered this phase) and start to proliferate to form micrometastasis. In the final step, cancer cells grow uncontrollably and form irreversible macrometastasis modifying the bone microenvironment drastically [7]. The phase of dormancy is especially interesting, because relapse and metastatic outgrowth can occur 20-25 years after tumor resection, implying that the cells are growth arrested and hence dormant in that time [92]. Three different mechanisms of dormancy have been identified: 1) escape from immunosurveillance, 2) angiogenic tumor dormancy in larger tumors with a balanced cell division and apoptosis and 3) dormancy of solitary cells (cellular dormancy) with a growth arrest in the G0-G1

phase of the cell cycle [93]. Dormant single cells have typically low Ki67 expression, high p21 and p27 expression, as well as phosphorylated p38 [94]. Although several markers have been associated with dormancy, there is an ongoing discussion in the field and usually a combination of several markers is used to define dormancy. The absence of Ki67 though, is often used as a first indicator for a growth arrest.

In the bone two main 'niches' have been described to support cellular dormancy: the endosteal and the perivascular niche. The endosteal niche mainly consists of a quiescent layer of bone lining cells that connect to the osteocyte network in the mineralized bone [7]. It has been shown, that tumor cells that metastasize to secondary organs, follow mechanisms from HSCs [95]. As the endosteal bone surface is in the focus as a HSC niche, an open hypothesis of cancer cells hijacking this niche is currently debated. The perivascular niche on the other hand has been associated with dormancy [96], although changes (e.g. sprouting) in the perivascular niche have been shown to increase cancer cell growth [97]. In general the long latency of bone metastasis suggests that the dormancy supportive niche is rather stable and does not undergo short-term change. Overall, the question of the niche is a developing field with controversies that will benefit from better (3D) imaging techniques, *in vivo* and *ex vivo*, that will shed light on this topic. Although the concept of dormancy has become an important focus point in metastasis research, there are many open questions surrounding this topic, especially in the bone microenvironment. It is unclear for now which structural and biophysical parameters can lead to dormancy or relapse, which regions of the bone are providing a dormant or even antimetastatic niche and how dynamic parameters like bone (re)modeling, also due to injury, might influence dormant cancer cells.

(Early) metastatic niche

Metastasis of breast cancer cells to the bone causes osteolytic lesions leading to skeletal morbidity with major complications and reduction of overall survival in patients [85]. The outgrowth of cancer cells in the bones undergoes two stages as described above, with early lesions caused by micrometastasis (Fig. 1.6D) and larger lesions and skeletal morbidity due to macrometastasis. The mechanism leading to macrometastasis with large osteolytic lesions and the effects on the bone microenvironment have been studied and are referred to as the 'vicious cycle'. It has been shown, that cancer cells can directly stimulate osteoclasts through interleukin-11 [98] or indirectly induce osteoclastogenesis by altering the RANKL/OPG production of osteoblasts and osteocytes [99]. During bone resorption, factors are re-

leased that further stimulate tumor growth, completing the 'vicious cycle' [100]. The mechanism and dynamics triggering the onset of early lesions on the other hand, have not been studied in depth and the actual cause of bone resorption is not clear, as in vitro experiments have shown, that direct resorption of bone by human breast cancer cells is also possible [101]. It has been shown though, that younger mice (6-week-old) tend to have more metastasis forming, even if the initial number of cancer cells arriving in the bone marrow is comparable to older mice (16-week-old) [102]. In addition, the influence of the structural and biophysical bone microenvironment on metastasis development and, vise versa, their changes due to tumor outgrowth, are not well understood. On this line, He et al. were able to show, that the outgrowth of tumors influences the hydroxyapatite nanostructure in the mineralized tissue [103].

1.4 Aims of the study

We hypothesize, that the structural and biophysical microenvironment in the bone modulate the establishment and progression of an osteolytic lesion caused by breast cancer metastasis. To address this hypothesis, we aim to develop an experimental mouse model of breast cancer bone metastasis for the 3D visualization and characterization of the early bone metastatic niche. With this model we want to study (i) pathological alterations in bone (re)modeling in the absence of detectable osteolytic lesions, (ii) establish a tool to detect and characterize the small osteolytic bone lesions and (iii) study the cancer cell niche in the bone microenvironment.
This thesis is structured in two different parts, firstly *in vivo* work and secondly *ex vivo* work, both with several specific aims:

1. Aim: To **define** baseline parameters of physiological (re)modeling in specific bone areas, in order to quantify the dynamics of bone (re)modeling in a reliable way, while also being sensitive enough to detect region specific pathological alterations.
2. Aim: : To **quantify** changes in the bone (re)modeling dynamics after cancer cell injection in animals without detectable osteolytic lesions in the long bones.
3. Aim: To **establish** a sensitive and robust tool able to detect the onset and track the growth of small osteolytic lesions in cortical bone, while being able to distinguish them from physiological bone erosion.
4. Aim: To **detect and categorize** all types of osteolytic lesion in both cortical and trabecular bone.
5. Aim: To **visualize and map** in 3D fluorescently labeled cancer cells and small cell clusters in the marrow of 3D (intact) bones using 3D LSFM.
6. Aim: To **characterize** the proliferation activity and the structural microenvironment of cancer cells and small cell clusters in the bone marrow.
7. Aim: To **characterize** the structural and biophysical microenvironment of small osteolytic lesions at early stage bone metastasis using multiscale and multimodal imaging tools.

CHAPTER 2

Materials and Methods

Experiments were carried out in two separate parts starting with the *in vivo* analysis, determining the point of sacrifice for the animals and the later *ex vivo* analysis of the bones (femur and tibia). For the *in vivo* work different groups of animals were used: 1) healthy animals with phosphate buffered saline (PBS) injections that were monitored for up to 45 days (n = 7), 2) healthy animals with PBS injections that were monitored for 17 days (n = 3), 3) cancer cell injected animals that showed osteolytic lesions in tibia and/or femur based on microCT imaging (n = 6) and 4) cancer cell injected animals that did not show osteolytic lesions (n = 5). The main tool of analysis for the *in vivo* work was microCT imaging (Fig. 2.1A and B). Animals were either sacrificed after an osteolytic lesion was detected in one of the four bone regions with the help of microCT imaging, or if the animal fulfilled any of the humane endpoint criteria (for example dramatic loss of weight or limping). Consequently, bones from tumor animals were harvested at time points ranging between 17 and 38 days.

For the *ex vivo* work, both limbs of all animals (2 femora and 2 tibiae each) were harvested. Two different methods of embedding without demineralization were used for analysis with different techniques: resin embedding and cryo-embedding. One tibia and one femur (in preference with osteolytic lesion) from each animal was embedded in resin with additional rhodamine staining, while tibiae were in addition optically cleared and measured with LSFM. After controlled angle cutting to expose the osteolytic lesion, sections were histologically stained and the block was analyzed with CLSM and BSE imaging (Fig. 2.1C). One tibia and one femur from each animal (in preference without osteolytic lesion) were cryo-embedded and sectioned with Kawamoto-films for immunofluorescence (IF) staining against the cell proliferation marker Ki67 and FN (Fig. 2.1C). The methods are explained in detail in the following sections.

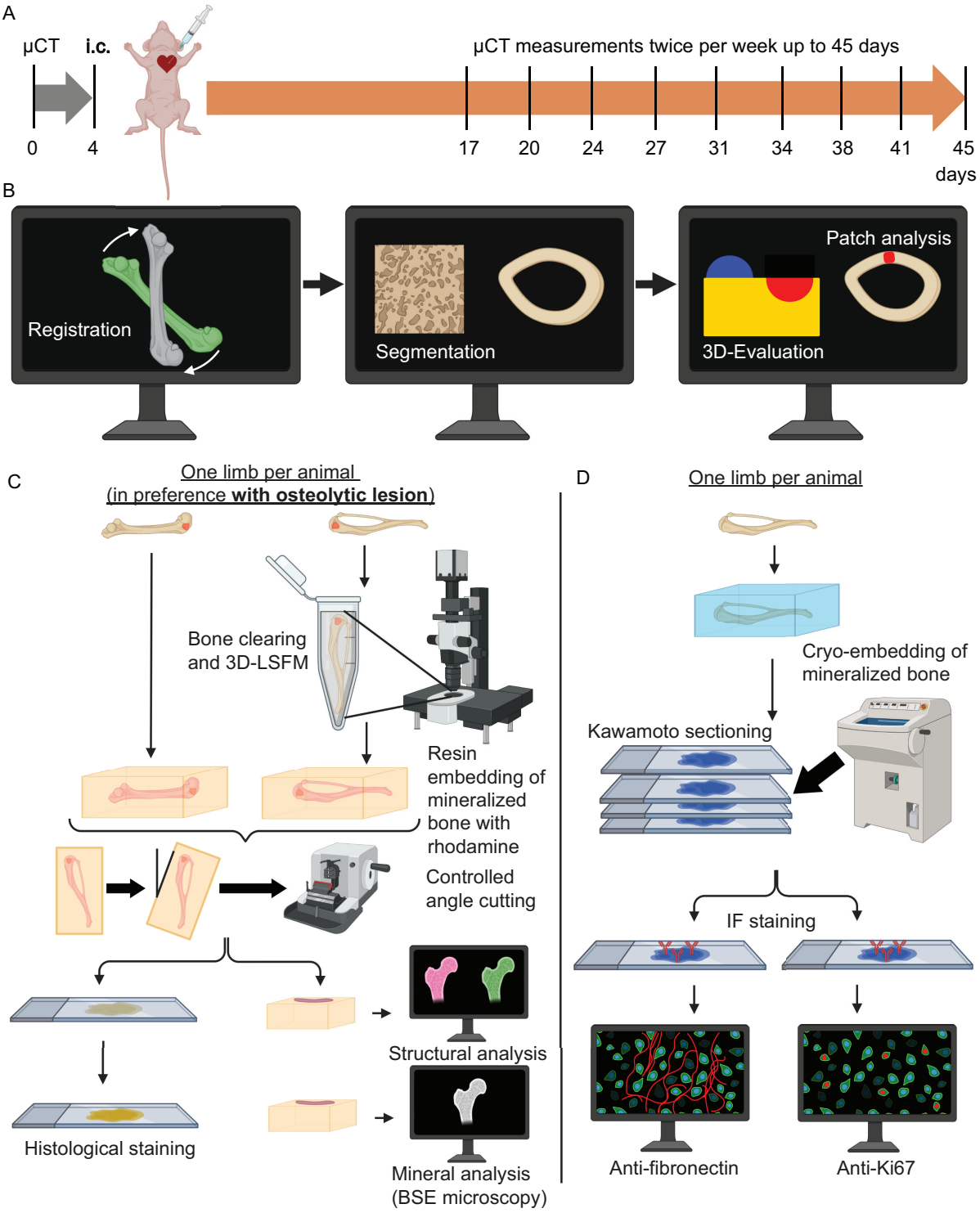

***Fig. 2.1: In vivo* and *ex vivo* workflow used for multiscale characterization.** (A) Schematic of the *in vivo* injection and monitoring with microCT twice per week for up to 45 days. (B) Depiction of the workflow for dynamic microCT-based time-lapse morphometry including registration, segmentation, evaluation and eroded bone patch analysis. (C) *Ex vivo* workflow for one limb per animal, preferably with an osteolytic lesions, including LSFM for tibiae, rhodamine staining and resin embedding of mineralized bones, controlled angle cutting, histological staining as well as structural and mineral analysis. (C) *Ex vivo* workflow for the other limb of each animal, including cryo-embedding of mineralized bones, Kawamoto sectioning and IF staining against FN and Ki67. (created with BioRender.com)

2.1 *In vivo* procedures

2.1.1 Animal model

12-week-old female BALB/c nude mice (CAnN.Cg-Foxn1nu/Crl, Charles River, Sulzfeld, Germany) were received and acclimatized in the animal facility of the Charité - Universitätsmedizin Berlin. The mice were housed 2-4 animals per cage with ad libitum access to food and water.

A reference microCT scan was acquired at day 0 and mice were injected after 4 days, under ultrasound guidance (Vevo2100, FUJIFILM VisualSonics Inc., Canada), into the left ventricle of the heart (one injection per mouse) using a 27 G needle. The mice used to study physiological bone (re)modeling (n = 7) were injected with PBS to ensure compatibility after this stressful procedure. Three additional mice were injected with PBS (n = 3) and sacrificed at day 17 for better comparison in *ex vivo* experiments with tumor animals, keeping the age of the animals and the exposure to radiation of the microCT as similar as possible. The tumor animals (n = 11) were injected with MDA-MB-231-1833 BoM cells (5×10^5 cells in 100 µL ice cold PBS). The animals received Carprofen (CP-Pharma Handelsgesellschaft mbH, Burgdorf, Germany) and Buprenorphin (CP-Pharma Handelsgesellschaft mbH, Burgdorf, Germany) as analgesic drugs during and after the injection. During longitudinal *in vivo* imaging and the intracardiac injection, the animals were anesthetized using isoflurane (CP-Pharma Handelsgesellschaft mbH, Burgdorf, Germany) at 1-2% with oxygen as a carrier and the eyes were protected from drying with Pan-Ophtal gel (Dr. Winzer Pharma GmbH, Berlin, Germany). The initial average animal weight was 19.7 g ± 1.7 g for PBS animals and 20.3 g ± 1.9 g for tumor animals. The weight at sacrifice for the PBS mice used to study physiological bone (re)modeling 45 days later was 19.6 g ± 2.1 g and 19.5 g ± 0.6 g for the animals sacrificed after 17 days. The weight at sacrifice for the tumor animals at the respective time points between day 17 and 38 was 19.2 g ± 2.0 g. All animal experiments were carried out according to the policies and procedures approved by local legal research animal welfare representatives (LAGeSo Berlin, G0224/18).

2.1.2 Cell culture

MDA-MB-231-1883 BoM cells were provided by Dr. Joan Massagué and purchased from the Antibody and Bioresource Core Facility of the Memorial Sloan Kettering Cancer Center, USA [81]. Briefly, MDA-MB-231 (ATCC ® HTB-26™) human epithelial breast cancer cells were stably transduced with

a lentivirus expressing a triple-fusion reporter, forming MDA-MB-231 TGL cells. The TGL reporter is a single fusion protein with three functional subunits under a single open reading frame. It allows the expression of green fluorescent protein (eGFP) (fluorescence), firefly luciferase (bioluminescence) and herpes virus 1 thymidine kinase (nuclear imaging technique)[104]. The here used subclone 1833 is a bone tropic human cell line derived from a metastasis formed by these MDA-MB-231 TGL cells hosted in a mouse[81]. MDA-MB-231-1883 BoM cells were cultured in low glucose Dulbecco's Modified Eagle's Medium (DMEM) (Sigma-Aldrich, Taufkirchen, Germany) supplemented with 1% penicillin/streptomycin (Gibco) and 10% fetal bovine serum (FBS superior, Sigma-Aldrich, Taufkirchen, Germany). The cells were grown at 37 °C with 5% CO_2 and regular passaging.

2.1.3 Longitudinal in vivo microcomputed tomography image acquisition

Longitudinal imaging of the hind limbs of the mice was performed with an *in vivo* high resolution microCT (U-CTHR, MILabs, Netherlands). The X-ray tube was operated at 50 kVp source voltage and 210 µA source current. Images were acquired at a step angle of 0.375° with 2 projections per step (75 ms exposure time), over a range of 360° and with 8.5 µm voxel size. Two aluminum filters with 100 µm and 400 µm thickness were used against beam hardening. The scan region included the entire femur and tibia of both hind limbs and was determined on an X-ray scout view. To prevent motion artifacts and ensure reproducibility, the anesthetized mice were positioned using an animal bed with the hindlimbs restrained. The scans were reconstructed using the MILabs Reconstruction software and a projection filter (Hann) was applied in the process to limit blurring. The scanner was calibrated before every scan using the internal calibration system. The animals were scanned with the microCT for a reference scan (day 0, 12-week-old). After 17 days, the animals were scanned twice per week up until maximum 45 days (on day 17, 20, 24, 27, 31, 34, 38, 41 and 45) as shown in Fig. 2.1 A. Anesthetized mice were sacrificed by cervical dislocation. The hind limbs were harvested and fixed with 4% paraformaldehyde (PFA) in PBS over night at 4 °C and stored in PBS until further processed.

2.1.4 Dynamic microcomputed tomography-based time-lapse morphometry

The analysis was performed in accordance with Birkhold et. al.[66] and Young et. al.[105]. To assess morphological changes due to physiological bone (re)modeling, microCT scans of time points once per week (day 17, 24, 31, 38 and 45) were compared to the reference scan at day 0 which ensures full in-

formation for all time points and no loss of events by changing the reference scan. In contrast, all time points (day 17, 20, 24, 27, 31, 34, 38, 41 and 45) were used to study differences in bone (re)modeling between tumor and control animals.

For physiological bone (re)modeling only the right limb of control animals injected with PBS were taken into account (n=6), while for the differences in bone (re)modeling of tumor and control mice, both limbs were used. The regions of interest (ROIs) were set at the distal femoral metaphysis and the proximal tibial metaphysis, reaching 10% of the total bone length. Each region of interest (ROI) started at the end of the non-mineralized growth plate, on the interface where the primary spongiosa of the metaphysis is found, reaching towards the diaphysis. The ROI included both primary and secondary spongiosa of the metaphysis (Fig. 3.2B, with epiphysis in light gray and metaphysis in dark gray). The entire epiphysis and other connected bones were manually segmented from the metaphysis. The threshold to remove the background was determined using the 3D Otsu-Method [106] (tool provided by Amira software, Amira 2020.1, Thermo Fisher Scientific, MA, USA) and a list of all used thresholds is reported in supplementary Table B.1, B.2, B.3, B.4 for healthy PBS animals and in Table B.5, B.6, B.7 and B.8 for tumor animals.

The registration process and following evaluation was performed in accordance with Birkhold et al. [66] and Young et al. [105]. The images were pre-processed and aligned using Amira. During the pre-processing step, the dataset was pre-cropped to the respective ROI. The epiphysis and other connected bones such as the fibula were removed by manual segmentation.

For the registration process, later time point images were registered onto the reference image (day 0) using a 3D rigid registration algorithm. The threshold determined as described above was used to exclude background noise from the registration, while keeping the gray scale of the respective bone region data set. A hierarchical strategy was chosen for the registration to avoid local minima, starting with coarse resampling and proceeding to finer resolutions under visual control to ensure correct registration. After the registration, the images were transformed into the same coordinate system using a Lanczos interpolation, keeping the voxel size constant. The images were then re-cropped according to the corresponding ROI.

The ROIs were then segmented into trabecular and cortical bone using morphological operations as described by Birkhold et al. [66] and evaluated, both using custom-made MATLAB (MATLAB 2018a; The Mathworks, Inc. Natick, MA, USA) scripts. Bone morphological changes were evaluated as previously described: MV/BV (normalized parameters are divided by the respective bone volume or bone

surface of the reference scan) shown in Fig. 2.2A in blue, normalized mineralized bone surface-to-soft tissue interface (MS_{ST}/BS) (newly introduced parameter from this work, Fig. 2.2B in lined blue), normalized mineralized bone surface-to-constant bone interface (MS_{CB}/BS) (Fig. 2.2C in hatched blue), MAR (mean thickness of formed bone in µm/day), EV/BV shown in Fig. 2.2A in red, normalized eroded bone surface-to-soft tissue interface (ES_{ST}/BS) (Fig. 2.2B in lined red), normalized eroded bone surface-to-constant bone interface (ES_{CB}/BS) (newly introduced parameter from this work, Fig. 2.2C in hatched red), as well as MRR (mean depth of resorbed bone in µm/days).

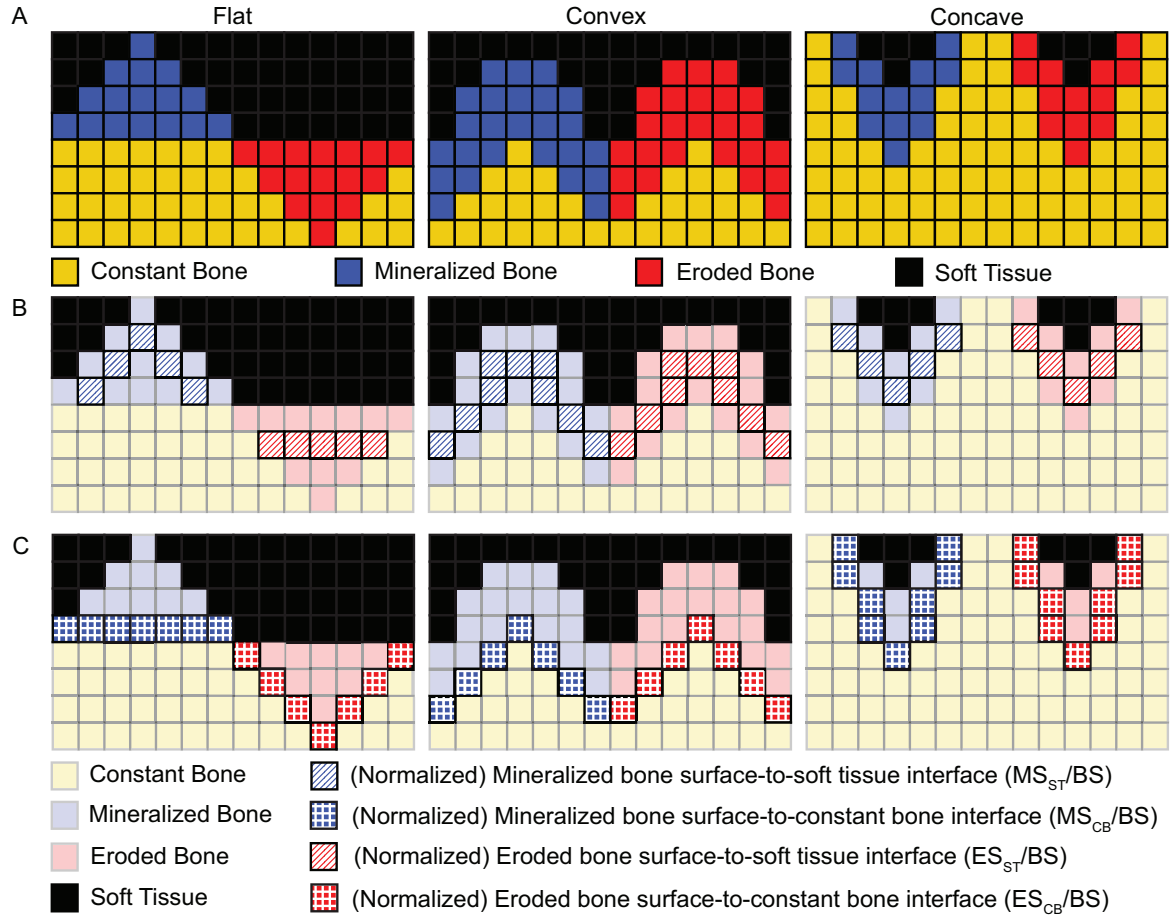

Fig. 2.2: **Sketch of how four distinct interfaces are strongly influenced by surface curvature.** (A) Schematic of the output of a microCT scan registration, with mineralized bone (blue) and eroded bone (red), constant bone (yellow) and soft tissue (black), on a flat, convex or concave surface. Different definitions of forming and resorbing bone surfaces on the interface with (B) soft tissue or with (C) constant bone, giving rise to two distinct normalized mineralized bone surfaces (MS_{ST}/BS and MS_{CB}/BS) and two distinct normalized eroded bone surfaces (ES_{ST}/BS and ES_{CB}/BS). The schematic shows constant bone (light yellow), mineralized bone (light blue), eroded bone (light red) and soft tissue (black), as well as MS_{ST}/BS (lined blue), MS_{CB}/BS (hatched blue), ES_{ST}/BS (lined red) and ES_{CB}/BS (hatched red).[105]

Briefly, for each case only the concerning voxels, being labeled as constant, mineralized or eroded voxels, were taken into consideration. The first layer of voxels was disregarded due to partial volume

effects, leaving the second most outward layer of voxels to be considered as the soft tissue interface, while the constant bone interface was evaluated by expanding the constant bone surface by one voxel. For the surface evaluation only one layer of voxels was taken into account, while all voxels were counted for volume evaluations. The different interfaces giving rise to the four distinct surfaces were calculated independently of each other and can thus in specific cases contain the same voxels, as depicted in Fig. 2.2 B and C. The description of the surfaces is not influencing the analysis of volumetric parameters, which are calculated from all bone voxels independently. A list of all parameters with definition and unit is provided in Table 2.1.

Tab. 2.1: List of abbreviations used in dynamic microCT-based time-lapse bone morphometry with definition and unit.

Abbreviation	**Definition**	**Unit**
MV/BV	Normalized mineralized bone volume	-
EV/BV	Normalized eroded bone volume	-
MS/BS	Normalized mineralized bone surface	-
MS_{ST}/BS	Normalized mineralized bone surface-to-soft tissue interface	-
MS_{CB}/BS	Normalized mineralized bone surface-to-constant bone interface	-
ES/BS	Normalized eroded bone surface	-
ES_{ST}/BS	Normalized eroded bone surface-to-soft tissue interface	-
ES_{CB}/BS	Normalized eroded bone surface-to-constant bone interface	-
MAR	Mineral apposition rate	µm day^{-1}
MRR	Mineral resorption rate	µm day^{-1}

2.1.5 Analysis of spatial gradients in bone (re)modeling using dynamic microcomputed tomography-based time-lapse morphometry

Both the distal femoral metaphysis and the proximal tibial metaphysis cortical bone regions were used for the spatial analysis of bone morphological changes in control animals with physiological bone (re)modeling. The femoral and tibial metaphysis (without the epiphysis) were discretized into intervals spanning 100 µm, starting at 400 µm from the end of the non-mineralized growth plate (on the interface with the primary spongiosa), reaching towards the diaphysis and ending at 1,400 µm (resulting in 10 intervals), thereby covering nearly the entire ROI corresponding to 10% of the total bone length. The dynamic morphometry parameters were evaluated for each section separately at day 45 (with day 0 as a reference).

2.1.6 Reproducibility of image processing

A precision analysis of the microCT (U-CTHR, MILabs, Netherlands) was performed based on *ex vivo* microCT scans. It has been shown that the reproducibility of *in vivo* and *ex vivo* scans is comparable [107]. The scans were performed on whole mice with intact limbs in order to get as close to the *in vivo* conditions as possible. The tibiae of three mice (n = 6 bones) were scanned four times each using the same settings as for the *in vivo* scans. Mice were re-positioned after each scan. The results for the metaphysis are shown in Table B.9, and for the epiphysis in Table B.10 [105].
All possible combinations of registration, (n – 1)! with n being the number of scans were performed. We then calculated mean, standard deviation (SD), the absolute precision error (PE_{SD}) and the precision error as coefficient of variation (PE_{CV}) in % as well as the confidence interval (CI) (using a chi-squared distribution, with df as the total degrees of freedom). The analysis was done for both cortical and trabecular bone volume and surface parameters [66] [108].

2.1.7 Osteolytic lesions in cortical bone: Eroded bone patch detection and volume analysis

To detect and analyze the volume of osteolytic lesions in cortical bone with dynamic microCT-based time-lapse morphometry data, a new mathematical evaluation tool was established that had the ability to differentiate between physiological erosion and pathological erosion patches in the cortical bone. Only eroded voxels of previously segmented cortical bone were taken into account for this procedure.

A chosen 3D neighborhood of each eroded voxel was evaluated, meaning that the status of surrounding voxels – being eroded or not eroded – and the voxel itself were considered and summed leading to a sum matrix as depicted in 2D as an example in Fig. 2.3A.

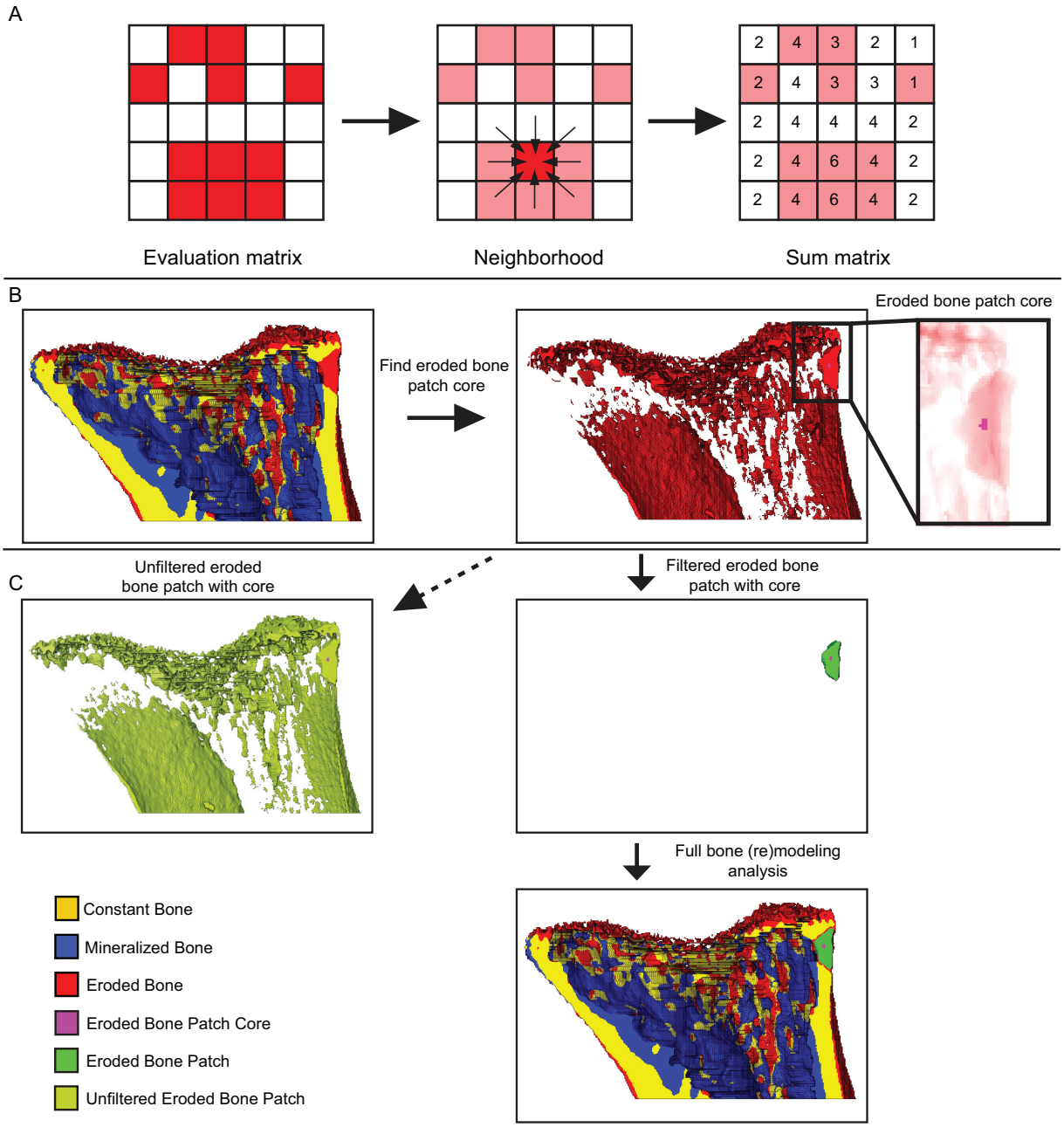

***Fig. 2.3:* Sketch of the eroded bone patch analysis.** (A) Schematic explaining how the neighborhood is determined, starting at the evaluation matrix, showing a 2D simplified 3×3 neighborhood for one voxel and the thereof resulting sum matrix. (B) Eroded bone patch core analysis: starting with the (re)modeled bone and detecting the eroded bone patch core. (C) Then filtering for the entire patch (green) while excluding unrelated erosion zones (light green). Constant bone is shown in yellow, mineralized bone in blue, eroded bone in red, eroded bone patch core in pink, eroded bone patch in green and unfiltered eroded bone patch in light green.

Two different empirically determined thresholds were applied to a) detect the eroded bone patch core

(the main criteria to determine whether or not an animal has a lesion) and b) analyze the volume of the entire eroded bone patch.

To detect the eroded bone patch core of only pathological erosions, the neighborhood of each eroded voxel was explored in 9×9×4 voxels in x, y and z. If a threshold of 92.61% was fulfilled, meaning that 92.61% of the neighborhood voxels were erosion voxels, that voxel was identified as belonging to the eroded bone patch core, as shown in Fig. 2.3B with the eroded bone patch core in pink. The parameters were determined empirically by testing visually detected lesions and data from healthy control animals.

To analyze the volume of the eroded bone patch, the noise in form of scattered eroded voxels around the eroded bone patch core was filtered (Fig. 2.3C, unfiltered noise in light green): To do so, the neighborhood of each eroded voxel was explored in 3×3×3 voxels in x, y and z. If a threshold of 70% was fulfilled, those erosion voxels were maintained and contributed to the volume of the eroded bone patch (Fig. 2.3C, eroded bone patch volume in green with patch core in pink). The threshold parameters were determined empirically under visual control.

The volume of each eroded bone patch in mm^3 was obtained at different time points. The location of osteolytic lesions was visualized with the eroded bone patch core shown in pink and the respective entire patch in green.

2.1.8 Microcomputed tomography based static bone analysis

Static bone analysis was performed for physiological bone (re)modeling on the pre-processed images for time points 0, 17, 24, 31, 38 and 45 to confirm the findings of the dynamic microCT-based time-lapse morphometry analysis. The separation of cortical and trabecular bone was achieved with the help of morphological operations, using the same steps as for the dynamic analysis and described by Birkhold et al. [66]. The used parameters include TV, BV, and BV/TV for both cortical and trabecular bone, as well as BS/BV for cortical bone. The parameters were calculated in MATLAB following the standard procedures as described by Bouxsein et al. [25]. Briefly, for cortical bone, TV was calculated as the entire mineralized bone and marrow volumes, while BV encompassed the mineralized tissue volume of the cortical bone. In trabecular bone, TV was calculated as the entire bone marrow volume, while BV covered the mineralized part of this volume.

2.1.9 Code availability

The original code as well as the modified versions used in this study are available on GitHub.
https://github.com/BWillieLab/Timelapse-Morphometry (original code)
https://github.com/CipitriaLab/Timelapse-Morphometry (modified code used for the work published by Young et al.[105])
A third version of the code including the eroded bone patch detection and volume analysis tool will be provided on the same platform after publication.

2.1.10 Statistical analysis in physiological bone (re)modeling measured with microcomputed tomography

The right femur and tibia of six control animals were used for statistical evaluation. The plots show the mean and standard deviation. Normal distribution of the data was confirmed with the help of quartile-quartile plots. Paired t-tests were used for statistical comparison between different regions and parameters with significant differences presented as * $p \leq 0.05$, ** $p \leq 0.01$ and *** $p \leq 0.001$. Origin 2021b (OriginLab, Northampton, US) was used to plot the data and for statistical analysis. (This study was published before all animal experiments were completed, therefore containing only a part of the overall collected data[105].)

2.1.11 Statistical analysis in pathological bone (re)modeling measured with microcomputed tomography

When comparing PBS controls with tumor animals, only bones harvested from animals without detectable osteolytic lesions were included for the latter. All bones harvested from animals with confirmed lesions were excluded from microCT analysis. Both limbs of all animals were considered, resulting in seven control animals with $n = 14$ bones and 5 tumor animals with $n = 10$ bones. The plots show the mean and standard deviation. Normal distribution of the data was confirmed with the help of quartile-quartile plots. Two sample t-tests were used for statistical comparison between different groups and parameters with significant differences presented as * $p \leq 0.05$. In addition, the 95% confidence interval is shown for all parameters and time points. Origin 2021b was used to plot the data and for statistical analysis.

2.2 *Ex vivo* procedures

2.2.1 Optical clearing and light-sheet fluorescence microscopy of tibiae

Fixed tibiae were dehydrated in an ascending ethanol series (50, 70 and two times in 100%) for 12 h each at room temperature and cleared with ethyl cinnamate (Sigma-Aldrich, Taufkirchen, Germany) at room temperature for 24 h according to the simpleCLEAR protocol[18].

To image cleared tibiae via LSFM, a LaVision BioTec Ultramicroscope Blaze (Miltenyi/LaVision BioTec, Bielefeld, Germany) with a supercontinuum white light laser (460-800nm), 7 individual combinable excitation and emission filters covering 450 – 865 nm, an AndorNeo sCMOS Camera with a pixel size of 6.5 µm^3, and 1.1× (NA 0.1), 4× (NA 0.35), 12× (NA 0.53) objectives with a magnification changer ranging from 0.66× to 30× was used. For image acquisition, cleared samples were immersed in ethyl cinnamate in a quartz cuvette and excited at 470/30 nm for eGFP-excitation and 560/40 nm for tissue autofluorescence excitation. eGFP was detected using a 525/50 nm band-pass emission filter and a 620/60 nm band-pass emission filter was used for tissue autofluorescence detection. Because the excitation optics of the microscope provide a light-sheet thickness of 4 – 24 µm (adjustable NA), the Z-step size was set to 5 or 10 µm depending on the selected light-sheet NA. The optical zoom factor varied from 1.66× to 4× depending on the objectives and digital zoom factors used.

Imaris (Bitplane, Version 9.6.0, Oxford Instruments, Abingdon, UK) was used for data analysis. The bone marrow was segmented manually and the cells were analyzed using the spots tool with an initial estimated diameter of 35.5 µm, that was found by manually measuring around 10 cells. Cellular patches on the periosteum were also segmented manually and analyzed using the spots tool with an initial estimated diameter of 20 µm that was found by manually measuring around 10 cells. N = 5 bones from five different animals were analyzed.

The clearing protocol was reversed by placing samples in a descending ethanol series (100, 70, 50%) with 1% Tween-20 for 5h at room temperature each, followed by two steps in PBS with 1% Tween-20 (5h at room temperature each). The samples were stored in PBS until further usage.

2.2.2 Resin embedding of mineralized bone tissue

Bone specimens were cold embedded at 4 °C in poly(methyl methacrylate) (PMMA) (Technovit 9100, Kulzer, Germany), following the manufacturer's instructions. Briefly, samples were dehydrated in an

ascending ethanol series (70, 80, 96 and 100%) for 48 h at 4 °C each with a final step in rhodamine solution (4.17 mg mL^{-1} Rhodamine B, pure in 100% ethanol, ACROS Organics, Geel, Belgium), followed by a xylene washing (two times for 3 h each at room temperature), pre-infiltration and infiltration for 48 h each at 4 °C and embedding in PMMA for up to 7 days at −20 °C.

2.2.3 Sectioning of resin embedded bones using controlled angle cutting and *ex vivo* microcomputed tomography

In order to expose the metastatic osteolytic lesion, we used controlled angle cutting as described by Moreno-Jimenez et al.[109]. The excess PMMA was first trimmed and the entire block scanned with an *ex vivo* microCT scanner (EasyTom micro/nano tomograph RX solutions, France) at a low resolution with 15 µm voxel size and acquisition parameters of 107 kV, 93 µA, frame rate of 6 and average frame of 5. Reconstruction of the 800 projections/scan were performed using RX Solutions X-Act software. The cutting plane to capture the metastatic osteolytic lesion was found using Data Viewer (Bruker, Kontich, Belgium) by rotating the block around the x and z axis. For small correction angles under 20°, a tilted cylinder was cut and the sample blocks were fixed on it for sectioning. For larger correction angles over 20°, an additional cut of the block was performed with a diamond wire saw (DWS.100, Diamond WireTec GmbH & Co.KG, Weinheim, Germany) and a second microCT scan was performed, repeating the same procedure as above. The histological sections were taken at a thickness of 6 µm with a microtome (Leica RM2255 Microtome, Leica Biosystems, Wetzlar, Germany).

2.2.4 Movat's Pentachrome staining

The PMMA embedded sections were stained using a standard protocol of Movat's Pentachrome performed fully at room temperature. In short, sections were deplastified in 2-methoxyethyl acetate (MEA) (Morphisto GmbH, Offenbach am Main, Germany) three times for 20min each and rehydrated in a descending ethanol series (100, 96, 80 and 70% twice for 2 min each). The samples were then stained with 1% alcian blue (Alcian blue 8GX, Alfa Aesar, Haverhill, US) in 3% acetic acid (Carl Roth, Karlsruhe, Germany) and transferred into a basic environment by incubating in alkaline ethanol (96% ethanol with ammonia 9:1) for 1 h. The samples were washed in tap water for 10 min and then stained with Weigert's haematoxylin (Solution A and B Set, 1:1 mixture, Sigma-Aldrich, Taufkirchen, Germany) for 10 min, followed by an additional washing step. Next, the samples were stained with brilliant crocein 1 mg mL^{-1} (Waldeck GmbH & Co. KG, Münster, Germany) and acid

fuchsin 1 mg mL^{-1} (Waldeck GmbH & Co. KG, Münster, Germany) mixed at a ratio of 4:1 for 15 min, followed by a washing step in 5% phosphotungstic acid (Waldeck GmbH & Co. KG, Münster, Germany) for 5 min. The samples were dehydrated in an ascending ethanol series (70, 80, 96% twice for 2 min each) and a final staining with saffron du Gâtinais (60 mg mL^{-1} in 100% ethanol, Waldeck GmbH & Co. KG, Münster, Germany) for 1 h was performed. The sections were incubated in 100% ethanol for 3 min twice, followed by incubation in xylene twice for 2 min and mounted with mounting media (VITROCLUD, deltalab, Barcelona, Spain). The stained sections were imaged with a Keyence Digital Microscope (VKX-5550E, Keyence, Germany). The following tissue types were stained: mineralized bone and collagen (yellow), cartilage (blue/green), fibrin and muscle (red), cell nuclei (black).

2.2.5 Haematoxylin and eosin staining

The PMMA embedded sections were stained using a standard protocol of haematoxylin and eosin (H&E) (H&E Rapid kit, Clin-Tech, Surrey, UK). In short, sections were rehydrated in a descending ethanol series (100, 96, 80 and 70% twice for 2 min each), washed in tap water, followed by staining in Carazzi's double-strength haematoxylin for 1 min. After another wash in tap water, the slides were stained in eosin for 30 s, rinsed in tap water, dehydrated in an ascending ethanol series (70, 80, 96, 100% twice for 2 min each), incubated in xylene twice for 2 min and mounted (VITROCLUD, deltalab, Barcelona, Spain). The stained sections were imaged with a Keyence Digital Microscope (VKX-5550E, Keyence, Germany). Mineralized tissue and nuclei are shown in dark purple, while soft tissue is shown in light purple.

2.2.6 Tartrate-resistant acid phosphatase staining

The PMMA embedded sections were stained using a standard protocol of tartrate-resistant acid phosphatase (TRAP) staining. In short, sections were deplastified in MEA three times for 20 min each and rehydrated in a descending ethanol series (100, 96, 80 and 70% twice for 2 min each). Samples were then incubated in TRAP buffer (sodium acetate 40 mM, VWR, Radnor, US, and disodium tartrate dihydrate 10 mM, Merck KGaA, Darmstadt, Germany) for 10 min at room temperature, followed by an incubation in pre-warmed TRAP staining solution (in TRAP buffer, naphthol AS-MX-phosphate 0.2 mg mL^{-1}, Sigma-Aldrich, Taufkirchen, Germany, fast red violet LB salt 1.2 mg mL^{-1}, Sigma-Aldrich, Taufkirchen, Germany, N,N-dimethlyformamid 2%, Sigma-Aldrich, Taufkirchen, Germany and Triton X 1%, Thermo Fisher Scientific, Waltham, US) at 37 °C for 2 h under repeated vi-

sual control to ensure appropriate incubation until the staining was well developed. The sections were washed in water, counter stained with Mayer's haematoxylin (Sigma Aldrich, Taufkirchen, Germany) for 2 min followed by washing in 0.1% ammonium hydroxide for 30 s. For visualization of the bone structure, sections were incubated in aniline blue solution (aniline blue 0.4 mg mL^{-1}, phosphotungstic acid 12 mg mL^{-1}, Carl Roth, Karlsruhe, Germany) for 20 min at room temperature. The sections were blotted to remove access liquid, followed by xylene incubation twice for 2 min and mounted with mounting media (VITROCLUD, deltalab, Barcelona, Spain). The stained sections were imaged with a Keyence Digital Microscope (VKX-5550E, Keyence, Germany). Osteoclasts are shown in pink, nuclei in pale blue and bone tissue in blue.

2.2.7 Confocal laser scanning microscopy fluorescence imaging

After sectioning, the exposed PMMA block surface was polished (PM5, Logitech, Glasgow, Scotland) with abrasive paper 4000 with grading of 5 µm and with 3 µm and 1 µm diamond spray under constant visual control, ensuring that only minimal tissue got removed. The block surface of the rhodamine stained samples was imaged using CLSM (Leica TCS SP8 DLS, Multiphoton, Leica Microsystems CMS GmbH, Wetzlar, Germany). The samples were images with a HC PL APO CS2 40×/1.30 oil objective (NA 1.3) at a magnification of 40×. Argon laser light with $\lambda_{excitation} =$ 514 nm / $\lambda_{emission} =$ 550 – 650 nm was used with a laser intensity of 10%. Images were acquired with a resolution of 1024 pixels by 1024 pixels (pixel size of 284 nm) at a scan speed of 400 Hz. Over 100 images for each sample with a thickness of 347 nm, spanning a changing thickness of around 50 µm depth from the block surface were imaged. To compensate for the loss of signal during scanning along the depth, the photomultiplier gain was continuously increased. The images were stitched and visualized with the LAS X software (Version 3.5.7.23225, Leica Microsystems CMS GmbH, Wetzlar, Germany). For each animal, a region containing an osteolytic lesion, either in the cortical or trabecular bone, and a lesion-free region in the same bone at a comparable location were imaged. N = 5 bones from five different animals were analyzed.

2.2.8 Second harmonic generation imaging

SHG imaging was performed on the exact same ROI with the same instrument and objective. A pulsed infrared laser ($\lambda_{excitation} =$ 910 nm/ $\lambda_{emission} =$ 450 – 460 nm) with a power of 0.6 W and an intensity of 10% was used. Images were acquired with a resolution of 1024 pixels by 1024 pixels (pixel size of

284 nm) at a scan speed of 400 Hz. Around 20 images with a thickness of 2.758 µm were made keeping the same total depth as for the previous image of rhodamine staining and fluorescence imaging. For each animal a region containing an osteolytic lesion, either in the cortical or trabecular bone, and a lesion-free region at a comparable location were imaged. The images were stitched and visualized with the LAS X software (Version 3.5.7.23225, Leica Microsystems CMS GmbH, Wetzlar, Germany). N = 5 bones from five different animals were analyzed.

2.2.9 Backscattered electron microscopy

The polished PMMA block surface of the samples was imaged with an environmental scanning electron microscope (Quattro ESEM, Thermo Fisher Scientific, Waltham, US) in backscattered electron mode. The following settings were used: 15 kV, low vacuum conditions (100 Pa), working distance of approximately 8 mm, spot size of 3 and 500× magnification. The images were manually stitched using Adobe Photoshop 2022. N = 5 bones from five animals were analyzed.

2.2.10 Cryo-embedding and -sectioning of mineralized bone tissue

Bones of one limb of each mouse without a detectable osteolytic lesion were freeze embedded following the method of the SECTION-LAB Co. Ltd. (Hiroshima, Japan). Briefly, the samples were dehydrated in an ascending sucrose solution (10%, 20% and 30% in distilled water) for 24 h each at 4 °C. Next, a metal mold was placed in isopropanol cooled with liquid nitrogen and filled with embedding medium (SCEM; SECTION-LAB Co. Ltd., Hiroshima, Japan). The bone was placed in the middle and covered it with embedding medium, avoiding direct contact with the cooled isopropanol. Samples were stored at −80 °C until further usage. Cryosections with a thickness of 20 µm were cut following the Kawamoto method using a cryostat (Leica CM3060S, Leica Microsystems CMS GmbH, Wetzlar, Germany). The sections were collected using Kawamoto films (type 2C(9), SECTION-LAB Co. Ltd., Hiroshima, Japan), then attached to a microscopic slide and stored at -20°C until further use.

2.2.11 Histological immunofluorescence staining and imaging

For IF staining the slides were blocked with blocking buffer (1%bovine serum albumin (BSA), Sigma-Aldrich, Taufkirchen, Germany, 0.1%Tween20 Carl Roth, Karlsruhe, Germany, 0.1% dimethyl sulfoxide (DMSO), Merck KGaA, Darmstadt, Germany in PBS) for 1 h. Primary and secondary antibodies were diluted in blocking buffer and incubated for at least 4 h at room temperature or over night

at 4 °C, with in between washing steps (three times, 15 min each) in washing buffer (0.1%Tween20, 0.1% DMSO in PBS). Final washing steps were conducted in washing buffer (twice for 15 min) and in distilled water (once for 15 min). Slides were then mounted with Dako fluorescence mounting media (S302380-2, Agilent Technologies, Santa Clara, US). The primary antibodies and respective concentrations used in this study are the following: 4',6-diamidino-2-phenylindole (DAPI) (1:500, Roche), anti-Ki67 (1:100, ab45580, abcam) and anti-FN (1:200, ab23750, abcam). As secondary antibody Alexa Fluor 555 (1:1000, A-21429, abcam) was used. Samples were imaged using CLSM (Leica TCS SP8 DLS, Multiphoton, Leica Microsystems CMS GmbH, Wetzlar, Germany).

Three different objectives were used: HC APO L 10x/0.30 water objective (NA 0.3) at a magnification of 10×, HC PL APO CS2 40×/1.30 oil objective (NA 1.3) at a magnification of 40×, HC PL APO CS2 63x/1.40 oil objective (NA 1.4) at a magnification of 63×. For imaging the DAPI, Diode 405 laser light with $\lambda_{excitation} =$ 405 nm $/\lambda_{emission} =$ 410 – 483 nm was used. For imaging the eGFP, argon laser light with $\lambda_{excitation} =$ 488 nm $/\lambda_{emission} =$ 493 – 556 nm laser light was used. For imaging the Alexa Fluor 555, DPSS 561 laser light with $\lambda_{excitation} =$ 561 nm $/\lambda_{emission} =$ 566 – 756 nm laser light was used. Laser intensity and photomultiplier gain were kept constant: DAPI (intensity 1%, HyD detector, gain 150 and 25 for higher magnifications), eGFP (intensity 20%, PMT detector, gain 900), Alexa Fluor 555 (intensity 1%, HyD detector, gain 100 and 60 for higher magnifications). Images were acquired with a resolution of 1024 pixels by 1024 pixels (pixel size of 284 nm) at a scan speed of 400 Hz (200 Hz for 63× magnification), and a varying number of images with a thickness of 4 µm (2 µm for 63× magnification) were made over a depth of around 20 µm. For 10× and 40× magnification, tile scans depending on the size of the sample were acquired.

Images were analyzed using ImageJ (40× magnification images were used for quantification), thresholds were applied manually under visual control and cells/clusters were manually counted and categorized using the cell counter tool. Images were visualized with Imaris (Imaris Viewer 9.8.0, Oxford Instruments, Abingdon, United Kingdom). N = 4 bones from four animals were analyzed.

2.2.12 Sample size in *ex vivo* procedures

The bones used for the different analyses, including their sacrifice time point, detected lesions and methods used are depicted in Fig. 2.4.

Five tibiae from five different animals were optically cleared, measured with LSFM and used for the analysis of cancer cells homing in the bone marrow (one additional animal was excluded due to a larger

osteolytic lesion). Three of these tibiae had detected osteolytic lesions in either cortical or trabecular bone (Fig. 2.4, animal 1, 2, 3), one tibia was from an animal with an osteolytic lesion in the corresponding femur (Fig. 2.4, animal 4) and one animal did not present any detectable osteolytic lesion (Fig. 2.4, animal 7).

Five bones from five different animals were resin-embedded and imaged for lesion analysis with CLSM after rhodamine staining and with SHG imaging. Four tibiae (Fig. 2.4, animal 1, 2, 3, 6) and one femur (Fig. 2.4, animal 4) were imaged. All these bones had an osteolytic lesion in either cortical or trabecular bone detected with microCT.

Four tibiae from four different animals were cryo-embedded, stained with IF and imaged using CLSM. All animals had at least one osteolytic lesions in one of the long bones. Three tibiae had no detectable lesion (Fig. 2.4, animal 1, 3, 4), while one tibia had a lesion in the trabecular bone (Fig. 2.4, animal 2).

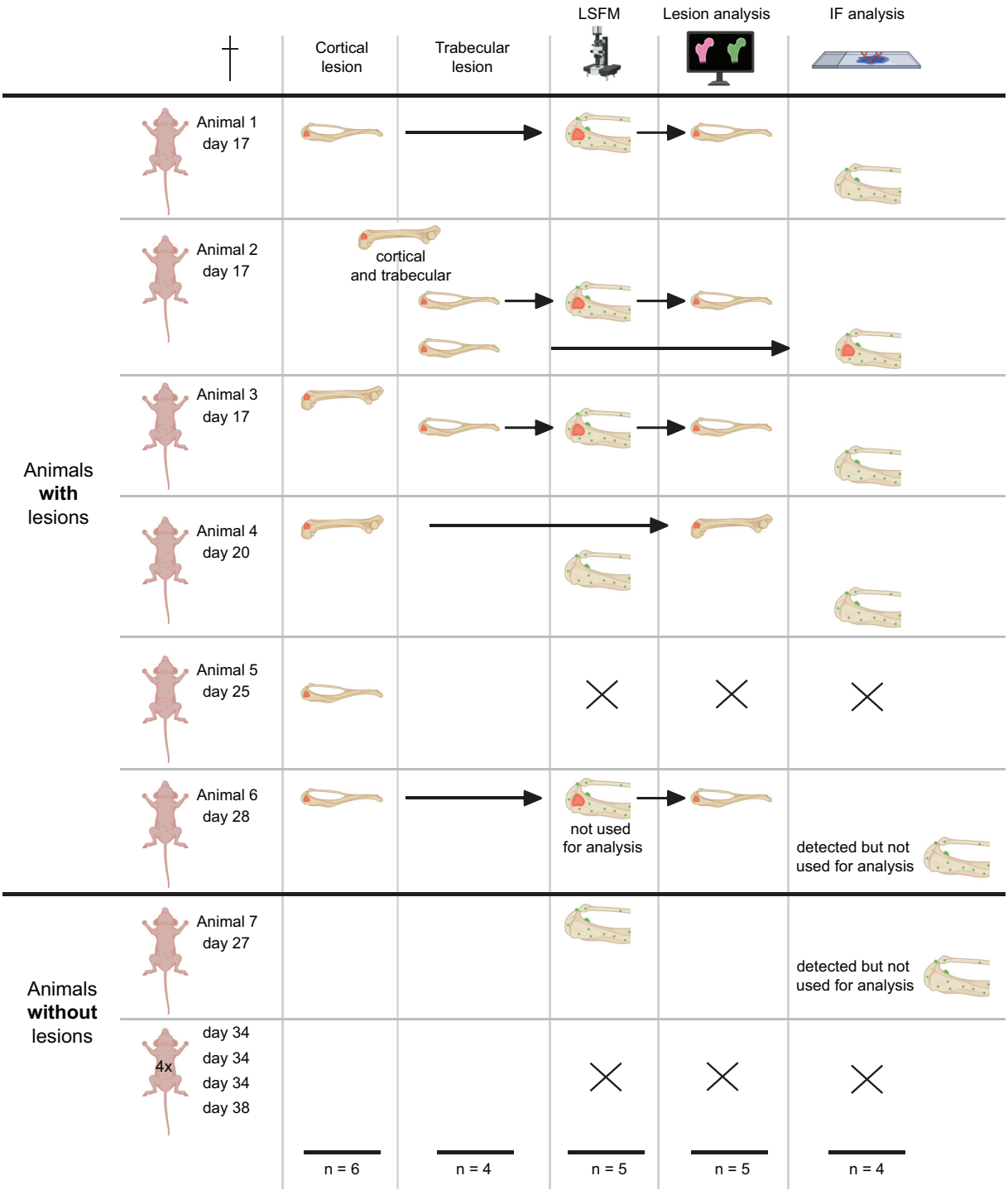

Fig. 2.4: **Depiction of the samples used in the *ex vivo* experiments determined by the *in vivo* results** Schematic shows the sacrifice time point for each animal and the number of bones used (as indicated by the row). Bones with lesions are depicted with a red hole, while bones with detected cancer cells are depicted with green dots. A final number of bones used per technique is shown below. (created with BioRender.com)

CHAPTER 3

Results

In this work we aimed at developing an experimental mouse model of breast cancer bone metastasis for the 3D visualization and characterization of the early bone metastatic niche. With this model we wanted to study pathological alterations in bone (re)modeling in the absence and presence of osteolytic lesions and changes in the bone microenvironment harboring the cancer cell niche.
The results are structured into two parts, starting with the *in vivo* work, using mainly microCT-based methods to study both physiological and pathological bone (re)modeling and the detection and analysis of osteolytic lesions.

3.1 Healthy bone (re)modeling baseline

Physiological bone (re)modeling was studied with the help of dynamic microCT-based time-lapse morphometry to create a baseline for further studies on pathological alterations. New surface parameters were introduced and we could show how they were affected by bone curvature. In addition, region specific temporal differences in epiphysis and metaphysis as well as tibia and femur were shown, including a spatial analysis and direct comparison to static microCT characterization.

3.1.1 An extension of the bone surface parameters and the influence of curvature on these interfaces

In dynamic microCT-based time-lapse bone morphometry analysis of cortical and trabecular bone, different definitions of mineralized and eroded surfaces can be used. Fig. 2.2A depicts the outcome

of this analysis with mineralized bone in blue, eroded bone in red and constant bone in yellow for a flat, convex and concave structure. Fig. 2.2B and C illustrate the four distinct surfaces that can be derived. We distinguished between mineralized (light blue) and eroded (light red) bone, and its interface to bone volumes that stayed constant (light yellow) or to surrounding soft tissue (black). The four distinct surfaces are the following:

- normalized mineralized bone surface-to-soft tissue interface (MS_{ST}/BS) (lined blue)
- normalized mineralized bone surface-to-constant bone interface (MS_{CB}/BS) (hatched blue)
- normalized eroded bone surface-to-soft tissue interface (ES_{ST}/BS) (lined red)
- normalized eroded bone surface-to-constant bone interface (ES_{CB}/BS) (hatched red)

MS_{CB}/BS and ES_{ST}/BS were included in the original model by Birkhold et al.[66]. MS_{ST}/BS and ES_{CB}/BS have been introduced in the current work by Young et al.[105] and provide a more complete description of the different mineralized and eroded surfaces. Further, this has a clear impact in the results, as it will be described in the following paragraphs.
Those surfaces are strongly influenced by the local curvature of the bone. The (re)modeling of bone is often depicted on a flat surface, where the mineralization is seen as a hill, leading to a larger MS_{ST}/BS as it is covering the hill, while the MS_{CB}/BS goes along the bottom of the hill and is therefore smaller. Similarly, the erosion is seen as a valley, with the ES_{ST}/BS covering the top of the valley and thus being smaller than the ES_{CB}/BS which is running alongside the valley. The schemes in Fig. 2.2B and C show how these surfaces are changing depending on the curvature (convex or concave) of the bone. On a convex surface, the soft tissue interface (MS_{ST}/BS and ES_{ST}/BS) is larger than the constant bone interface (MS_{CB}/BS and ES_{CB}/BS), while the opposite is true for a concave surface.

- Flat: $MS_{ST}/BS > MS_{CB}/BS$ and $ES_{CB}/BS > ES_{ST}/BS$
- Convex: $MS_{ST}/BS > MS_{CB}/BS$ and $ES_{ST}/BS > ES_{CB}/BS$
- Concave: $MS_{CB}/BS > MS_{ST}/BS$ and $ES_{CB}/BS > ES_{ST}/BS$

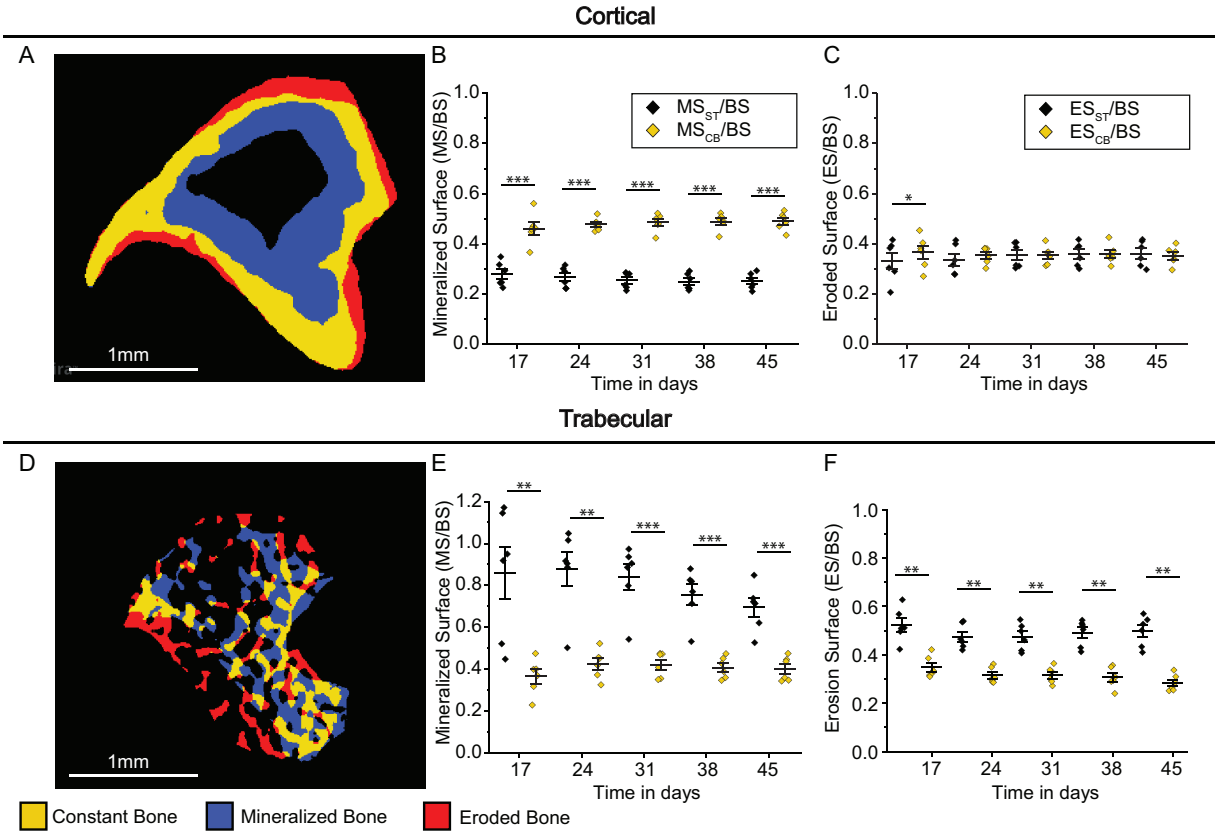

***Fig. 3.1:* Analysis of bone mineralization and erosion on four distinct interfaces that are strongly influenced by surface curvature.** (A) Evaluation of cortical bone (re)modeling (with constant bone in yellow, mineralized bone in blue and eroded bone in red, day 31). Shown are normalized (B) mineralized and (C) eroded surface over time, on the interface with constant bone (yellow) or with soft tissue (black). (D) Evaluation of trabecular bone (re)modeling. Shown are normalized (E) mineralized and (F) eroded surface over time, on the interface with constant bone (yellow) or with soft tissue (black). (All plots show mean and standard deviation, with statistically significant values presented as $*$ $p \leq 0.05$, $**$ $p \leq 0.01$ and $***$ $p \leq 0.001$. N = 6 bones from six control animals.) [105]

The results of the surface analysis are shown in Fig. 3.1 for healthy control animals. In the cross sections of tibia cortical (Fig. 3.1A) and trabecular (Fig. 3.1D) bone, constant bone is depicted in yellow, mineralized bone in blue and eroded bone in red. The evaluation of mineralized and eroded bone surfaces on four distinct interfaces is shown for cortical bone (Fig. 3.1B and C) and for trabecular bone (Fig. 3.1E and F). The data plotted over time for soft tissue interfaces (MS_{ST}/BS and ES_{ST}/BS) is shown in black, while constant bone interfaces (MS_{CB}/BS and ES_{CB}/BS) are shown in yellow. The plots show how the respective surfaces significantly differ from each other at each time point.

In the cortical compartment depicted in Fig. 3.1A, mineralization occurs mostly in the endocortical region which has a concave curvature. Therefore, the mineralized surface MS_{ST}/BS is significantly smaller than the MS_{CB}/BS (Fig. 3.1B). The values stay constant over time for both interfaces between day 17 and day 45. Erosion on the other hand, occurs mostly on the periosteal region, which

has both concave and convex surfaces (Fig. 3.1A). Consequently, the results show very similar values for both interfaces (ES_{ST}/BS and ES_{CB}/BS), with values remaining constant over time (Fig. 3.1 C). In the trabecular compartment a lot of (re)modeling can be observed which leads to an overall smaller interface with constant bone (Fig. 3.1D). Consequently, the interface with the constant bone is smaller for both mineralization (Fig. 3.1E) and erosion (Fig. 3.1F). This effect is even stronger in the mineralized bone and a constant decrease of MS_{ST}/BS from maximum 120% to 90% can be observed, while all other three surfaces stay constant over time. In trabecular bone, the main influence on the results for different interfaces is thus not the curvature (which presents both concave and convex regions), but the amount of existing constant bone, as trabecular bone is highly (re)modeled.

We were able to show, that surface (re)modeling parameters are strongly influenced by the curvature of the bone, especially in cortical bone. Therefore, all four distinct surfaces should be described to ensure a complete picture of the (re)modeling processes.

3.1.2 Different bone (re)modeling patterns are observed within tibial metaphysis and epiphysis

Even past sexual maturity (6-8 weeks of age) longitudinal growth continues in mice, though at a much slower rate, and the growth plate never fuses completely [110]. Therefore, the metaphysis and epiphysis do not fuse in mice, but continue to be separated by the growth plate, where cartilage is formed at the epiphyseal side and is replaced by newly mineralized bone on the metaphyseal side. The different regions are visualized in Fig. 3.2A, where mineralized bone at the epiphysis and metaphysis is shown in yellow, separated by the cartilaginous growth plate in blue/green. In order to investigate if the two distinct regions (epiphysis and metaphysis) exhibit different (re)modeling patterns, we segmented the microCT data into two ROIs as shown in Fig. 3.2B, with the epiphysis in light grey and the metaphysis in dark grey. Additionally, we performed the precision analysis for both regions independently and the results are presented in the supplementary in Table B.9 for the metaphysis and Table B.10 for the epiphysis.

The results for cortical bone (re)modeling in cortical bone are depicted in Fig. 3.2C for the metaphysis and in Fig. 3.2D for the epiphysis. The quantitative analysis of the MV/BV over time is shown in Fig. 3.2E and EV/BV in Fig. 3.2F. For the metaphysis, the MV/BV of cortical bone ranges between 30% and 45%, only increasing slightly over time. For the epiphysis, it stays constantly low at around

10%, thus being significantly different at all time points. The same trend can be observed for the EV/BV, with constant values around 20% for the metaphysis and around 5% for the epiphysis, leading to significant differences at all time points. Therefore, cortical bone (re)modeling is greater in the metaphysis compared wit the epiphysis.

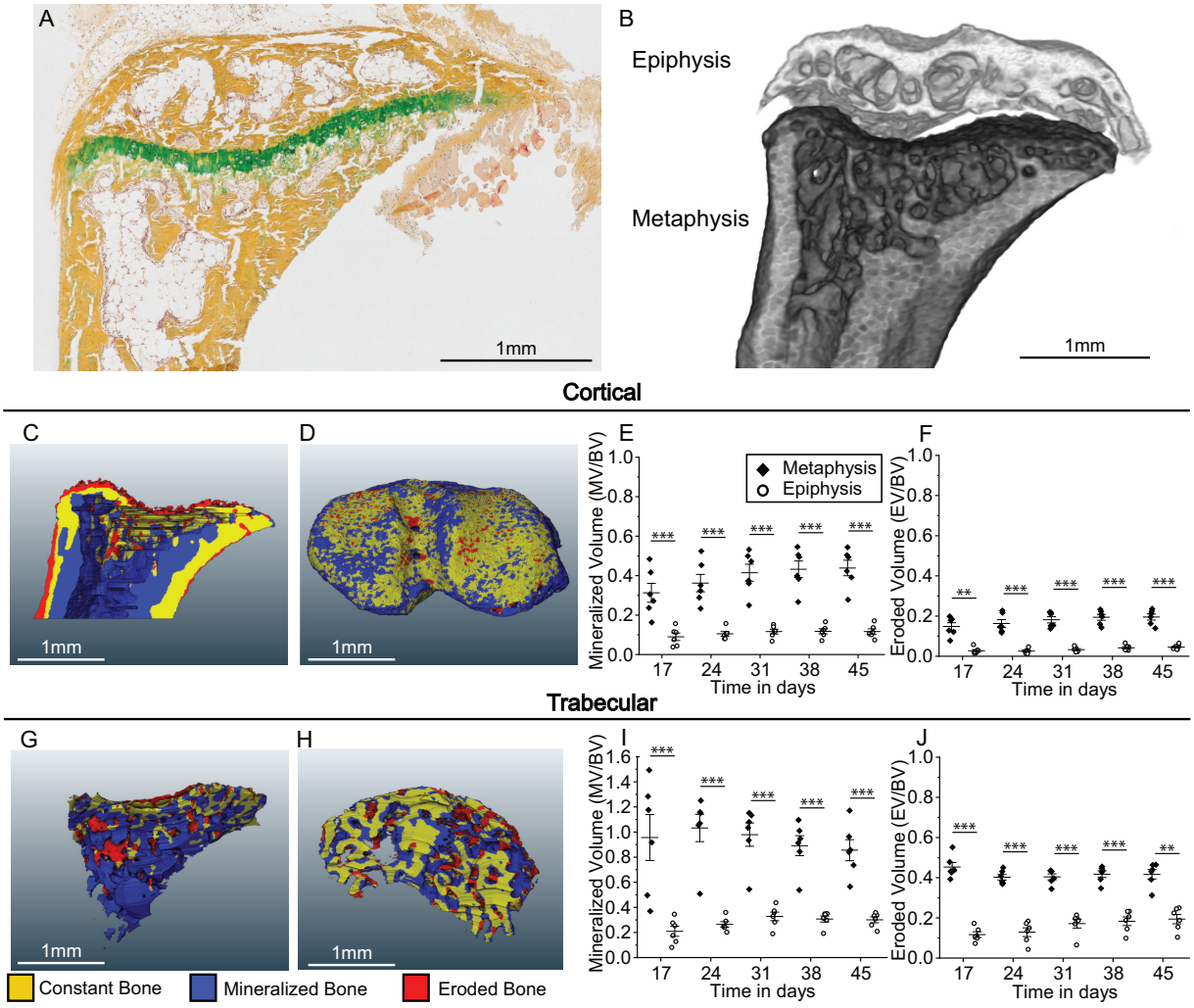

Fig. 3.2: **Segmentation of ROIs according to different (re)modeling behavior in metaphysis and epiphysis in the tibia.** (A) Bone section stained with Movat's Pentachrome showing the growth plate (green/blue) and mineralized tissue (yellow). (B) Segmented microCT data with epiphysis (light grey) and metaphysis (dark grey). Evaluation of cortical bone (re)modeling (with constant bone in yellow, mineralized bone in blue and eroded bone in red, day 31) in the (C) metaphysis and (D) epiphysis. Shown are normalized (E) mineralized and (F) eroded volume over time for metaphysis (diamond) and epiphysis (empty circle). Evaluation of trabecular bone (re)modeling in the (G) metaphysis and (H) epiphysis. Shown are normalized (I) mineralized and (J) eroded volume over time, for metaphysis (diamond) and epiphysis (empty circle). (All plots show mean and standard deviation, with statistically significant values presented as $*$ $p \leq 0.05$, $**$ $p \leq 0.01$ and $***$ $p \leq 0.001$. $N = 6$ bones from six control animals.) [105]

Analogous results are found for trabecular bone, including both primary and secondary spongiosa in the metaphysis as depicted in Fig. 3.2G and for the epiphysis in Fig. 3.2H. The quantitative analysis of the MV/BV is shown in Fig. 3.2I, and EV/BV in Fig. 3.2J. The MV/BV in the metaphysis spans

a large range between 40% and 150%, with a slight decrease over time. This is in accordance with the static microCT analysis (Fig. C.1E), where we see BV increasing between day 0 and day 17, but slightly decreasing between day 17 and day 45. In the epiphysis on the other hand, the values stay constant and at a much smaller range between 10 and 40%, leading to significantly different values between metaphysis and epiphysis at all time points. The EV/BV is similarly higher for the metaphysis, ranging around 45%, compared with the epiphysis (around 15%) with no visible trends over time, thus we find significant differences at all time points between the two regions.

Overall, the segmentation and independent analysis of metaphysis and epiphysis in both cortical and trabecular bone shows, that the two regions with their distinct functions also exhibit different bone (re)modeling patterns, with significantly greater bone (re)modeling in the metaphysis than in the epiphysis over the entire time range. In the following sections, the analysis is focused on metaphyseal bone.

3.1.3 The long bones femur and tibia in the mouse exhibit different bone (re)modeling patterns

In 12-week-old female BALB/c nude mice, the distal femur (Fig. 3.3A) and proximal tibia (Fig. 3.3B) regions in the hind limbs are located in close proximity to one another around the knee and share many physiological features. We compared the bone (re)modeling of segmented metaphyseal bone in the proximal tibia and distal femur, of both cortical and trabecular bone, looking at volume, surface and mineral apposition/resorption rate (MAR/MRR) as shown in Fig. 3.3. Both the newly introduced surface definitions (Fig. 2.2 and 3.1) and the distinct ROIs for cortical and trabecular bone (including primary and secondary spongiosa) (Fig. 3.2) were used.

The cortical bone (re)modeling results are depicted for the femur (Fig. 3.3C) and tibia (Fig. 3.3G) and quantified for mineralized/eroded volume (Fig. 3.3D, H), mineralized/eroded surface on four distinct interfaces (Fig. 3.3E, I) (with soft tissue interfaces in black and constant bone interfaces in yellow) and mineral apposition/resorption rate (Fig. 3.3F, J), showing the femur as diamond and the tibia as empty circle in each plot.

The tibia shows a strong mineralization front in the endocortical region (Fig. 3.3G), which is less pronounced in the femur. This is reflected in the significantly higher MV/BV (Fig. 3.3D) and MAR (Fig. 3.3F) for the tibia at each time point.

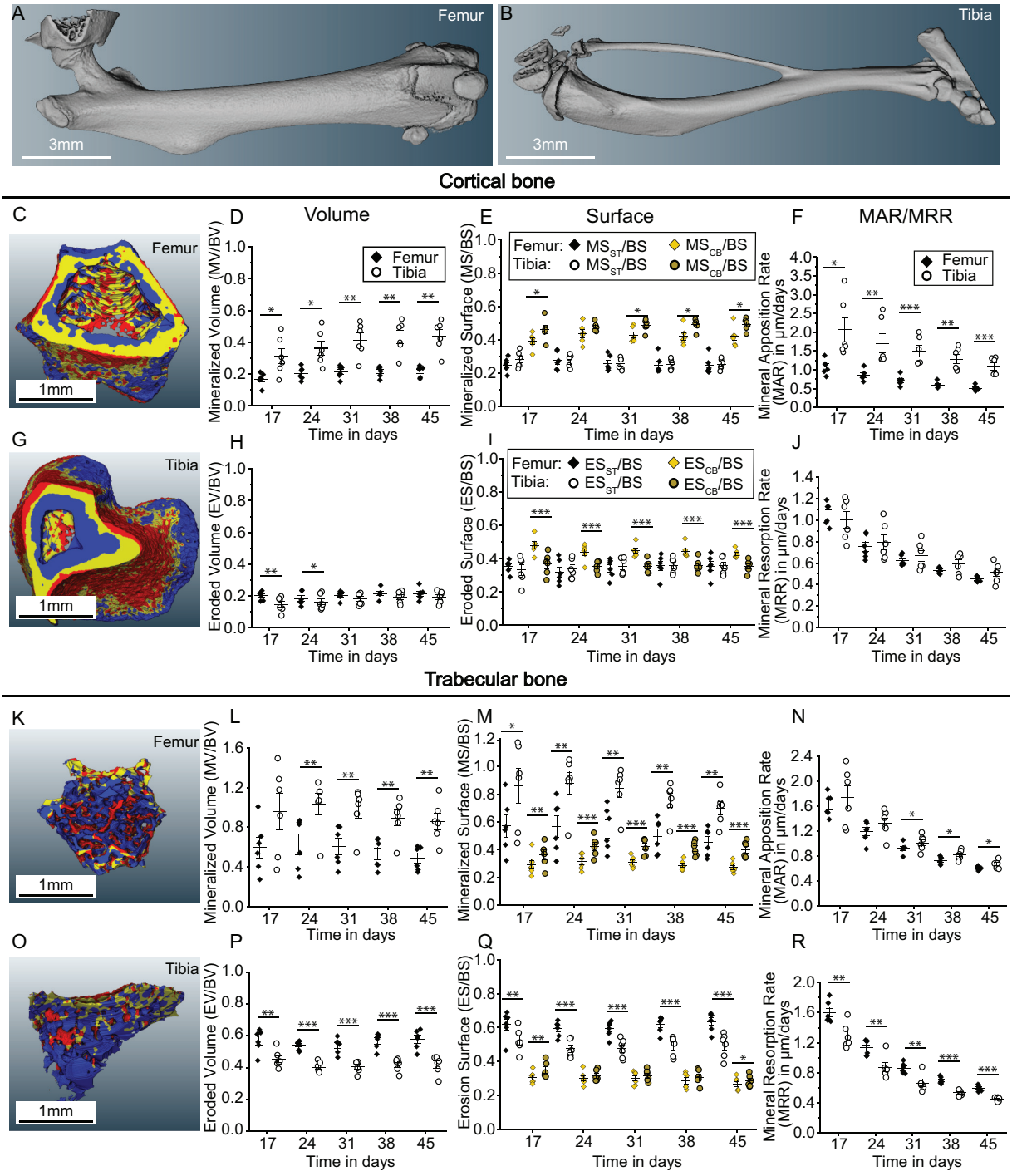

Fig. 3.3: **Different bone (re)modeling patterns on the tibial proximal metaphysis and the femoral distal metaphysis.** 3D rendering of microCT image of mouse (A) femur and (B) tibia. Evaluation of cortical bone (re)modeling in the (C) femur and (G) tibia. Shown are normalized mineralized (D) volume, (E) surfaces (soft tissue interface in black and constant bone interface in yellow, day 31) and (F) MAR over time, as well as normalized eroded (H) volume, (I) surfaces (soft tissue interface in black and constant bone interface in yellow) and (J) MRR over time for femur (diamond) and tibia (empty circle). Evaluation of trabecular bone (re)modeling in the (K) femur and (O) tibia. Shown are normalized mineralized (L) volume, (M) surfaces (soft tissue interface in black and constant bone interface in yellow) and (N) MAR over time, as well as normalized eroded (P) volume, (Q) surfaces (soft tissue interface in black and constant bone interface in yellow) and (R) MRR over time, for femur (diamond) and tibia (empty circle). (All plots show mean and standard deviation, with statistically significant values presented as $*$ $p \leq 0.05$, $**$ $p \leq 0.01$ and $***$ $p \leq 0.001$. N = 6 bones from six control animals.) [105]

A similar trend can be observed for the mineralized surface describing the interface with constant bone (MS_{CB}/BS, Fig. 3.3E), where significant differences can be found at day 17, 31, 38 and 45. This indicates that the constant bone interface is more sensitive to describe cortical bone mineralization.
The eroded cortical bone does not differ strongly in femur and tibia (Fig. 3.3H-J) and both show stable erosion values over time. The only differences can be observed in ES_{CB}/BS, where the femur shows significantly higher erosion values at all time points (Fig. 3.3I). This indicates again that the constant bone interface is more sensitive to describe cortical bone (re)modeling.
The trabecular (re)modeling results are depicted for the femur (Fig. 3.3K) and tibia (Fig. 3.3O) and quantified for mineralized/eroded volume (Fig. 3.3L, P), mineralized/eroded surface on four distinct interfaces (Fig. 3.3M, Q) (with soft tissue interfaces in black and constant bone interfaces in yellow) and mineral apposition/resorption rate (Fig. 3.3N, R), showing the femur as diamond and the tibia as empty circle.
In analogy to cortical bone, trabecular mineralization is significantly higher in the tibia *vs.* femur, for volume and both surfaces at all time points (Fig. 3.3L, M), although for MAR the differences are only significant after day 31 (Fig. 3.3N).
The eroded trabecular bone is higher for the femur for volume, surface and MRR (Fig. 3.3P-R). The ES_{ST}/BS (Fig. 3.3Q) shows significantly more eroded bone for the femur than the tibia, thus making it the more sensitive interface to study trabecular bone (re)modeling. In addition, the MRR is significantly higher for the femur than the tibia at all time points, suggesting localized erosion events in the femur as can be seen in Fig. 3.3K.

Overall a higher mineralization can be observed in the tibia, in both cortical and trabecular (re)modeling. The femur shows higher erosion, mainly in the trabecular bone, compared to the tibia.

3.1.4 Static microcomputed tomography-based bone morphometry analysis as validation for dynamic bone (re)modeling results

Static microCT parameter evaluation of both cortical and trabecular bone was used to further deepen the understanding and validate the results found with dynamic microCT-based time-lapse morphometry. The data for the tibial proximal metaphysis is shown in Fig. C.1. In cortical bone, we see a decrease of TV over time (Fig. C.1A), which is in accordance with the erosion we found on the periosteal site

visible in Fig. 3.2C. In Fig. C.1B we see an increase of BV over time, especially between day 0 and day 17, which strengthens the result we found for the dynamic analysis, with MV/BV starting at around 0.3 (Fig. 3.3E).

The static trabecular bone analysis is shown in Fig. C.1D-F. TV is clearly decreasing (Fig. C.1D), especially between day 0 and 17, which is in accordance with the newly mineralized region on the endocortical bone, reducing the overall marrow volume. BV on the other hand is increasing until day 24 and decreasing afterwards (Fig. C.1E). A similar trend was observed for MV/BV, which shows high values for day 17 and 24, but a decrease towards day 45 (Fig. 3.3L).

Fig. C.2 shows BS/BV for cortical bone in the tibial proximal metaphysis. There is a large decrease between day 0 and day 17, which is expected with the endocortical mineralization visible in Fig. 3.1A. In addition, it confirms the results found in Fig. 3.1B, with lower values for MS_{ST}/BS than for MS_{CB}/BS, as new mineralization at the convex endocortical side, will lead to a decrease in BS/BV and lower values for MS_{ST}/BS than for MS_{CB}/BS.

Analogous analysis for the femoral distal metaphysis is shown in Fig. C.3, including the comparison with the tibial proximal metaphysis. The data for cortical bone is shown in Fig. C.3A-C, with TV staying constant over time for the femur, while there is a slight decrease in the tibia between day 0 and 17. Additionally, BV (Fig. C.3B) is staying constant for the femur over time, while it increases clearly for the tibia. This confirms the trend we find for MV/BV (Fig. 3.3D), with constant values for the femur and increasing values for the tibia. In trabecular bone, there is a decrease of TV for both tibia and femur (Fig. C.3D), with a much stronger trend for the tibia. BV is staying nearly constant for the femur, while we see an increase for the tibia up until day 24, followed by a decrease. These findings are in accordance with the dynamic analysis, showing higher eroded volumes (Fig. 3.3P) and MRR (Fig. 3.3R) for the femur.

In summary, static microCT validates the findings of dynamic time-lapse microCT and reinforces the differences between tibial and femoral bone (re)modeling. Importantly, we can see that only the dynamic analysis gives us detailed information on the different mineralized and eroded regions.

3.1.5 Spatial gradient

After finding that the metaphysis is highly dynamic in comparison to the epiphysis (Fig. 3.2) and that femur and tibia show significantly different (re)modeling behavior (Fig. 3.3), we investigated whether

our model could detect and quantify spatial bone (re)modeling changes in the metaphysis of cortical bone from the tibia and the femur.

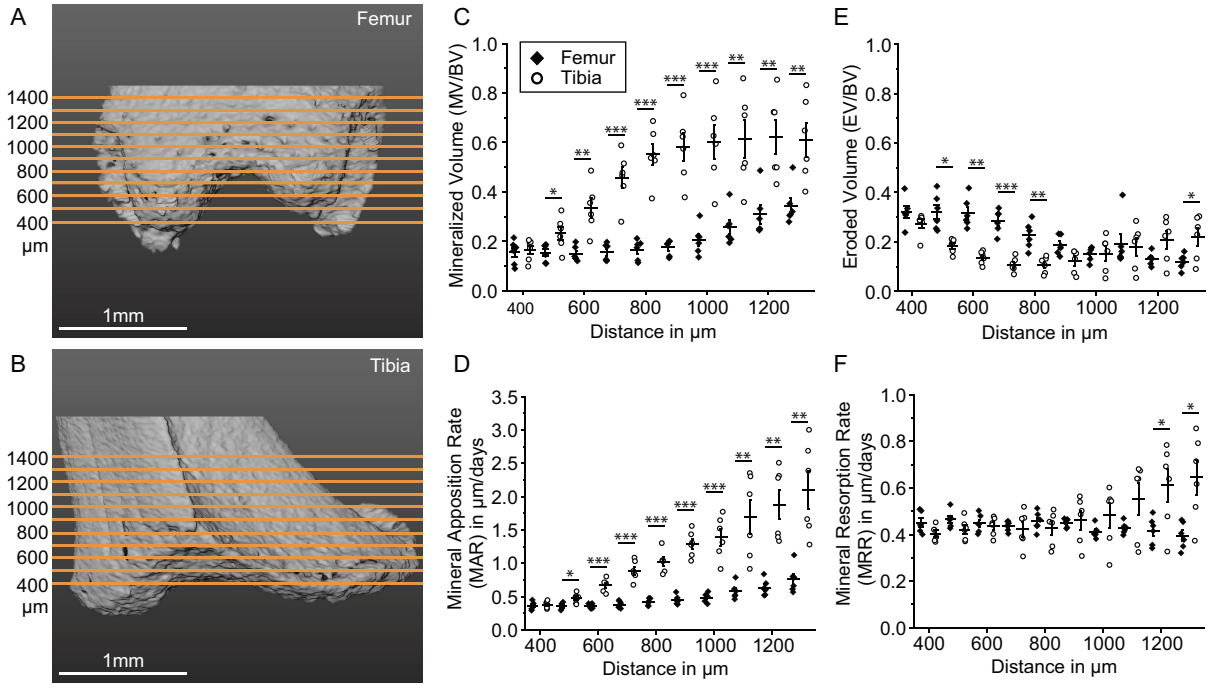

Fig. 3.4: **Spatial evaluation of gradients in bone (re)modeling of femur and tibia reveals significant differences in mineralized regions.** Localization of ten separate 100 µm thick sections in microCT images for (A) the femur and (B) the tibia. Shown are normalized cortical volume of (C) mineralization and (E) erosion as well as (D) MAR and (F) MRR, for femur (diamond) and tibia (empty circle). (All plots show mean and standard deviation, with statistically significant values presented as $*$ $p \leq 0.05$, $**$ $p \leq 0.01$ and $***$ $p \leq 0.001$. N = 6 bones from six control animals.) [105]

The spatial (re)modeling was studied in the respective regions at day 45 (in reference to day 0), by segmenting the microCT datasets into 100 µm thick sections starting 400 µm below the non-mineralized part of the growth plate (on the interface with the primary spongiosa) and reaching towards the diaphysis, as shown in Fig. 3.4A for the femur and Fig. 3.4B for the tibia. The orange lines indicate the respective sections and span nearly the entire ROI of 10% bone length previously analyzed and is shown Fig. 3.4A and B.

MV/BV (Fig. 3.4C) and EV/BV (Fig. 3.4E), as well as MAR (Fig. 3.4D) and MRR (Fig. 3.4F) were analyzed (with the femur shown as diamond and the tibia as empty circle). In both tibia and femur, a gradient of mineralization is visible, showing increasing values in MV/BV (Fig. 3.4C) and MAR (Fig. 3.4D) from the growth plate towards the diaphysis. This gradient is steeper for the tibia and significant differences between tibia and femur are found already 500 µm below the growth plate.

The eroded volume for both femur and tibia on the other hand, shows decreasing values from the

growth plate towards the diaphysis (Fig. 3.4E), with lower values for the tibia. As a consequence, significant differences between femur and tibia can be found in regions from 400 to 900 µm below the growth plate. The MRR does not reflect this difference, showing constant and rather similar values for both femur and tibia and only significantly higher values for the last sections (1,200 – 1,400 µm) of the tibia.

The findings of the spatial analysis are in accordance with the temporal changes that we found. The tibia has a higher mineralization throughout the entire region of the cortical bone, and a lower erosion in some parts of the bone.

In summary, we were able to establish a baseline of physiological bone (re)modeling in both tibia and femur. We have advanced the previously established method of dynamic microCT-based time-lapse morphometry, by introducing two new surface parameters and studied how they are influenced by bone curvature. We further showed significant differences in bone (re)modeling of the tibial epiphysis and metaphysis. Our findings were confirmed with established static microCT parameters and the spatial understanding was further deepened by showing differences in cortical bone (re)modeling in the tibial and femoral sections.

3.2 Changed bone (re)modeling after cancer cell injection

After setting the baseline for physiological bone (re)modeling, we then investigated alterations in bone (re)modeling after cancer cell injection but in the absence of osteolytic lesions.

The bone (re)modeling of animals injected with cancer cells was studied for up to 38 days and compared with healthy animals injected with PBS (n = 7), monitored for up to 45 days. For this analysis, all bones from tumor animals that formed a detectable osteolytic lesions in cortical or trabecular bone of the hind limbs (n = 6/11 mice), were excluded to facilitate comparison between groups. Furthermore, animals not presenting with an osteolytic lesion (n = 5/11) were sacrificed between day 31 and 38 since injection due to humane end point criteria (e.g. significant loss of weight, limping), resulting in a lack of microCT data for day 41 and 45. In Fig. 3.5 the results for both tibial proximal metaphysis and femoral distal metaphysis are shown. The ROIs cover 10% of the total bone length.

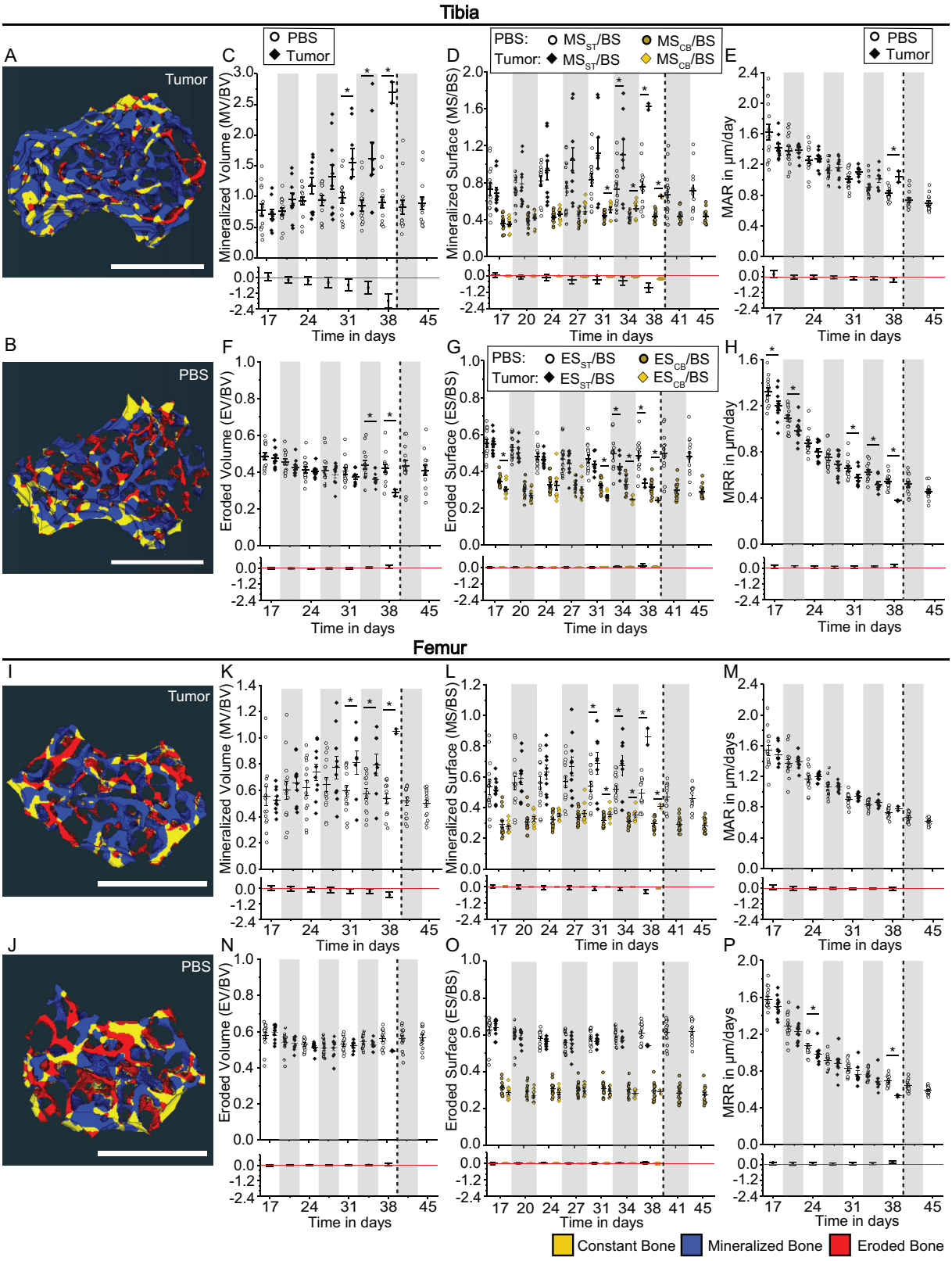
Tibia
A
Tumor
B
PBS
C
PBS
Tumor
Mineralized Volume (MV/BV)
D
PBS: MS_ST/BS MS_CB/BS
Tumor: MS_ST/BS MS_CB/BS
Mineralized Surface (MS/BS)
E
PBS
Tumor
MAR in µm/day
F
Eroded Volume (EV/BV)
G
PBS: ES_ST/BS ES_CB/BS
Tumor: ES_ST/BS ES_CB/BS
Eroded Surface (ES/BS)
H
MRR in µm/day
Time in days
Femur
I
Tumor
J
PBS
K
Mineralized Volume (MV/BV)
L
Mineralized Surface (MS/BS)
M
MAR in µm/days
N
Eroded Volume (EV/BV)
O
Eroded Surface (ES/BS)
P
MRR in µm/days
Time in days
Constant Bone
Mineralized Bone
Eroded Bone

Fig. 3.5

Fig. 3.5: **Bone (re)modeling analysis of animals injected with cancer cells (without detectable osteolytic lesions) in comparison to healthy control animals in trabecular bone.** Results in trabecular bone of tibial proximal metaphysis are depicted for (A) tumor cell injected animals and (B) healthy PBS animals, with newly mineralized bone in blue, eroded bone in red and constant bone in yellow. Results are shown for (C) MV/BV, (D) MS/BS and (E) MAR, as well as (F) EV/BV, (G) ES/BS and (H) MRR with the respective confidence intervals below. Results of bone (re)modeling analysis in trabecular bone of the femoral distal metaphysis depicted for (I) tumor cell injected animals and (J) healthy PBS animals, with newly mineralized bone in blue, eroded bone in red and constant bone in yellow. Results are shown for (K) MV/BV, (L) MS/BS and (M) MAR, as well as (N) EV/BV, (O) ES/BS and (P) MRR with the respective confidence intervals below. (All plots show mean and standard deviation, with statistically significant values presented as $* \; p \leq 0.05$ and confidence intervals shown below. (Scale bars correspond to 1 mm. PBS animals: N = 14 bones from seven animals, Tumor: N = 10 bones from five animals for tibia and femur respectively, data points for tumor animals only go up to day 38, indicated by the dashed line.)

The trabecular bone (re)modeling in the tibia proximal metaphysis is shown for volume, surfaces and apposition/resorption rate in Fig. 3.5A-H, with the depiction for tumor animals in Fig. 3.5A and for healthy PBS animals in Fig. 3.5B. The tumor animal shows mostly newly mineralized bone and clearly less eroded trabeculae, in contrast with the healthy PBS animal, which shows both newly mineralized and eroded trabeculae.

Higher MV/BV is observed for tumor animals at all time points (except for day 17, Fig. 3.5C), with values reaching between up to 1.5 - 2.5 for tumor animals and below 1 for healthy PBS animals. Significant differences with strong confidence intervals clearly below 0 can be seen on day 31, 34 and 38. Similar results are observed for surface (re)modeling in Fig. 3.5D. MS_{CB}/BS shows significantly higher values for tumor animals on day 31, 34 and 38 and MS_{ST}/BS shows significantly higher values only on day 34 and 38. MAR (Fig. 3.5E) shows a significant difference and higher values at day 38.

Differences can also be observed in eroded bone. EV/BV (Fig. 3.5F) shows significantly lower values for tumor animals on day 34 and 38. Interestingly, ES_{CB}/BS (Fig. 3.5G) already shows such significant differences at day 31. The lower erosion in tumor animals without osteolytic lesions can be best observed with the MRR (Fig. 3.5H), showing significantly lower values for day 17, 20, 31, 34 and 38, and with a clear trend for lower values at all time points.

Analogous analysis is performed on the trabecular bone in the femur distal metaphysis (Fig. 3.5). Volume, surfaces and apposition/resorption rate are shown in Fig. 3.5I-P, with the depiction of tumor animals in Fig. 3.5I and healthy PBS animals in Fig. 3.5J. Similar trends as in the tibia are found in the femur, although the femur shows overall less (re)modeling. The tumor animal shows more newly mineralized bone and less eroded trabeculae, in contrast with the healthy PBS animal, which shows both newly mineralized and eroded trabeculae.

Both volume and surface analyses show higher mineralization for animals injected with tumor cells,

with significantly higher values for MV/BV at day 31, 34 and 38 (Fig. 3.5K). The mean values for MV/BV in tumor animals reach up to 0.8, while values for healthy PBS animals stay around 0.6. The surface evaluation shows significantly higher values in both MS_{ST}/BS and MS_{CB}/BS for tumor animals at day 31, 34, and 38 (Fig. 3.5L). The same differences could not be observed in the dynamic analysis shown by MAR (Fig. 3.5M), where mean values for tumor animals seem to be higher at later time points, but without statistical differences.

For eroded bone, no significant differences or changed trends could be observed in both EV/BV (Fig. 3.5N) and ES/BS (Fig. 3.5O). The dynamic data on the other hand shown by MRR (Fig. 3.5P) has significantly lower values for tumor animals on day 24 and 38, and shows an overall trend of lower values for tumor animals for all time points.

The trends described for trabecular bone in both tibia and femur were also observed in cortical bone (Fig. D.1). The changes in (re)modeling were also stronger in the tibia compared to femur. However, most differences were not statistically significant. This highlights the trabecular bone as a more sensitive bone compartment affected by metastasis compared to cortical bone.

Overall, both tibia and femur show a trend towards more newly mineralized bone in tumor animals that were not presenting with osteolytic lesions, while in the tibia, in addition, lower erosion was found.

3.3 Detection and analysis of osteolytic lesions

Next to animals with altered bone (re)modeling in the absence of osteolytic lesions, we also found animals with both cortical and trabecular lesions (n = 6). A new mathematical method was established to detect and quantify osteolytic erosion patch volume over time in cortical bone of both femur and tibia, clearly differentiating between physiological bone erosion and pathological erosion patches. In addition, we visually inspected all bones for osteolytic lesions in the trabecular bone and found a reoccurring trend for lesions in the primary spongiosa right at the onset of the mineralized growth plate.

3.3.1 Eroded bone patch analysis of osteolytic lesions in cortical bone

Osteolytic erosion patches were found in the cortical bone of six animals, with three in the tibia and three in the femur. Some lesions were first visually detected by inspecting the microCT data, which

was a sacrifice criteria for the animals. The eroded bone patch method was develop afterwards with the help of the visually detected lesions. It confirmed the findings and additional lesions were detected. As a result, for some animals only one time point is available, as the lesion was visually detected and the animal sacrificed. Animal 1 was part of the pilot group, where the overall animal model was still established, and the lesions were visually tracked until the animal had to be sacrificed due to humane end point criteria.

Five of these lesions started in the periosteum and one in the endocortical region and the results are shown in Fig. 3.6. Lesions in the tibia are shown for animal 6 for up to 27 days (Fig. 3.6A and A.1) and animal 1 for day 17 (Fig. 3.6B and B.1). Lesions in the femur are shown for animal 2 (showing an endocortical lesion) for day 17 (Fig. 3.6C and C.1) and for animal 4 for day 17 and 20 (Fig. 3.6D and D.1).

For each animal both bone (re)modeling analysis images with constant bone in yellow, mineralized bone in blue, eroded bone in red, eroded bone patches in green and eroded bone patch cores in pink are shown with the respective original gray scale image. Enlargements for the (re)modeling visualization at day 17 are shown in Fig. 3.6A.1, B.1, C.1 and D.1. The quantification of the cluster size is shown in Fig. 3.6E.

All lesions were detected on day 17, which is the first time point that was measured after the reference scan. The patch size at first detection varies between 0.005 – 0.025 mm^3, with equal distribution of smaller and bigger lesions in both femur and tibia. Lesions were tracked for up to 27 days (animals had to be sacrificed due to humane endpoint criteria) and in several animals the increase in osteolytic eroded bone patch volume was followed, with animal 1 starting at 0.001 mm^3 and reaching a final lesion size of nearly 0.1 mm^3 (Fig. 3.6E).

In addition to the quantification, the eroded bone patch analysis enables the spatial and temporal visualization of osteolytic lesions, which improves the understanding related to the onset of the lesion, where and when they start. Animal 6 (Fig. 3.6A and A.1) shows an increasingly big erosion patch (as quantitatively proven in Fig. 3.6E), spanning the entire cortical bone already at day 17, with several voxels included in the initial eroded bone patch core (Fig. 3.6A.1). The patch seems to start from the periosteal region, where the osteolytic lesion is broader (as compared to the endocortical region).

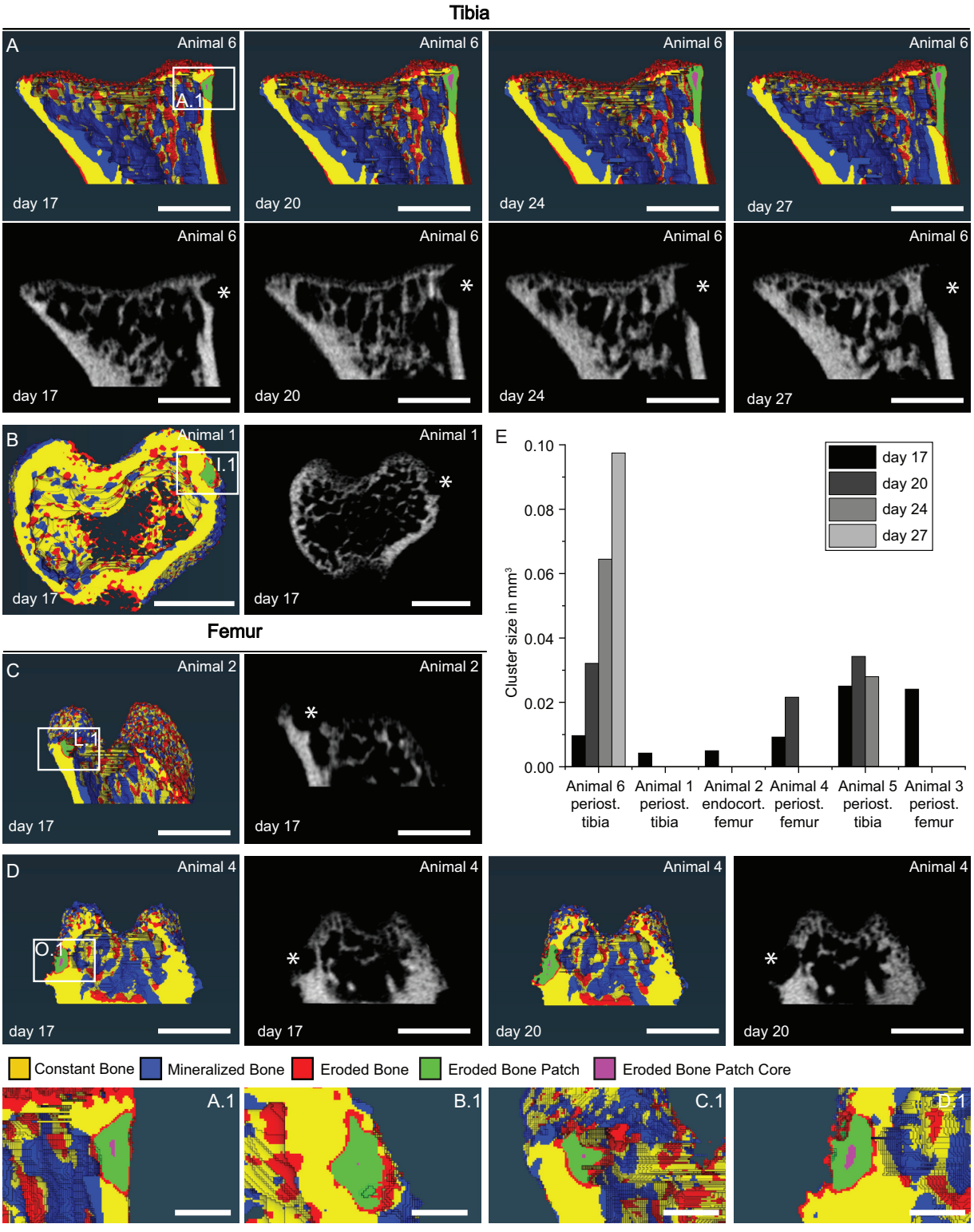
Tibia
A
Animal 6
A.1
day 17
day 20
day 24
day 27
B
Animal 1
I.1
Femur
C
Animal 2
L.1
D
Animal 4
O.1
E
Cluster size in mm³
0.10
0.08
0.06
0.04
0.02
0.00
day 17
day 20
day 24
day 27
Animal 6 periost. tibia
Animal 1 periost. tibia
Animal 2 endocort. femur
Animal 4 periost. femur
Animal 5 periost. tibia
Animal 3 periost. femur
Constant Bone
Mineralized Bone
Eroded Bone
Eroded Bone Patch
Eroded Bone Patch Core
A.1
B.1
C.1
D.1

Fig. 3.6

Fig. 3.6: **Newly established tool of erosion-patch analysis allows detection and quantification of osteolytic lesions in cortical bone.** Results of bone (re)modeling and detection of erosion-patches with constant bone in yellow, mineralized bone in blue, eroded bone in red, eroded bone patches in green and eroded bone patch core in pink are visualized for the tibia of (A) animal 1 at day 17 (with an enlargement in (A.1)), day 20, day 24 and day 27, with respective gray scale images shown below. (Re)modeling analysis visualization for the tibia of (B) animal 2 at day 17 (with an enlargement in (B.1)) with the respective gray scale image. (Re)modeling analysis visualization for the femur of (C) animal 3 at day 17 (with an enlargement in (C.1)) with the respective gray scale and for the femur of (D) animal 4 with (re)modeling analysis visualization for day 17 (with an enlargement in D.1) and day 20, with the respective gray scale images. (E) Quantitative results of the eroded bone patch analysis per animal up to 27 days. (Scale bars correspond to 1 mm, with 0.2 mm for enlargements and the lesions are indicated with an asterisk in the gray scale images. N = 6 bones from six tumor animals.)

Animal 1 shows a tibial lesions that seems to not have fully crossed the entire cortical thickness, or only at very few points (Fig. 3.6B.1). The femoral lesion in animal 2 on the other hand, is clearly starting at the endocortical site and not yet spanning the full cortical thickness (Fig. 3.6C.1).
This new eroded bone patch analysis tool allows us to identify and track erosion-patches in the cortical bone caused by metastatic osteolytic lesions, as early as day 17. Even the smallest patches with a size around 0.05 mm^3, which are not yet spanning the entire cortical thickness, can be identified and quantified. In addition, we made sure the tool only detects eroded bone patches stemming from pathological bone (re)modeling. We tested the tool with the help of healthy control mice and found no detected eroded bone patches at all time points (up to 45 days).

In summary the tool confirmed the lesions detected by first visual inspection of microCT data and, in addition, helped us to discover additional two lesions in tibia and femur.

3.3.2 Osteolytic lesions in trabecular bone

Osteolytic lesions in the trabecular bone were found in two animals, with three lesions presenting in the tibia and one in the femur. All lesions were detected at day 17, which is two weeks after cancer cell injection and the earliest measurement time point. Lesions in the tibia are shown in Fig. 3.7A-C and the femoral lesion is shown in Fig. 3.7D. For all animals bone (re)modeling analysis visualization of the top view and an enlargement of a cross-section is shown, together with the gray scale images. The top view shows, that the growth plate is highly (re)modeled in both tibia and femur. Here, the osteolytic lesion presents as a dense erosion patch. In the respective gray scale image a hole in the same area can be found, which is larger than physiological pores in the growth plate. The enlargements (Fig. 3.7A.1, B.1, C.1, D.1) confirm that the growth plate is eroded in a larger area, spanning both along the growth plate and towards the secondary spongiosa.

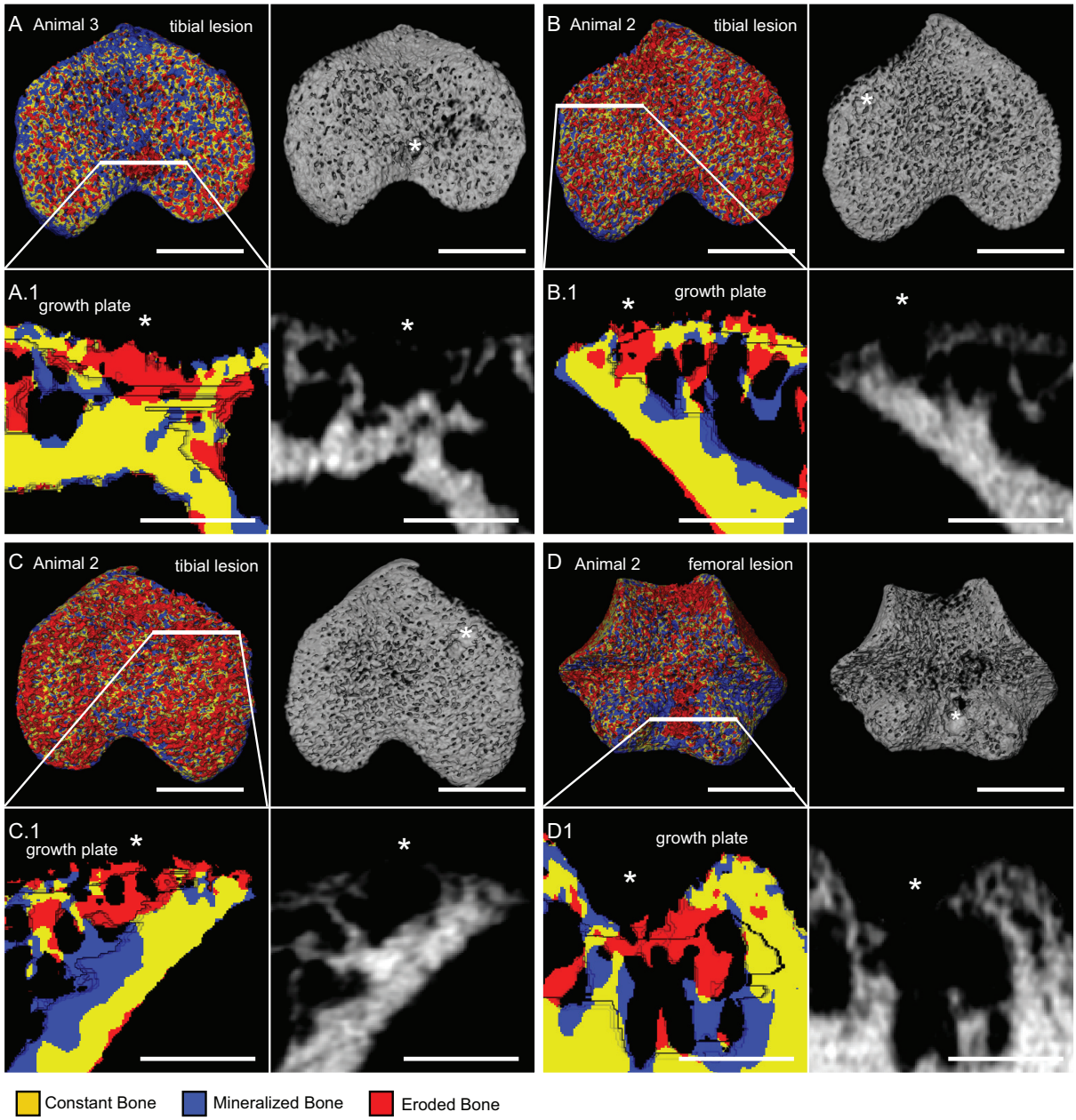

Fig. 3.7: **Trabecular lesions in the primary spongiosa in femur and tibia.** Results of bone (re)modeling with constant bone in yellow, mineralized bone in blue, eroded bone in red, as well as gray scale images for bones at day 17. (A)(Re)modeling visualization top view, with respective gray scale image and (A.1) enlargement of the cross-sections for the tibia of animal 1. (B)(Re)modeling visualization top view, with respective gray scale image and (B.1) enlargement of the cross-sections for the left tibia of animal 2. (C)(Re)modeling visualization top view, with respective gray scale image and (C.1) enlargement of the cross-sections for the right tibia of animal 2. (D)(Re)modeling visualization top view, with respective gray scale image and (D.1) enlargement of the cross-sections for the femur of animal 2. (Scale bars correspond to 1 mm and 0.5 mm for enlargements. The lesions are indicated with an asterisk. N = 4 bones from two tumor animals.)

Although all lesions are still at a very early stage, Fig. 3.7B.1 clearly shows the smallest lesion with a length of under 200 µm. Different locations of the trabecular erosions are observed, with two lesions at the lateral and medial site towards the anterior end (Fig. 3.7B and C). Two samples show a rather

large and dense erosion between the condyles (Fig. 3.7A and D). In addition, in a previous study with a pilot animal (Fig. E.1) [105], we showed that such lesions can erode nearly the entire trabecular bone within three weeks past injection.

Overall, we were able to identify three different types of lesions based on the bone compartment that they had started to erode (cortical vs. trabecular) and their location within these.

- There are fully cortical lesions as were shown in Fig. 3.6, that start on the periosteal side and do not attack the trabecular bone even in a growth period of 10 days (Fig. 3.6A).
- There are mixed lesions as shown in Fig. 3.6C, where both the endosteal cortical bone and the closely located trabecular bone are being resorbed. The progression of such a lesion was shown in our previously published work for one pilot animal (Fig. E.1) [105].
- Lastly there are trabecular lesions located directly at the mineralized growth plate, that do not involve the erosion of cortical bone in the early detection stages as shown in Fig. 3.7.

We have here presented a powerful tool to detect and study all types of lesions at an early stage of bone metastasis.

After successfully studying pathological bone (re)modeling *in vivo*, as well as developing a tool to detect and characterize osteolytic lesions, we then investigated the cancer cells in their bone microenvironment with multiscale and multimodal imaging tool.
In the second part of the results, the following *ex vivo* work is structured in the detection of cancer cells in the bone marrow, further studies on the proliferation of cancer cells and the structural microenvironment in the bone marrow and lastly a characterization of early osteolytic lesions.

3.4 Detection and analysis of cancer cells in the 3D (intact) bone

The infiltration of fluorescently labeled eGFP+ cancer cells was studied in 3D (intact) tibiae, with and without detectable osteolytic lesions. The bones were optically cleared and measured with a light sheet confocal microscope. To confirm the results, corresponding sections from the contralateral bone of each animal were imaged with CLSM with DAPI counter staining.

3.4.1 3D visualization and spatial mapping of cancer cells in intact bones using light-sheet fluorescence microscopy

LSFM was used to study cancer cells and small cell clusters in 3D (intact) tibiae. Optical clearing makes the bone transparent to the LSFM and allows 3D visualization of eGFP+ cancer cells in the bone marrow and in the periosteum. The results are shown in Fig. 3.8, with 2D (virtual) sections of the 3D (intact) bone shown in Fig. 3.8A (enlargements in A.1 - A.4) and a corresponding microCT image in Fig. 3.8B. Quantitative data showing the localization of the cancer cell clusters and their size is shown in Fig. 3.8C-E, including a colored depiction of the localization in Fig. 3.8F, where the color scale indicates the shortest distance to the cortical bone surface.
From the 6/11 tumor animals where an osteolytic lesion was detected, cancer cells were confirmed using LSFM in one of the four limbs in five of these animals. One animal was excluded in the analysis using LSFM, because the lesion was already large and caused severe alterations in the bone . In the 5/11 tumor animals where no osteolytic lesion in the lower limbs was detected, cancer cells were only confirmed in the tibia of one animal with LSFM. For the following analysis, five tibiae from five different animals were analyzed (Fig. 2.4):

- Two tibiae from animals with trabecular lesions in the same bone
- One tibia from an animal with a cortical lesion in the same bone

- One tibia from an animal with a cortical lesion in the respective femur
- One tibia from an animal without any detected osteolytic lesion

In total around 5,500 cells in the bone marrow of all bones were analyzed. As clearly visible in the (virtual) 2D section overview image in Fig. 3.8A, cancer cells and cell clusters have infiltrated the entire bone marrow of the tibia, originating from an animal with a trabecular osteolytic lesion in this tibia. In the metaphysis and upper diaphysis, most cancer cells are found on the anterior side of the tibia (Fig. 3.8A.1). In the lower diaphysis, cells are found more evenly distributed in the entire bone marrow (Fig. 3.8A.2). In addition to cells and small cell clusters distributed all over the bone marrow, larger and more dense clusters of cancer cells were found in the periosteal region, as shown in Fig. 3.8A.3, depicting a dense cluster of cells sitting on the periosteum of the tibial epiphysis close to the fibula. Finally, single cells and small clusters of only a few cells were found in between muscle fibers and all over the periosteal bone surface (Fig. 3.8A.4). Analogous analysis of five bones showed, that cancer cells could be detected in different bone compartments like the diaphysis, metaphysis and epiphysis, as well as in different types of bone such as tibia and fibula, as shown in Fig. 3.9.

The location of all cancer cells in the bone marrow of n = 5 bones was determined in relation to the shortest distance to the cortical bone surface. The results in Fig. 3.8C show that most tumor cells are in close proximity to the cortical bone surface with a mean distance of around 50 µm. Only animal 3 is an exception with a mean distance of around 80 µm. The distribution of cells in the bone marrow is also depicted in Fig. 3.8F, with cells closer to the cortical bone surface shown in yellow and cells furthest away shown in purple and blue. Only very few purple cells are visible, graphically depicting the quantitative analysis.

In addition, the size of cells and cell clusters in the bone marrow (Fig. 3.8D) and in the periosteal site (Fig. 3.8E) was determined. In the bone marrow, around 5,500 cells in n = 5 bones were analyzed, with around 600 cells mm^{-3}, except one bone with a density of 500 cells mm^{-3}. The largest cell clusters ranged up to 60 – 70 µm diameter, the smallest cells and clusters were under 10 µm diameter and the mean diameter was between 31 – 36 µm, indicating that most cells appear as small clusters. At the periosteal site around 2,800 cells were analyzed in larger dense clusters (Fig. 3.8E and Fig. 3.9E-H). The size of the cells in these clusters was found to be smaller than in the bone marrow with mean diameters around 20 µm (Fig. 3.8E).

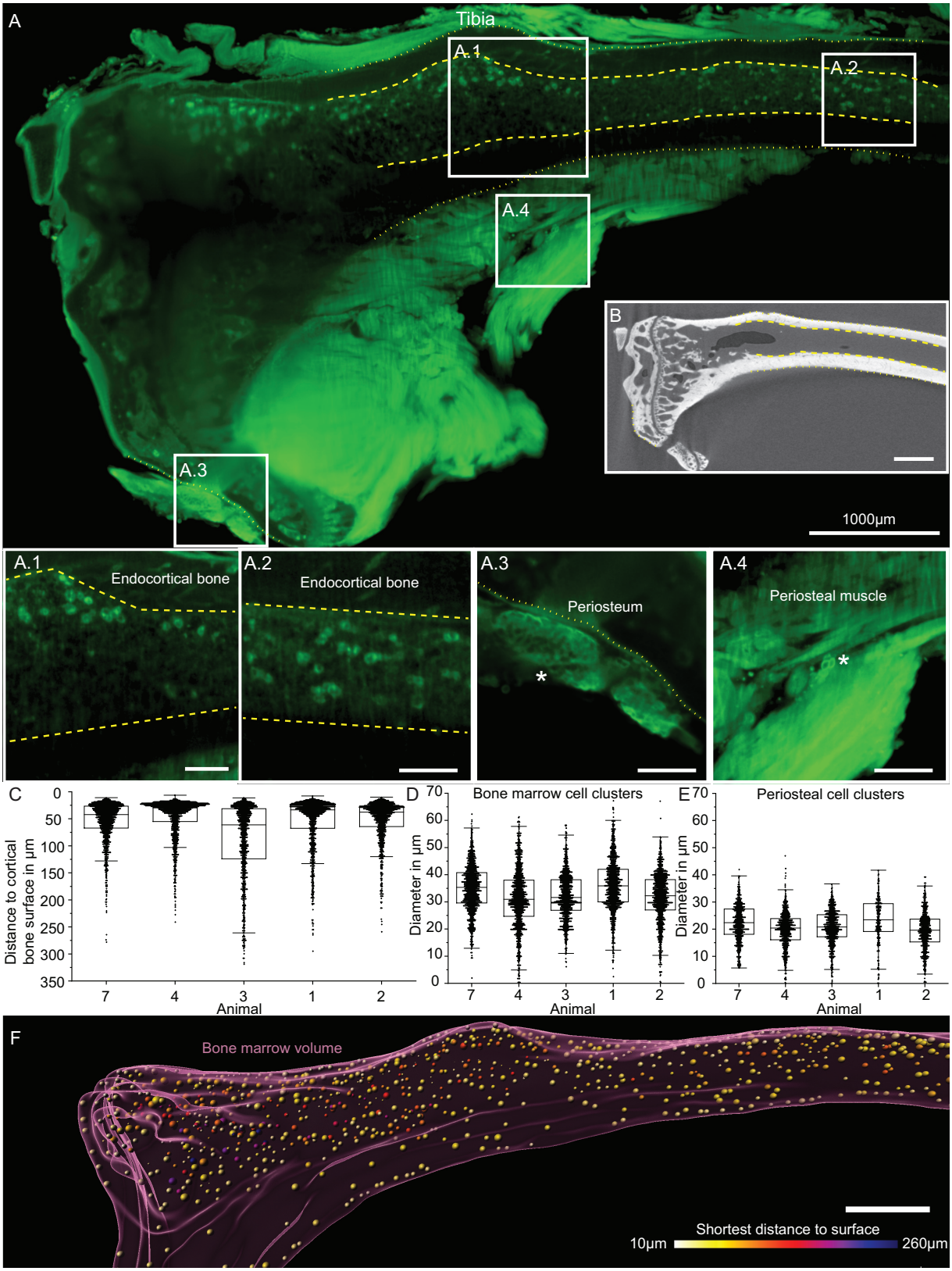
A
Tibia
A.1
A.2
A.4
A.3
B
1000µm
A.1
Endocortical bone
A.2
Endocortical bone
A.3
Periosteum
A.4
Periosteal muscle
C
Distance to cortical bone surface in µm
Animal
D
Bone marrow cell clusters
Diameter in µm
Animal
E
Periosteal cell clusters
Diameter in µm
Animal
F
Bone marrow volume
Shortest distance to surface
10µm
260µm

Fig. 3.8

Fig. 3.8: **Cancer cells were detected and quantified in five intact tibiae of tumor animals using LSFM.** LSFM images of one (virtual) section are depicted for (A) one entire bone, with enlargements of small cell clusters in the bone marrow on the (A.1) upper diaphysis with highlighted endocortical bone surface, (A.2) lower diaphysis with highlighted endocortical bone surface, (A.3) periosteal site as large dense cluster (marked with an asterisk) and (A.4) in between muscle tissue as small clusters (marked with an asterisk). (B) MicroCT image of the same bone as shown in A, with highlighted endocortical and periosteal bone surfaces. Quantification is shown in (C) with the distance of the cancer cells to the cortical bone surface, the size of cancer cells and clusters (D) in the bone marrow and (E) in larger periosteal clusters. (F) Graphical visualization of the distance of cancer cells in the bone marrow to the cortical bone with a color code indicating the distance. (Asterisks indicate the presence of cancer cells and scale bars correspond to 500 µm and 200 µm respectively. N = 5 bones from five tumor animals, representative images from animal 2.)

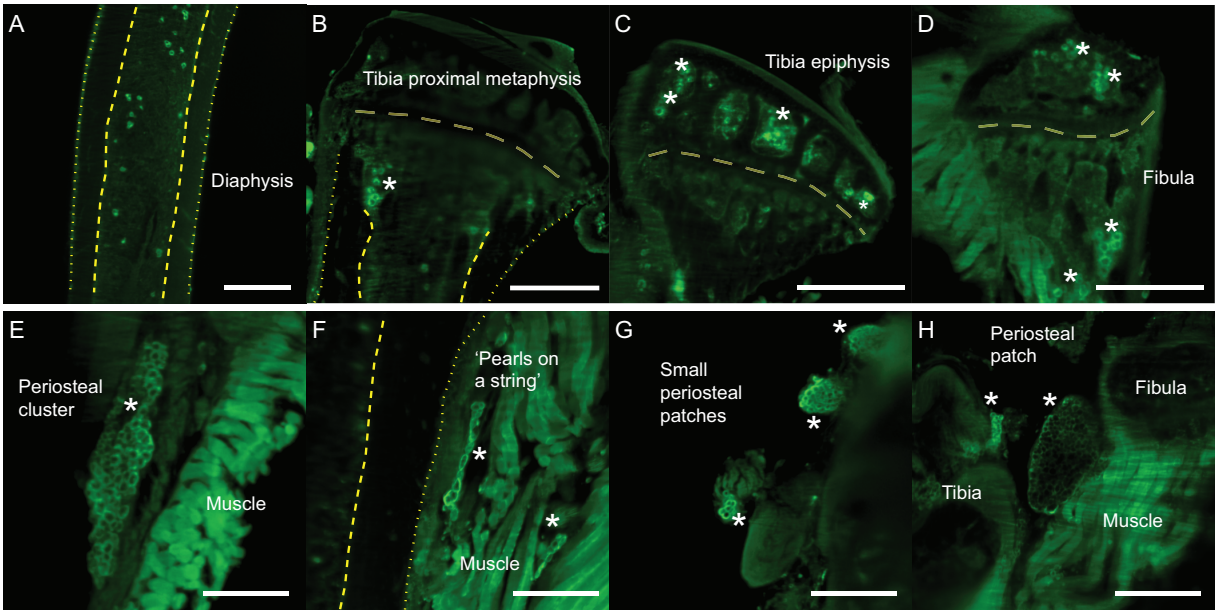

Fig. 3.9: **Visualization of cancer cells in and on the bone using LSFM.** Images showing cancer cells in the (A) tibial diaphysis, (B) tibial proximal metaphysis, (C) tibial epiphysis and (D) fibula, as well as in the periosteal are as (E) a large patch, (F) like 'pearls on a string', (G) as a small patch and (H) as a large patch between tibia and fibula. (Scale bars correspond to 500 µm (A-D) and 250 µm (E-F), cancer cells and patches are marked with an asterisk, while periosteal and endocortical bone, as well as the growth plate are marked with yellow lines. N = 5 bones from five animals.)

In summary we were able to both localize and quantify over 8,000 cells and cancer cell clusters in the bone marrow and periosteal region of n = 5 intact bones, giving completely new insights on the homing of cancer cells at the secondary organ bone.

3.4.2 Validation of detection of cancer cells in frozen bone sections using confocal laser scanning microscopy

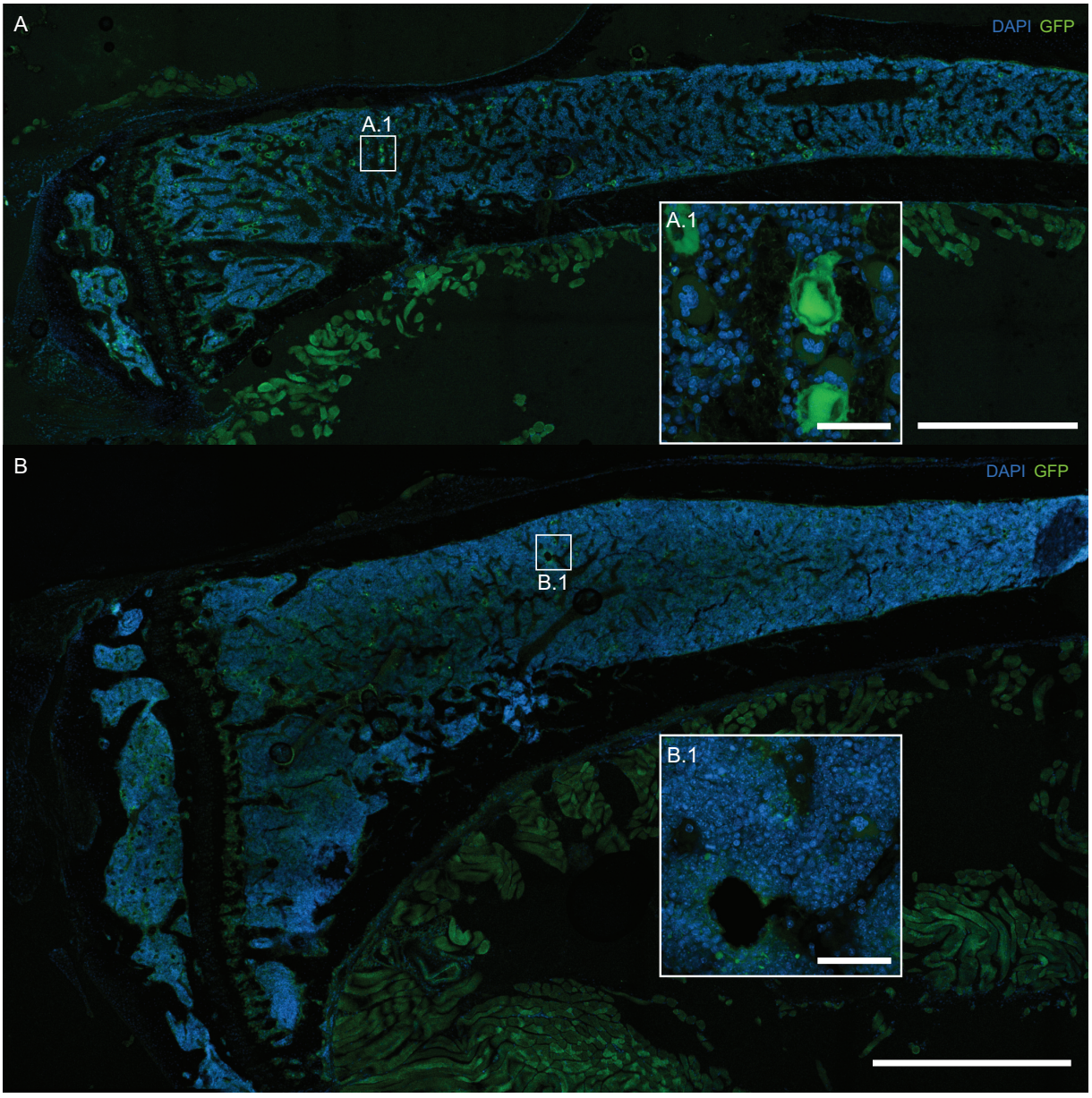

Fig. 3.10: **Detection of eGFP labeled cancer cells in bone cryo-sections using CLSM.** (A) Tumor animal with enlargement in (A.1) and (B) PBS control animal with enlargement in (B.1). (Scale bars correspond to 1 mm for overview and 50 µm for enlargements. DAPI staining of the nucleus in blue, eGFP of the cancer cells in green. N = 6 bones from six tumor animals, representative images from animal 1 for A.)

In order to confirm the results of the LSFM analysis and to gain further insights about the homing of the cancer cells, histological cryo-sections of the contralateral tibia of each animal were analyzed with CLSM.

The results in Fig. 3.10 show a tumor animal with eGFP+ cancer cell invasion in the bone marrow

(Fig. 3.10A with an enlargement in Fig. 3.10A.1) and a healthy PBS animal sacrificed after 17 days as a control (Fig. 3.10B with an enlargement in B.1). The tumor animal shows many large strongly fluorescent cancer cell clusters in the bone marrow, both in the metaphysis and the epiphysis. In the PBS animal on the other hand, only some auto-fluorescent spots can be observed, but no larger clusters of fluorescence are found.

3.5 Status of cancer cell clusters in bone marrow and characterization of the surrounding extracellular matrix

With the help of LSFM we were able to detect, quantify and localize cancer cells in the bone marrow in 3D. To verify our findings, we used CLSM on sections from contralateral tibiae that were additionally stained with DAPI and we detected the eGFP+ breast cancer cells. In order to investigate the proliferation status of the cancer cells and characterize their structural microenvironment, in particular FN fiber density in the ECM, further IF staining of sections was performed.

3.5.1 Proliferation activity

The proliferation state of the cancer cells and cell clusters in the bone marrow was analyzed using the proliferation marker Ki67. This protein is present during all active phases of the cell cycle and only absent in resting cells. Sections from four bones harvested from four tumor animals, that had presented with osteolytic lesions in one of the other long bones and one bone having a trabecular lesion (Fig. 2.4), were imaged. In total 388 cells were detected in the bone marrow and analyzed for the proliferation status. Results are shown in Fig. 3.11A (with enlargements in A.1, A.2 and A.3) and quantification in Fig. 3.11B.

For all bones a distinct area with a large number of cancer cells was analyzed which was either the metaphyseal or upper diaphyseal region. Three different states were defined: 1) Ki67 negative cancer cells clusters (Fig. 3.11A), 2) Ki67 positive cancer cell clusters (Fig. 3.11A.2) and 3) cancer cell clusters with a Ki67 signal on the edge, that could stem from either the cluster or other closely located cells (Fig. 3.11A.3). High resolution examples of the single signals for Ki67 negative (Fig. F.1A-D) and Ki67 positive (Fig. F.1E-F) cancer cell clusters can be found in the supplementary materials.

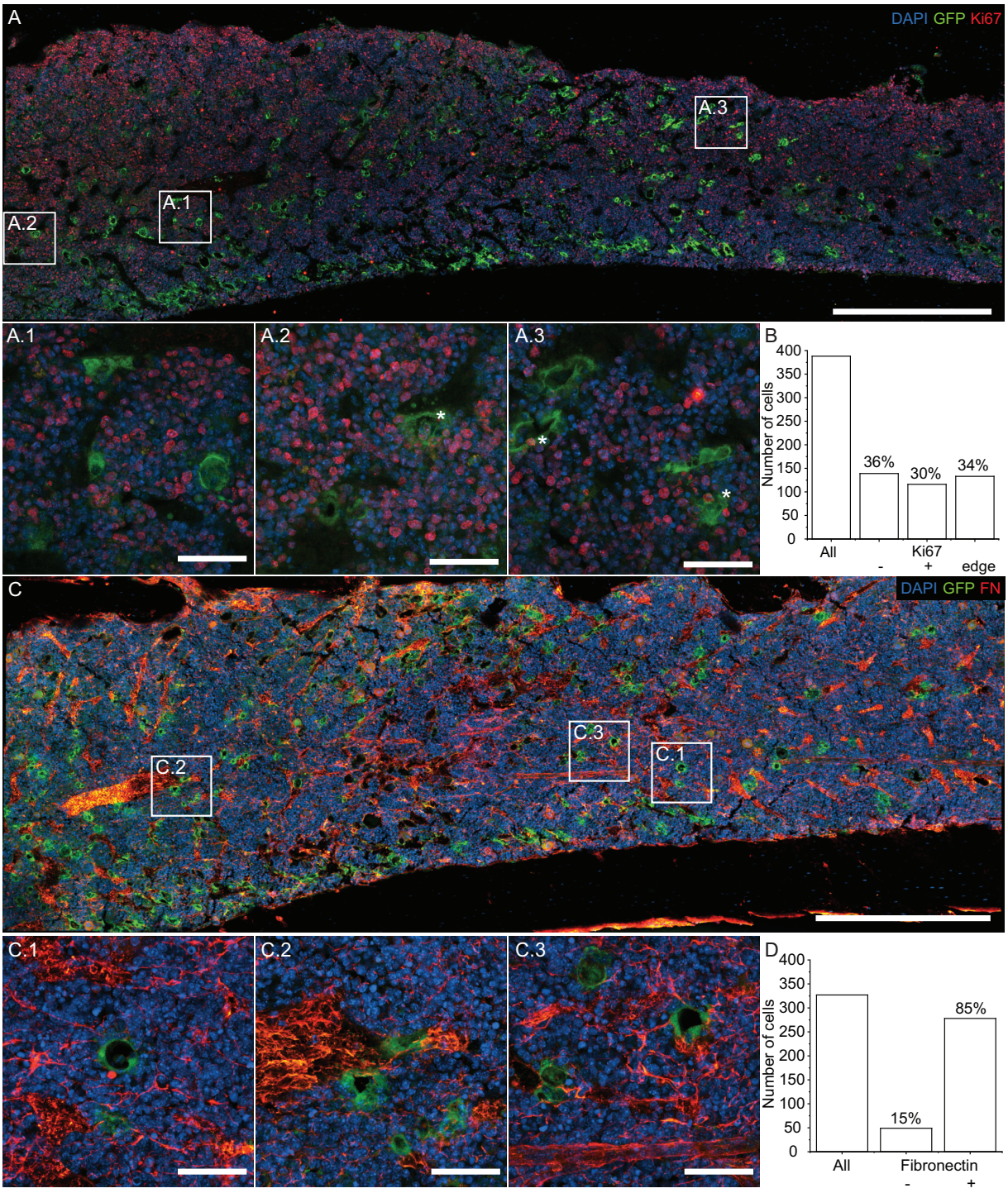

Fig. 3.11: **Proliferation activity and FN network analysis surrounding breast cancer cells in the bone marrow.** Results of CLSM shown for (A) Ki67 proliferation marker with enlargement (A.1) showing Ki67 negative cell clusters, (A.2) showing Ki67 positive cell clusters and (A.3) showing cell clusters that have a Ki67 signal on the edge of the cluster that can not be clearly associated (Ki67 edge). (B) Quantification of the Ki67 signal for all n = 388 analyzed cells. Results of CLSM shown for (C) FN with enlargement (C.1) showing cancer cell clusters not in contact with FN, (C.2) and (C.3) showing cancer cell clusters in close contact with FN. (D) Quantification of the FN network distribution in the proximity of breast cancer cells of n = 327 analyzed cells. (Scale bars correspond to 500 µm and 50 µm for the enlargements. DAPI staining of the nucleus in blue, eGFP of the cancer cells in green and Ki67 (A) and FN (C) in red respectively. N = 4 bones from four tumor animals with osteolytic lesions in other long bones, representative images from animal 3.)

Out of 388 analyzed cells, 139 were found to be Ki67 negative, while 116 were clearly Ki67 positive and 133 had a signal from the edge (Fig. 3.11B). Therefore, a third of the cancer cell clusters in the bone marrow can be claimed as non proliferative.

3.5.2 Fibronectin network analysis

As FN is one of the key proteins of the ECM and has been shown to be associated with cancer outgrowth, we studied the FN distribution in the proximity of breast cancer cells in the bone marrow (Fig. 3.11C, with enlargements in Fig. 3.11C.1, C.2 and C.3) and quantification in Fig. 3.11D. Overall, the FN density in the bone marrow is heterogeneous with some higher and lower density areas (Fig. 3.11C). The location of the cancer cell clusters with respect to FN was investigated and two separate categories identified: 1) not surrounded by FN or only by few single fibers (Fig. 3.11C.1), 2) in close contact with FN network (Fig. 3.11C.2 and C.3). Out of 327 analyzed cells (Fig. 3.11D), only 49 were not surrounded by a dense FN network (which corresponds to roughly 15%) and those were mainly located in the diaphysis. 85% of the cells (278) were in close contact with a dense FN network. Therefore, it is clear that cancer cell clusters seem to favor a FN rich microenvironment.

3.6 Early metastatic osteolytic lesions and alterations on the structural and biophysical bone microenvironment

Lastly, we aimed to characterize the structural and biophysical microenvironment of early metastatic osteolytic lesions, using multiscale and multimodal imaging tools. Bone osteolytic lesions in femur (Fig. 3.12) and tibia (Fig. G.1) were analyzed and compared with intact regions within the same bone. Different tools were used to study the compartments of the ECM. With the help of BSE microscopy, the mineralized tissue is visualized. CLSM of rhodamine-stained tissue enables us to see the lacunae and canaliculi network, while SHG imaging allows the detection of collagen fibers. Finally staining of a section with H&E, gives an overview of the different tissue types, including mineralized tissue, soft tissue and cells.

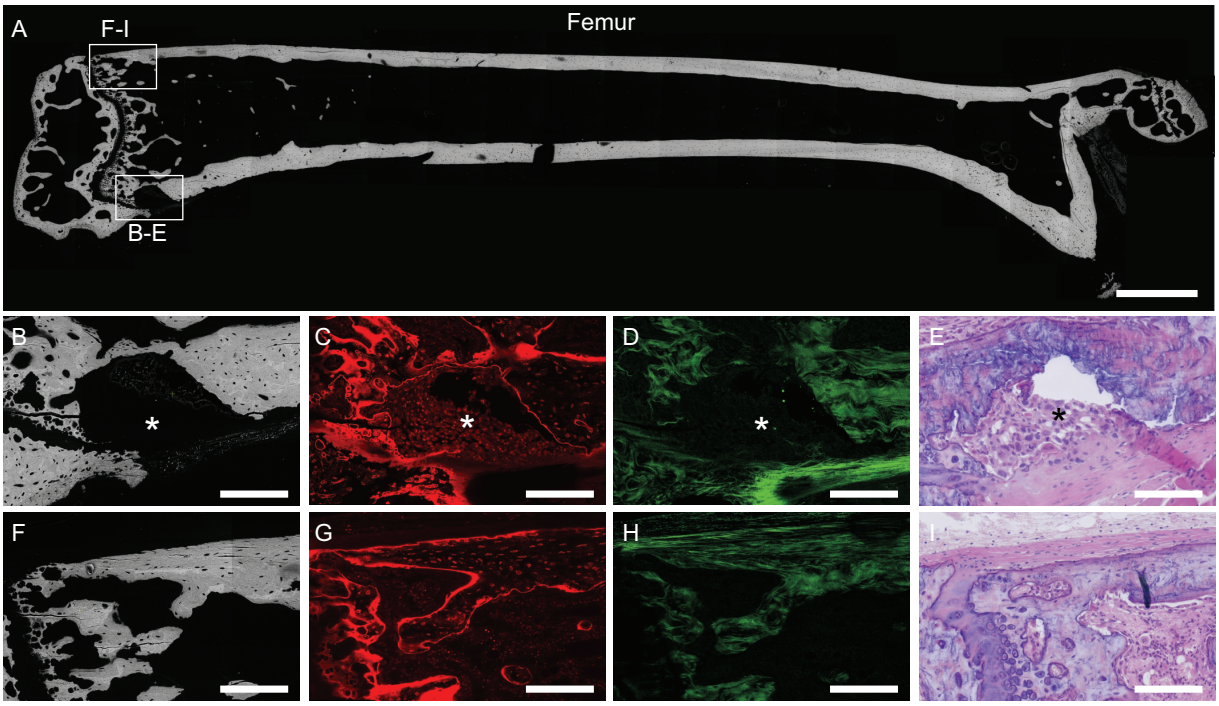

***Fig. 3.12: Ex vivo* characterization of an early metastatic lesion in cortical bone and comparison with intact bone tissue in the same sample.** (A) Overview BSE microscopy image of a femur with (B) enlargement of a cortical lesion, as well as (C) CLSM of rhodamine-stained tissue, (D) SHG imaging of collagen fibers and (E) H&E stain. (F) BSE microscopy enlargement of an intact bone region, as well as (G) CLSM of rhodamine-staining tissue, (H) SHG imaging of collagen fibers and (I) H&E stain. (Asterisks indicates the presence of a lesion, scale bars correspond to 1 mm and 200 µm in the enlargements. N = 5 bones from five tumor animals containing an osteolytic lesion, representative images from animal 4.)

An overview image of the femur using BSE microscopy is shown in Fig. 3.12A, with the mineralized tissue of the bone being intact except for the cortical lesion close to the posterior growth plate (enlargement in Fig. 3.12B). The cortical bone is resorbed in nearly the entire cortical thickness, with only a thin layer remaining on the endocortical side. This suggests that the lesion originates on the periosteal side as shown in our eroded bone patch analysis. In the progression of such small osteolytic lesion, the entire lacunae and canaliculi network is resorbed (Fig. 3.12C). The collagen analysis with SHG also shows, that all fibrillar collagen type I fibers that were part of the cortical bone have been resorbed (Fig. 3.12D). Interestingly, the thick collagen layer in the periosteum is still intact (Fig. 3.12D). The lesion region is now filled with a completely new soft tissue, with high cell density of larger size, than most cells found in other regions of the bone (Fig. 3.12E). The intact cortical bone on the anterior side is visible in Fig. 3.12A (with an enlargement in F). In comparison to the lesion region, the mineralized tissue (Fig. 3.12F) and the lacunae and canaliculi network within is fully intact (Fig. 3.12G). The entire mineralized tissue is filled with aligned collagen type I fibers (Fig. 3.12H) and an intact thick layer of aligned collagen in the periosteum can be seen. The bone marrow shows small cells and no soft tissue

can be seen in the area of the cortical bone.

An overview image of the tibia using BSE microscopy is shown in Fig. G.1A, with the mineralized tissue of the bone being intact except for the trabecular lesion on the anterior growth plate (enlargement in Fig. G.1B). The mineralized part of the growth plate is visibly thinned out in that region and the surrounding trabeculae show a rough surface, indicating an ongoing erosion of the tissue. The CLSM image of the rhodamine-stained tissue (Fig. G.1C) shows the same lesion and no lacunae or canaliculi can be observed in the non mineralized region. The collagen fibers as shown in Fig. G.1D follow the same erosion pattern shown in Fig. G.1B and C and seem to get resorbed together with the mineral tissue. The growth plate on the posterior side on the other hand is still intact (Fig. G.1A and F). The mineral layer of the growth plate is much thicker than in the lesion area, which is visible both in the BSE microscopy image (Fig. G.1F) and in the rhodamine stained CLSM image (Fig. G.1G), where both the edge of the mineralized region and the intact lacunae and canaliculi are visible. The collagen fibers are also aligned along the borders of the mineralized tissue (Fig. G.1H) without any sudden ends, as seen in the lesion region (Fig. 3.12D).

In summary, in both early cortical and trabecular lesions, the mineralized tissue, embedded lacunae and canaliculi, as well as collagen fibers within mineralized tissue are all fully resorbed and replaced by a new soft tissue with high density of cells larger than those normally found in the bone marrow or periosteal tissue.

CHAPTER 4

Discussion

The aim of this work was to develop an experimental mouse model of breast cancer bone metastasis for the 3D visualization and characterization of the early bone metastatic niche. We used microCT-based time-lapse morphometry for our *in vivo* experiments, and further developed the method. In the first part of the study, we added a new bone surface interface definition, and by segmenting epiphysis and metaphysis, we were able to create a baseline of bone (re)modeling in 12-week-old, female BALB/c nude mice, that is more physiologically relevant for studying metastasis. With the help of this baseline, we further developed the microCT-based method to detect alterations in bone (re)modeling due to early bone metastasis. With a new eroded bone patch analysis tool, osteolytic lesions in the cortical bone were detected and their growth over time was quantified. Visualizing bone (re)modeling, osteolytic lesions in the trabecular bone primary spongiosa right at the mineralized growth plate were identified. Finally we applied an *ex vivo* analysis pipeline that allowed us to study the distribution of cancer cells in the intact bone in 3D, analyze cancer cell and cell cluster proliferation state, characterize the FN network in the ECM, as well as an in-depth analysis of the osteolytic lesion physical microenvironment in both cortical and trabecular bone. The following chapter puts our work in the context of other studies and starts with our findings in physiological bone (re)modeling, followed by pathological bone (re)modeling and the detection of osteolytic lesions. Then the detection of cancer cells in the intact bone and the further analysis on proliferation and FN network are discussed, followed by our characterization of small osteolytic lesions with various *ex vivo* methods.

4.1 Physiological bone (re)modeling

We used microCT-based time-lapse morphometry to study physiological bone (re)modeling in healthy animals and found variations between epiphysis and metaphyis, femur and tibia, as well as spatial gradients in the metaphysis.

4.1.1 Extension of bone (re)modeling surface parameters and influence of curvature

The first fundamental step in this work was to build on the existing microCT-based time-lapse morphometry methods [66] [67] by adding new definitions for bone surface interface parameters that are influenced by bone curvature. We used the method to create a baseline and investigate physiological bone (re)modeling in cortical and trabecular bone of female 12-week-old mice.

In this work, we found that four distinct surfaces can be described in the bone (re)modeling process, which are all strongly influenced by the local bone curvature and therefore provide additional information about the spatio-temporal development of the mineralized tissue. For bone mineralization, the surface that can be described with static microCT or other imaging techniques and is visible after harvesting the bone, is the MS_{ST}/BS, newly introduced in this work. The MS_{CB}/BS on the other hand can only be studied with microCT-based time-lapse morphometry data, or if the bone has been labeled as it is done in classical 2D histomorphometric analysis. 2D histomorphometry was used in the past to confirm results of microCT-based time-lapse morphometry [66]. Birkhold et al. compared the MAR to standard 2D histomorphometry. They found slightly lower values for 3D microCT-based analysis, which can be explained by differences in resolution or a potential bias towards dominant labels for 2D histomorphometry [70]. Further insights into the mineralization behavior can be obtained by comparing the two surfaces, especially in the cortical bone, where the bone geometry plays an important role. In trabecular bone on the other hand, the main influence on surface parameters, is the overall bone (re)modeling. As trabecular bone is highly dynamic, the MS_{CB}/BS is significantly smaller than the MS_{ST}/BS.

For bone erosion, the in this work newly introduced ES_{CB}/BS is the surface present after harvesting the bone, but can only be studied if prior knowledge of the bone status (for example through a microCT scan) is available. The same holds true for the ES_{ST}/BS, which is already eroded and therefore no longer detectable. Both erosion surfaces can only be studied well with the help of microCT-based

time-lapse morphometry. The ES/BS is therefore not frequently used in other studies, but shows immense importance when studying osteolytic disease[111]. An important insight into the erosion geometry and the (re)modeling of the overall bone can be gained from the combination of both surfaces. We were able to show, that the constant bone interfaces are more sensitive to study physiological bone (re)modeling in cortical bone, while the soft tissue interfaces are better suited to study physiological changes in trabecular bone. Only a combination of all four surface parameters allows a full picture of the dynamic processes though. The definition of the four distinct surfaces and the influence of bone curvature on them is a completely new approach, which can only be studied with the method of microCT-based time-lapse morphometry. In the past only the interfaces relevant for (re)modeling on a flat surface had been taken into account[66],[67],[70]. By describing all four relevant interfaces, we were able to expand the spatial understanding of the bone (re)modeling process.

Especially in the surface (re)modeling analysis, the threshold approach plays a critical role, as events could be missed or systemic errors introduced. A common and widely used approach is to use a fixed mean threshold[25]. This threshold is determined by calculating the threshold per ROI and time point with a common method, taking the mean of all these thresholds and afterwards using it as a fixed mean threshold for all ROIs. According to the guidelines[25], other threshold approaches are also applicable, if the mineralization is not expected to be the same for all ROIs at all time points. In this work, the differences in mineralization between day 0 and following time points day 17-45, were significantly different as shown in Fig. B.1. In case of a fixed mean threshold, the mineralized tissue of the reference scan is underestimated (Fig. B.1G and H, only orange voxels). The differences at day 45 are on the other hand very small, with only a few voxels added on the surface if a fixed mean threshold is used (Fig. B.1O and P, green voxels). Thus, with a fixed threshold, the mineralization over time is overestimated mainly by missing voxels at the reference time point. For this reason, in this study a variable threshold, determined by consistently using the Otsu method under visual control was used[106]. This approach captures the dynamics of mineralization best, especially since small differences between reference scan at day 0 and later time points are compared.

4.1.2 The importance of segmenting epiphyseal from metaphyseal regions in long bones when studying disease models

One major step in analyzing microCT derived data is choosing the right ROI[25]. We were able to show in Fig. 3.2, that the epiphysis and the metaphysis in the long bones of 12-week-old skeletally mature

mice, (re)model significantly different from each other and should therefore be analyzed separately from each other and treated independently. This observation can be explained by the differences in structural development in those two compartments. The epiphysis derives from ossified cartilage [110] and is, thus less prone to bone turnover, while the metaphysis undergoes several cycles of bone (re)modeling during development. The differences in the two regions might become smaller with age once long bone growth has reached a plateau. The differentiation of the regions is especially important in cancer research, as it has been shown, that the primary spongiosa close to the growth plate and the secondary spongiosa located in the metaphyseal region are prone to be the origins of trabecular osteolytic lesions [112]. We were able to show this with the help of a pilot model of metastasis (Fig. E.1). Even in the presence of a large osteolytic lesion, the epiphysis stays completely intact, while the primary spongiosa is heavily eroded, emphasizing the need to treat these regions separately [105]. This finding is in accordance with the work of He et al. where the intact epiphysis can be observed in histological sections even in the presence of large osteolytic lesions [103]. In addition, leaving out the primary spongiosa would lead to a lack of comprehensive information. Consequently, the segmentation of metaphysis and epiphysis gives the opportunity to study pathological (re)modeling in the entire affected metaphyseal region, without the interference of non-affected epiphyseal parts. This method of segmentation could also be interesting for other disease models like osteoarthritis, where the primary target is the subchondral bone, hence the epiphysis [113].

4.1.3 Differences in (re)modeling of morphologically similar regions in femur and tibia

Another important focus point of this study was the comparison of the femoral distal metaphysis and the tibial proximal metaphysis, two regions that share many morphological features and are interchangeably used in bone (re)modeling studies or disease models. The established parameters, including new surface parameters and the clear definition of the ROI allowed us to find significant differences in bone (re)modeling between the two regions, thus a baseline parameters for volume, surface and MAR/MRR in healthy bones of 12-week-old female BALB/c nude mice. The results were validated with the help of conventional static microCT analysis. The comparison show, that the femur is undergoing less (re)modeling and is therefore at a more stable homeostasis state at the described age (12-18 weeks). The tibia shows higher values of newly mineralized bone in both cortical and trabecular regions, visible in volume, surface and MAR. The differences we observe especially in the cortical bone,

might be related to the specific structure-function relationship caused by the biomechanical loading of tibia and femur in the mouse [114] [115] [116]. Most bone loading studies are performed on the tibia [117], due to accessibility with the experimental setup. However, the transfer of such limb-loading data to the femur or other long bones should be reconsidered in light of these findings.
If we compare our data to previously reported analysis using dynamic *in vivo* microCT of tibiae of 10-week-old BALB/c mice, we can see that the diaphysis is as expected (re)modeled far less [66], while the proximal tibia shows a similar trend of higher mineralization and lower erosion in both volume and surface. The higher mineralization rates are particularly interesting with regards to the study by Chiou et al., who found that animals injected with cancer conditioned media showed more mineralization on both cortical and trabecular bone [91]. They suggest a preference for cancer cells to home to newly immature mineralized regions and thus the tibia overall.

The rationale behind using these specific presented parameters for volume, surface and MAR/MRR over many other possible dynamic morphometry parameters, was to provide a broad picture of bone (re)modeling over time, while using read-out frequently reported in analogous studies using microCT-based time-lapse morphometry [66] [67] [70]. By combining volume and surface, we are able to study global and more detailed (curvature influenced) changes in bone (re)modeling, while the MAR and MRR describe the dynamics behind these processes. Therefore, with the combination of volume, surface and MAR/MRR, a global and dynamic result clearly showing the trends can be obtained in a short time, which is especially important with time-lapse *in vivo* studies.

4.1.4 Spatial gradients in bone (re)modeling

In addition to the temporal evolution of bone (re)modeling, we studied the spacial gradients in femur and tibia cortical bone, thus providing an additional spatio-temporal dimension to this baseline. As had been shown in the temporal evolution, the tibia has a higher mineralization starting closer to the growth plate and that stayed significantly higher for the entire metaphyseal region. The femur on the other hand has higher erosion values closer to the growth plate which needs to be considered when establishing osteolytic disease models. The spatial evolution of trabecular bone was not studied in this work, as it is strongly influenced by the curvature of the growth plate.

Overall, we have created an important baseline for physiological bone (re)modeling in frequently studied regions, using BALB/c nude mice, which is an important mouse strain used for studies in

metastatic bone disease. This is a crucial starting point to study early pathological or rare events. This physiological bone (re)modeling baseline enables us to further deepen our understanding of pathological procedures, for example in breast cancer bone metastasis.

4.2 (Re)modeling in the presence of (systemic) cancer cells and detection of osteolytic lesions

One of the most important accomplishments of this work, was to use the enhanced method of microCT-based time-lapse morphometry to study bone (re)modeling after cancer cell injection. We compared the (re)modeling behavior of tumor injected animals that did not form a detectable osteolytic lesion in any of the two limbs, to animals with physiological bone (re)modeling, discussed in section 4.2.1. In addition, we further developed the cortical bone analysis by creating an eroded bone patch analysis tool to detect small osteolytic lesions and track their volume over time. In a last step, we used the advanced visualization of the bone (re)modeling analysis to detect osteolytic lesions in the primary spongiosa of trabecular bone in both tibia and femur. Overall, we have successfully enhanced and used a powerful tool to study bone (re)modeling in the presence of cancer and introduced new advancements that allow us to detect and study small cortical and trabecular osteolytic lesions. This is discussed in 4.2.2 for lesions in cortical bone and in 4.2.3 for trabecular compartments.

4.2.1 Altered (re)modeling in animals without detectable osteolytic lesions

Our first analysis focused on animals that were injected with cancer cells but did not show evidence of osteolytic lesions in the tibia or femur based on microCT analysis. We wanted to investigate any systemic effect of circulating tumor cells (CTCs) or established tumors in other regions on bone (re)modeling in long bones. We observed significant changes in the trabecular bone (Fig. 3.5) that is more prone to bone (re)modeling and similar trends were also observed in cortical bone (Fig. D.1). Trabecular bone in both femur and tibia showed increased mineralization in volume and surface, with significant differences compared to control animals detectable at later time points (31 days onward). The differences were more pronounced in the tibia, which is also more (re)modeled in the physiological state compared to the femur. In addition, we found that the erosion is slightly down regulated in the tibia, shown in the volume and surface parameters, but specifically in the MRR. Lower MRR can also be detected for some time points in the femur. These findings show a clearly different trend compared

to animals with large osteolytic disease as described in the literature[75].

In the context of the pre-metastatic niche, Chiou et al. had shown a similar trend of more mineralized bone in animals injected with with tumor conditioned media, suggesting that the increased mineralization is not caused by direct cancer cell contact[91] and could precede osteolytic disease caused by metastasis. It has also been reported that cancer cells secrete factors that expand the osteoblast population, leading to 'educated' osteoblasts, which cause tumor cell suppression and p21 upregulation in tumor cells[118]. Currently, it is not known which tumor derived factors are responsible for the changes in osteoblast activity[119] and the only well established path is the stimulation of RANKL expression by parathyroid hormone-related protein (PTHrP)[100][120]. Brown et al. had shown though, that the location of tumor cells is crucial for the fate of bone cells, as cancer-induced changes in osteoblast and osteoclast numbers differed substantially depending on whether or not the bone cells were in direct contact with tumor cells. In particular, in areas not in direct contact with tumor cells, they showed increased numbers of osteoblasts and reduced numbers of osteoclasts, compared to controls, which aligns with our findings[119].

The presented findings cause a controversy in the field and we speculate about two possible mechanisms behind this increase in mineralization and partial reduction in erosion in animals with CTCs or metastasis in other sites, but no evidence of osteolytic lesions in the long bones. It could be a mechanism by breast cancer cells from the primary tumor or other secondary sites to prepare the premetastatic niche and increase the chances of establishing metastasis at later time points. For prostate cancer, which is accompanied by osteoblastic bone disease, it has been shown that their homing is supported by an osteoblast-rich niche[121]. The same has only been postulated for breast cancer with no clear evidence yet[91].

As alternative mechanism, it has been suggested that the increased mineralization might be a reaction to prevent the homing and proliferation of cancer cells, for example by creating 'educated' osteoblasts that suppress cancer cell proliferation[118]. Our current experiments cannot shed light on this controversial debate, but future experiments, combining microCT-based time-lapse morphometry to study bone (re)modeling in combination with techniques like intravital imaging to monitor the cell invasion are important tools. They could help us to understand the cascade of events and mechanisms behind this increase in bone mineralization in long bones during early bone metastasis, in absence of osteolytic lesions and with CTCs or established tumors in other regions.

Another point to be considered is the effect of radiation. The control PBS injected and the tumor animals without lesion were subjected to a high radiation dosage due to their by-weekly microCT scans. This might have had an influence on overall bone (re)modeling, and as we could see from later histological analysis, it caused a visible increase of adipocytes in the bone marrow. This has to be taken into account, especially in *ex vivo* studies. The here shown bone (re)modeling changes are still influenced mainly by the cancer cell injection, as all groups were treated with the same radiation dosage.

To summarize, here we have presented a temporal quantitative analysis of increase mineralization in trabecular bone of tibia and femur of animals with CTCs but without established osteolytic lesions in those long bones, in direct comparison with physiological (re)modeling in healthy animals.

4.2.2 Detection and tracking of small cortical osteolytic lesions based on micro-computed tomography

In this work we have presented a new mathematical tool to detect and track the evolution early osteolytic lesions, with initial sizes as small as $0.004\,\mathrm{mm}^3$. The eroded bone patch analysis helped us to reliably find cortical osteolytic lesions as early as two weeks after cancer cell injection (with the first time point measured). The tool was tested with healthy PBS injected animals for up to six weeks post injection, to rule-out the detection of non-pathological erosion patches.
A similar tool was developed in the past by Campbell et al., where a distance transformation was used to detect the osteolytic lesions [122]. A lowest distance of 150 µm for all planes (in x,y and z) was used in the work by Campbell et al., omitting the specific characteristic of osteolytic lesion to grow across the cortical thickness. In addition, the published tool was not tested on healthy mice, that undergo major (re)modeling especially at early ages (before 12 weeks). Our eroded bone patch analysis has proven reliable in finding early osteolytic lesions without detecting physiological eroded bone patches. With the help of this the eroded bone patch analysis tool we were able to detect two different kinds of osteolytic lesions in the cortical bone. The majority of cortical lesions in this study were either located or initiated at the periosteal side (n = 5 out of 6). This type of cortical lesion had not been much reported in the past, but we found it to be the most frequent form of lesion in our entire study. It is widely accepted, that osteoclasts are activated by cancer cells to cause osteolytic lesions [123] and osteoclasts have been reported to be located in the periosteum [124], making this one possible

mechanism for the formation of lesions at the periosteal region. Wang et al. on the other hand showed, that osteoclast activity does not play a major role in the early stages of metastasis [125] and it has been debated, that tumor cells themselves might play a role in the resorption of mineralized bone [126]. The second type of cortical lesion found in this study, was an endocortical lesion with trabecular involvement. In this type of lesion both cortical and trabecular bone get eroded and we had shown the progression of such a lesion over a longer time with a pilot animal (Fig. E.1) [105].

In summary, we have developed a new and reliable tool to detect and study osteolytic lesions in cortical bone. We were able to differentiate two different types: lesions originated in the periosteal vs. endocortical site, which might be caused by different types of bone erosion.

4.2.3 Detection of small trabecular osteolytic lesions based on microcomputed tomography

Next to cortical lesions, we analyzed very early lesions in the trabecular bone. All of the lesions were detected two weeks after the cancer cell injection and were located at the growth plate area, eroding the mineralized primary spongiosa (n = 4). We found smaller lesions at the lateral and medial edge of the bone, and slightly larger lesions between the condyles. The growth plate is one of the most (re)modeled areas within the bone and further supports the idea, that (re)modeling could be a driver for metastasis. Previous studies have also found that younger mice that undergo high bone (re)modeling suffer from more metastasis than older animals after intracardiac injection, even if the same number of cells arrive to the bone [102]. To overcome this, we used skeletally mature 12-week-old mice, but the local (re)modeling that is present in animals at all age could be a driver for metastasis. This theory gets further supported by the fact that most lesions, cortical and trabecular, are found in the metaphysis, a more (re)modeled region than the diaphysis or epiphysis. On the other hand, we saw more (re)modeling in trabecular bone compared to cortical bone in both healthy and diseased animals. We did not find more osteolytic lesions in trabecular bone though. One reason for this could be, that trabecular lesions at early stages are more difficult to capture. In addition, the surface of cortical bone is also highly (re)modeled and a correlation between (re)modeling in specific areas and the onset of metastatic lesions would be highly interesting. Further studies with patient data could show if the observation of trabecular lesions starting at the growth plate also holds true in human disease, which might help to advance screening by localizing early events at specific areas.

In this study, trabecular lesions were detected visually with the help of both original microCT images and microCT-based time-lapse morphometry, which might also lead to an underestimation of trabecular lesions in this study. Ideally, an objective tool like the eroded bone patch analysis for cortical bone, should be established for the trabecular compartment. Cortical bone is dense and (re)modeled only in particular regions (endosteum and periosteum), which is an advantage when creating neighborhood based or other mathematical tools. Trabecular bone on the other hand, has many different morphological features, with larger trabeculae in the secondary spongiosa (20 – 70 µm [127]) and a very thin and dense network of trabeculae in the primary spongiosa. In addition, trabecular bone is far more dynamic than cortical bone and highly (re)modeled, as shown in this thesis [105]. These factors make it more difficult to establish specific parameters like the neighborhood analysis we have performed in cortical bone, in order to detect an osteolytic lesion in trabecular bone. As the primary spongiosa seems to be a key target for osteolytic lesion, a further segmentation into primary and secondary spongiosa might help with finding an adequate tool. The primary spongiosa is highly influenced by the 3D curvature of the growth plate though, which makes this segmentation quite complex. Overall, the data we have presented open up a lot of possibilities to establish a tool in the future to (semi)automatically detect osteolytic lesions in trabecular bone.

4.3 Cancer cell detection in the intact bone

After successfully establishing our *in vivo* model, we wanted to analyze the soft tissue and cellular parts involved in the process of breast cancer metastasis in the bone. The main critical step in this analysis is the detection of the breast cancer cells in the bone, which is usually done by section staining. In order to retrieve a more complete picture, we optically cleared the bones and analyzed the fluorescently labeled cancer cells in the intact bone with LSFM. In doing so, we had access to a far larger number of cells and much better spatial knowledge.

4.3.1 Cancer cell cluster localization

We studied the homing and localization of cancer cells and cell clusters for the first time in the intact 3D bone marrow, having the full spatial information. In addition, this gave us access to a far larger number of cells as roughly 8,000 cells were analyzed. The question of localization of cancer cell in the bone had been previously addressed in much detail using 2D sections, studying different types

of niches. Carlson et al. came to the conclusion, that cancer cells home in the perivascular niche, by analyzing the co-localization of the cells to blood vessels, osteoblasts and megakaryocytes [96]. Wang et al. on the other hand used immunological staining of RUNX2 and Osterix to show that cancer cells were in direct contact with cells expressing these factors and hence finding them to be in the osteogenic niche [125]. In our study we found cancer cells to be sitting preferably close to the endocortical bone surface, with a clear preference for the anterior side also seen in 2D sections, which is in contrast with previous findings that see a preference in the medial region [121]. Our findings could align with findings from both Carlson et al. as the cortical bone is permeated by many fine trans-cortical blood vessels [18]. Also the finding of Wang et al. would align with our results as the endocortical bone surface is home to bone forming osteoblasts and a high level of mineralization is occurring on the endocortical bone of the tibia as we could show in this work [105]. A more detailed analysis of the intact niche making use of additional stainings for blood vessels and osteoblasts could shed light on the highly debated question of the preferred niche for cancer cells.

In our work, we show for the first time that already two weeks post-injection cancer cells can be found in different long bones (femur, tibia and fibula) and in all bone compartments including the epiphysis, metaphysis and diaphysis. This is specifically interesting in light of our *in vivo* microCT-based study. We clearly described a preference for osteolytic lesions to form in highly (re)modeled areas, like the primary spongiosa. In addition, no lesion was detected in the epiphysis or the diaphysis (visual control), leaving the metaphysis as the preferred site. Therefore, the ability for the cancer cells to reach certain locations is not sufficient as an explanation for the formation of osteolytic lesions. This rather strengthens the hypothesis of antimetastatic niches as recently postulated for the skeletal muscle and parts of the bone marrow, describing inhospitable microenvironments where metastases occur rarely, if ever. Tumor cells are able to disseminate to these sites, but cannot colonize them in a meaningful timeframe, leading to the term 'antimetastatic' [128].

4.3.2 Cluster formation

The size of the eGFP+ breast cancer cells that were found in the 3D analysis was around 30 µm in diameter. In combination with IF imaging of 2D sections with CLSM, it was shown that the cells form small very tight clusters. These clusters were mostly found in the bone marrow compartment but also on the periosteal side. Cells were rarely detected as single cells, but often in small clusters of 2-3 cells or in line like 'pearls on a string' (Fig. 3.9). In addition, we found large cancer cell clusters

of up to several hundred micrometer diameter in the periosteum (Fig. 3.9E). Similar observations of large clusters could not be made in the bone marrow. This might indicate that only small clusters or single cells can traverse capillaries and home in the bone marrow. In addition, the large clusters in the periosteum could be a sign of a more advanced stage of metastasis and are well in line with the osteolytic lesions we find in our microCT analysis, starting at the periosteum. The ability for cancer cells to form clusters has been described in the past and it was shown that clusters have a higher potential to survive and form lesions than single CTCs[129]. In this work we show for the first time the localization and size of clusters with 3D imaging of (intact) bones using LSFM and validation with detailed IF imaging of 2D sections. Further studies are necessary to understand the process behind the formation of these tight clusters and their metastatic potential depending on their localization.

4.4 Characterization of cancer cells in the bone marrow

The bone marrow has been shown ot be both a metastatic and antimetastatic niche[128]. In order to understand the proliferative status of cancer cells we investigated the Ki67 proliferation marker. To characterize the surrounding ECM, we analyzed the FN protein network. Both analyses were performed with IF staining of 2D sections and CLSM imaging.

4.4.1 Cancer cell cluster proliferative status

High proliferation is a sign for an outgrowing metastasis, often stained for with the proliferation marker Ki67. The absence of this marker in combination with other stainings (for example p21), is currently used to show that cells are in a dormant, non active state. Miller et al. showed in the past, that the absence of Ki67 is a clear signal, that a cell is in G0/G1 phase, but even positively stained cells could be in a G0/G1 state[130]. Therefore, Ki67 alone cannot be used as a marker for dormancy, but it is an important indicator to show if metastatic cell clusters is not yet highly proliferative or the opposite holds true. We found that only around a third of the cell clusters analyzed had a clear signal for Ki67+, and could therefore be categorized as active. Especially in the diaphysis, we found many cells with no or only a partial Ki67+ signal on the edge. This supports the theory that certain regions of the bone marrow could be antimetastatic[128] and therefore resulting in a low proliferation of cancer cells homing there. Further investigations using additional dormancy markers like p21 could be helpful to establish the idea of bone compartment dependent antimetastatic or dormancy inducing regions. The

(re)modeling of these regions studied with microCT-based time-lapse morphometry could in addition be used to investigate the role of newly mineralized tissue on the activity of homed cancer cells.

4.4.2 Fibronectin microenvironment in the bone marrow

The influence of the ECM in the bone marrow on bone metastasis progression is currently understudied. We were able to show, that cancer cells have a clear preference to home close to dense FN fibers, with FN being a key ECM component. FN is also known to be incorporated between endothelial and perivascular cells in blood vessels [131]. This leaves room for two possible hypotheses: 1) a preference for cancer cells to home in the perivascular niche due to the access to vascularization or 2) a preference to homing in FN rich areas. Further studies are necessary to understand the interactions between cancer cells an FN, since our study clearly shows an abundance of the protein in the bone marrow and the preference for cancer cells to home close to dense FN areas.

Changes in stiffness of the microenvironment strongly influence cell fate (e.g. stem cells) [43]. In the context of cancer this has been recently shown by Di Martino et al. investigating the role of collagen type III in the context of cancer cell dormancy [132]. FN on the other hand is an important component of the ECM interacting with collagen, as collagen type I deposition is primarily dependent on previously assembled FN networks [133]. In addition it has been shown that the FN tension is dramatically decreased in tissues infiltrated by cancer cells, caused by the presence of alpha-smooth muscle actin (α-SMA) expressing myofibroblasts (also known as cancer-associated fibroblasts) [45]. Altogether, this suggests that the complex biophysical microenvironment with stiffness gradients, in part determined by the interaction of various ECM structural components, might play a crucial role in the establishment of larger lesions. Molecular processes involved in the sensation of stiffness changes referred to as mechanotransduction are currently investigated. A prominent member is the yes-associated protein (YAP)/tafazzin (TAZ) pathway [134]. In a collaborative project with another doctoral researcher in our group, Dr. Bakhshandeh, we were able to show the stiffness dependent nuclear localization of the four-and-a-half LIM domains 2 (FHL2) protein, leading to p21 expression and breast cancer cell quiescence. IF staining of cancer cells or small cell clusters in the bone marrow showed a clearly nuclear FHL2 signal in the absence of Ki67. Within osteolytic lesion regions, the FHL2 protein was localized in the cytoplasm and a Ki67 signal was detected. The complementing *in vitro* studies show, that this effect and the resulting quiescence can be fully induced by changes in the stiffness of the surrounding 3D matrix (Bakhshandeh et al., in preparation). However, detailed mechanisms of mechanotransduc-

tion have rarely been fully elucidated, particularly *in vivo*, and are an important focus of ongoing research.

4.5 Characterization of small osteolytic lesions

With the help of our powerful *in vivo* microCT-based eroded bone patch analysis tool we were able to detect osteolytic lesions two weeks after the cancer cells had been injected. At this point the lesions were still small and in a very early phase. In addition, we used the microCT-based time-lapse morphometry visualization to detect osteolytic lesions in trabecular bone at the same early time point. With our *ex vivo* multimodal analysis, we have studied different parts of the metastatic cortical and trabecular lesions, with focus on the mineralized tissue, collagen fibers and the type of new tissue/cells invading the space.

As we have described before, different types of osteolytic lesions have been detected: cortical lesions on the periosteal side, endocortical lesions with trabecular erosion and fully trabecular lesions. Here we show the *ex vivo* analysis for a cortical lesion starting at the periosteum and a trabecular lesion close to the growth plate. In both cases the BSE microscopy images confirmed the microCT findings. Previous work focusing on the mineralized tissue has shown animals with massive lesions, 4-6 weeks after injection, where much of the mineralized tissue had already been eroded and, hence, no clear localization and trace of the onset of the lesion could be made [103].

With the help of rhodamine staining and CLSM, as well as SHG imaging, we were able to show that even in small lesions, the collagen fibers and the entire mineralized tissue were resorbed. This means that important structures of the canaliculi network were dramatically disrupted, especially in the case of cortical lesions spanning the entire cortical thickness. The canaliculi network plays an important role in the mechano-sensitivity of the bone through fluid flow patterns [27]. The disruption of these patterns and the apoptosis of osteocytes could in return change the 'biophysical sensitivity' of larger bone areas. In addition, the network architecture could get hijacked by cancer cells for long distance signaling to other bone parts. Future work could focus on the exact location of cancer cells in relation to lacunae and canaliculi, to answer some of the important questions raised within this work.

CHAPTER 5

Conclusion

Aim 1*: To define baseline parameters of physiological (re)modeling in specific bone areas, in order to quantify the dynamics of bone (re)modeling in a reliable way, while also being sensitive enough to detect region specific pathological alterations.*

In this work we presented a new baseline for physiological bone (re)modeling in skeletally mature 12-week-old female BALB/c nude mice. We advanced the method of microCT-based time-lapse morphometry by introducing new definitions of bone surface interfaces and showing the influence of local bone curvature. In addition, we improved the selection of the ROI, segmenting the epiphysis from the metaphysis, allowing the analysis of the full metaphysis including primary and secondary spongiosa, which is specifically important in osteolytic cancer disease models. By doing so we have created a powerful tool to investigate the dynamics of bone (re)modeling using volume, surface and apposition/resorption rate. We were able to show major differences in the (re)modeling of epiphysis and metaphysis, which have never been shown before. We also showed variations in the (re)modeling between morphologically similar regions in proximal tibia and distal femur. The here established *in vivo* method could have applications in various disease models including osteolytic alterations like breast cancer metastasis or multiple myeloma, as well as osteoporosis or osteoblastic alterations as seen in osteosarcoma and prostate cancer metastasis.

Aim 2*: To quantify changes in the bone (re)modeling dynamics after cancer cell injection in animals without detectable osteolytic lesions in the long bones.*

Using this advanced method of microCT-based time-lapse morphometry, we were able to show differences in animals with pathological bone (re)modeling without detectable osteolytic lesions compared

with physiological bone (re)modeling in control animals. Surprisingly, it was found that the animals have higher rates of newly mineralized bone in comparison to healthy animals. This finding aligns with previous studies, but the dynamics and site specific differences were shown quantitatively for the first time in this work. In addition, it highlights the need to understand if this enhanced mineralization is resulting in a premetastatic or antimetastatic niche. MicroCT-based time-lapse morphometry combined with other advanced imaging techniques could be an important tool in answering this question.

***Aim 3**: To establish a sensitive and robust tool able to detect the onset and track the growth of small osteolytic lesions in cortical bone, while being able to distinguish them from physiological bone erosion.*
We then developed a novel and reliable eroded bone patch analysis tool to detect early cortical osteolytic lesions and track their evolution over time. Small lesions were already detected at the first day of measurement two weeks after cancer cell injection. The eroded bone patch analysis tool was tested with control animals to rule out any erosion patches stemming from physiological bone erosions of 12-week-old female BALB/c nude mice. With the help of this novel tool, we were able to identify osteolytic lesions at an early time point, track them over several measurements and quantify the volume changes over time. Thanks to 3D visualization we were able to identify the location of the onset: some lesions started in the periosteum, others in the endocortical bone. This had not been shown in such detail before.

***Aim 4**: To detect and categorize all types of osteolytic lesion in both cortical and trabecular bone.*
In addition, we found the onset of trabecular lesion at the growth plate in the primary spongiosa thanks to the 3D visualization of the bone (re)modeling analysis. This region is often not studied as it is very porous and cannot easily be separated from the epiphysis, but is highly (re)modeled, which might enhance its potential for metastatic outgrowth. The combination of both cortical and trabecular analysis allowed us to describe three different types of osteolytic lesions forming from breast cancer metastasis in the bone: 1) cortical lesions initiating in the periosteum, 2) cortical lesions initiating in the endocortical bone with trabecular erosion and 3) trabecular lesions in the primary spongiosa. It is the first time that such a detailed analysis and categorization of different lesion localization has been performed and this shows great potential to enhance screenings in clinical cases.

***Aim 5**: To visualize and map in 3D fluorescently labeled cancer cells and small cell clusters in the marrow of 3D (intact) bones using 3D LSFM.*
We started the *ex vivo* analysis by the invasion of cancer cells in the bone marrow and in the surround-

ing bone tissue, visualizing 3D (intact) bones using optical clearing and LSFM. We quantified the size and location of up to 8,000 cells, gaining completely new statistical relevance and spatial information. We found that in the bone marrow, cancer cells predominantly home close to the cortical bone surface with a preference for the anterior side as also seen in 2D sections. We also found that most cells tend to home in the form of small cell clusters with a mean diameter of around 30 µm. Our findings support the hypothesis of specific regions having a positive or negative influence on the ability to form osteolytic lesion, as cancer cells were detected in all parts of the bone environment, including the metaphysis, epiphysis, periosteum and periosteal muscle. However, osteolytic lesions were predominantly found with microCT in metaphyseal cortical and trabecular bone. Such 3D correlation between presence of cancer cells and site-specific appearance of lesions is shown in this work for the first time.

***Aim 6**: To characterize the proliferation activity and the structural microenvironment of cancer cells and small cell clusters in the bone marrow.*

We then investigated the proliferative state of cancer cell clusters and characterized the FN network in the ECM surrounding them. We found that at least a third of the cancer cells and cell clusters colonizing the bone marrow were not proliferative. Overall, 85% of colonizing cells had a strong tendency to home close to dense FN networks. These first findings invite further investigations of the ECM architecture, composition and correlations with the proliferative state of cancer cells and cells clusters.

***Aim 7**: To characterize the structural and biophysical microenvironment of small osteolytic lesions at early stage bone metastasis using multiscale and multimodal imaging tools.*

In the last part of this study, we studied the structural and biophysical microenvironment of the osteolytic lesion with different imaging tools. We showed that even in early stages of metastatic bone disease, the mineralized tissue including the collagen fibers are fully eroded in the osteolytic lesions and filled with new soft tissue with high cellular density metastatic cells.

Overall, we have established a baseline for physiological bone (re)modeling using microCT-based time-lapse morphometry. We used this new baseline to detect pathological bone (re)modeling in tumor cell injected animals without detectable osteolytic lesions. As a next step, we developed a new mathematical tool to detect and analyze early osteolytic lesions in cortical bone. We visually detected trabecular lesions and classified all lesions according to their anatomical location. We were able to study the homing of cancer cells in the bone marrow with the help of optical clearing and LSFM for the first

time giving full 3D information about their size and spatial distribution. We then characterized the cancer cells in the bone marrow, as well as the ECM. Lastly, we studied early osteolytic lesions with multimodal methods characterizing the onset of such lesions for the first time (Fig. 5.1). Our work gives important 3D information and new perspectives on various states of cancer research including the debate on pre- or antimetastatic niches, homing and the onset of metastasis in the long bones.

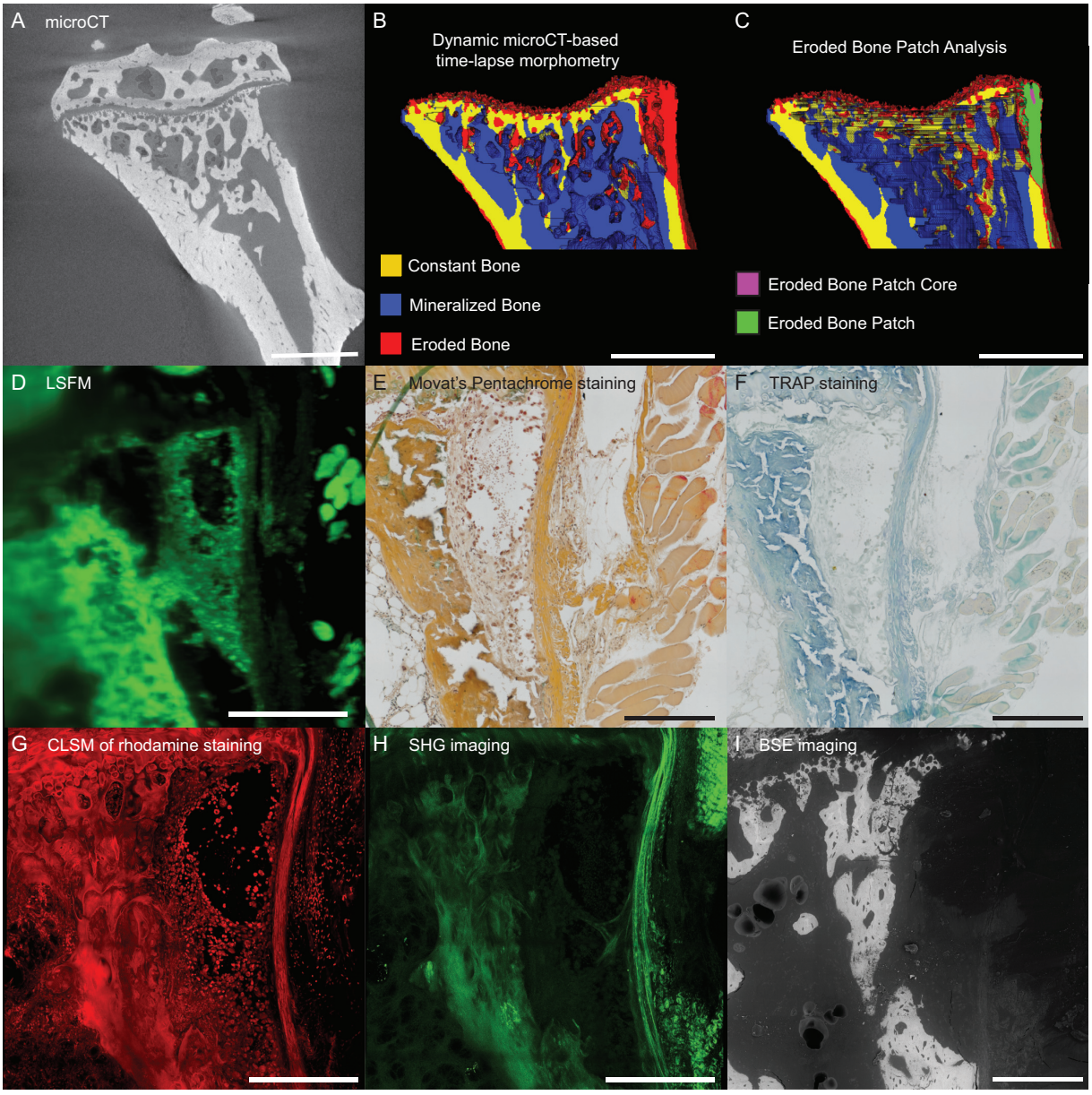

Fig. 5.1: **Multiscale characterization of a larger osteolytic lesion with *in vivo* and *ex vivo* methods** Larger osteolytic lesion in the proximal metaphysis, visualized (A) with *ex vivo* microCT and *in vivo* bone (re)modeling shown in (B) with (C) additional eroded bone patch analysis. Visualization with (D) LSFM, (E) Movat's pentachrome staining, (F) TRAP staining, (G) CLSM of rhodamine stained tissue, (H) with SHG imaging showing the collagen fibers, (I) BSE imaging showing the mineralized tissue and . (Scale bars correspond to 1,000 µm (A-C), 500 µm (D) and 250 µm (E-I), data shown for day 28 from left tibia of animal 6.)

CHAPTER 6

Future Perspective

With the advanced method of microCT-based time-lapse morphometry, future work could focus on the bone (re)modeling before osteolytic lesions occur. To do so, an additional measurement time point (e.g. day 10) could be introduced. This should give the cells enough time to establish themselves in the bone marrow, but would still provide interesting details on bone (re)modeling in specific preferred lesion areas. Such an experimental design would show if newly mineralized bone is in general more permissive to osteolytic attack by cancer cells or is rather serving a protective function (anti-metastatic niche hypothesis).

Another experimental design using microCT-based time-lapse morphometry as a monitoring tool to study the effects of cancer cell derived factors, would be an injection of tumor conditioned media followed by an intracardiac injection with breast cancer cells. This would show both enhanced mineralization and the potential effect on the ability of cancer cells to metastasize in those regions.

In order to fully understand the onset of metastasis with the here used mouse model, a mathematical tool to detect and quantify trabecular lesions could be established. This would prove useful in many different experimental designs and could be used for other osteolytic or even osteoblastic disease models.

In addition, further cellular and molecular analyses of the found cancer cell clusters could be performed, to understand the cellular interactions and evaluate if they have an increased metastatic potential over single cells or smaller clusters. Especially the larger periosteal cancer cell clusters have not been shown before and in combination with the osteolytic lesions we found initiating from the periosteum, this opens up many interesting research questions.

Further this work could be paired with new studies, ideally using 3D information, investigating the

role of osteoblasts and osteoclasts in the establishment of early osteolytic lesions. One major question here would be to understand if the cancer cells are able to erode the mineralized tissue themselves in these early stages. Both immunostaining and CLSM, as well as optical bone clearing and LSFM could prove to be powerful tools to study the cellular involvement in a spatial context.

Aside from the cellular microenvironment of cancer cells, the structural microenvironment including different types of collagen, FN and other ECM proteins could be studied to better characterize the cancer cell niche in the bone. This work should ideally be complemented by studies visualizing the bone vasculature (ideally in 3D), for example with the help of bone clearing and LSFM. Ongoing research questions about the perivascular and endocortical niche could be better understood with such experiments.

Another really interesting further perspective that we could only touch on is the involvement of osteocytes and the lacuno-canaliculi network in the context of early osteolytic lesions. A broader network analysis around early cortical lesions could show how the bone mechanosensitivity gets influenced during early metastasis and if cancer cells have a preference to home in regions of specific network architecture. The hypothesis of cancer cells hijacking the canaliculi network could explain the rapid and exponential establishment of lesions in the bone.

Our work is a great starting point for more in depth analysis of the structural and biophysical bone microenvironment and its interplay with the cellular and molecular components, both in physiological and pathological settings. This work opens many new avenues of research and we were able to show that only an interdisciplinary approach will bring us closer to the biological reality of bone and metastasis research.

Publications

1. Young, Sarah A. ; Rummler, Maximilian ; Taïeb, Hubert M. ; Garske, Daniela S. ; Ellinghaus, Agnes ; Duda, Georg N. ; Willie, Bettina M. ; Cipitria, Amaia: In vivo microCT-based time-lapse morphometry reveals anatomical site-specific differences in bone (re)modeling serving as baseline parameters to detect early pathological events. In: *Bone* 161 (2022)

2. Young, Sarah A. ; Heller, Anna-Dorothea; Garske, Daniela S.; Rummler, Maximilian; Qian, Victoria; Ellinghaus, Agnes; Georg, Duda; Willie, Agnes; Grüneboom, Anika; Cipitria, Amaia: 3D visualization of the early bone metastatic niche and in vivo monitoring of pathological changes in bone structure and dynamics (in preparation)

3. Bakhshandeh, Sadra; Taïeb, Hubert M.; Varadarajan, Adithi R.; Hücker, Sarah M.; Lu, Xin; Garske, Daniela S.; Young, Sarah A.; Contzen, Jörg; Gossen, Manfred; Kirsch, Stefan; Warfsmann, Jens; Honarnejad, Kamran; Klein, Christoph A.; Cipitria, Amaia: Quiescence-inducing 3D-engineered matrix uncovers drug protective signaling pathway of dormant cancer cells (in submission)

Conference contributions

2019 S. A. E. Young "Multiscale characterization of the extracellular matrix in breast cancer bone micrometastasis", ECTS PhD Training course, Bologna, Italy. (student presentation)

2019 S. A. E. Young, D. S. Garske, A. Ellinghaus, M. Rummler, G. N. Duda, B. M. Willie, A. Cipitria, "In vivo monitoring of the extracellular matrix in breast cancer bone metastasis", EACR Conference: Seed and Soil - Mechanism of Metastasis, Berlin, Germany. (poster presentation)

2019 S. A. E. Young, D. S. Garske, A. Ellinghaus, M. Rummler, G. N. Duda, B. M. Willie, A. Cipitria, "In vivo monitoring of the extracellular matrix in breast cancer bone metastasis", EACR Conference: Goodbye flat biology - Advancing 3D-based Models for Cancer Biology and Drug Discovery, Berlin, Germany. (poster presentation)

2019 S. A. E. Young, D. S. Garske, A. Ellinghaus, M. Rummler, G. N. Duda, B. M. Willie, A. Cipitria, "In vivo monitoring of the extracellular matrix in breast cancer bone metastasis", BSRT PhD Symposium 'The Hitchhiker's Guide to Regenerative Therapies: The Role of Space and Time in Healing Processes', Berlin, Germany. (poster presentation)

2021 S. A. E. Young, A. D. Heller, D. S. Garske, M. Rummler, V. Qian, H. M. Taieb, A. Ellinghaus, P. Fratzl, G. N. Duda, A. Grüneboom, B. M. Willie, A. Cipitria, "Longitudinal microCT in vivo monitoring of pathological bone remodeling in breast cancer bone metastasis", BSRT PhD Symposium 'A Deep Dive Into Science: Swimming through the Seven Seas of Regenerative Medicine' (virtual). (student presentation)

2022 S. A. E. Young, A. D. Heller, D. S. Garske, M. Rummler, V. Qian, H. M. Taieb, A. Ellinghaus, G. N. Duda, A. Grüneboom, B. M. Willie, A. Cipitria, "3D visualization of the early bone metastatic niche and in vivo monitoring of pathological changes in bone structure and dynamics", EACR Conference: The Structural Microenvironment: Breaking down the walls of cancer (virtual).

(poster presentation)

2022 S. A. E. Young, A. D. Heller, D. S. Garske, M. Rummler, V. Qian, H. M. Taieb, A. Ellinghaus, G. N. Duda, A. Grüneboom, B. M. Willie, A. Cipitria, "3D visualization of the early bone metastatic niche and in vivo monitoring of pathological changes in bone structure and dynamics", EMBO | EMBL Symposium Defining and defeating metastasis, Heidelberg, Germany. (poster presentation)

CHAPTER 7

Bibliography

[1] Karsenty, Gerard ; Kronenberg, Henry M. ; Settembre, Carmine: Genetic Control of Bone Formation. In: *Annual Review of Cell and Developmental Biology* 25 (2009), nov, Nr. 1, 629–648. http://dx.doi.org/10.1146/annurev.cellbio.042308.113308. – DOI 10.1146/annurev.cellbio.042308.113308

[2] Crockett, J. C. ; Rogers, M. J. ; Coxon, F. P. ; Hocking, L. J. ; Helfrich, M. H.: Bone remodelling at a glance. In: *Journal of Cell Science* 124 (2011), apr, Nr. 7, 991–998. http://dx.doi.org/10.1242/jcs.063032. – DOI 10.1242/jcs.063032

[3] Yin, Tong ; Li, Linheng: The stem cell niches in bone. In: *Journal of Clinical Investigation* 116 (2006), Nr. 5, S. 1195–1201. http://dx.doi.org/10.1172/JCI28568. – DOI 10.1172/JCI28568

[4] Zanetti, Costanza ; Krause, Daniela S.: "Caught in the net": the extracellular matrix of the bone marrow in normal hematopoiesis and leukemia. In: *Experimental Hematology* 89 (2020), sep, 13–25. http://dx.doi.org/10.1016/j.exphem.2020.07.010. – DOI 10.1016/j.exphem.2020.07.010

[5] Teitelbaum, Steven L.: Osteoclasts: What Do They Do and How Do They Do It? In: *The American Journal of Pathology* 170 (2007), feb, Nr. 2, 427–435. http://dx.doi.org/10.2353/ajpath.2007.060834. – DOI 10.2353/ajpath.2007.060834

[6] Clarke, Bart: Normal Bone Anatomy and Physiology. In: *Clinical Journal of the American Society of Nephrology* 3 (2008), nov, Nr. Supplement 3, S131–S139. http://dx.doi.org/10.2215/CJN.04151206. – DOI 10.2215/CJN.04151206

[7] Croucher, Peter I. ; McDonald, Michelle M. ; Martin, T. J.: Bone metastasis: the im-

portance of the neighbourhood. In: *Nature Reviews Cancer* 16 (2016), jun, Nr. 6, 373–386. http://dx.doi.org/10.1038/nrc.2016.44. – DOI 10.1038/nrc.2016.44

[8] Méndez-Ferrer, Simón ; Bonnet, Dominique ; Steensma, David P. ; Hasserjian, Robert P. ; Ghobrial, Irene M. ; Gribben, John G. ; Andreeff, Michael ; Krause, Daniela S.: Bone marrow niches in haematological malignancies. In: *Nature Reviews Cancer* 20 (2020), may, Nr. 5, 285–298. http://dx.doi.org/10.1038/s41568-020-0245-2. – DOI 10.1038/s41568–020–0245–2

[9] Abeynayake, Nethmi ; Arthur, Agnieszka ; Gronthos, Stan: Crosstalk between skeletal and neural tissues is critical for skeletal health. In: *Bone* 142 (2021), jan, Nr. September 2020, 115645. http://dx.doi.org/10.1016/j.bone.2020.115645. – DOI 10.1016/j.bone.2020.115645

[10] Coutu, Daniel L. ; Kokkaliaris, Konstantinos D. ; Kunz, Leo ; Schroeder, Timm: Three-dimensional map of nonhematopoietic bone and bone-marrow cells and molecules. In: *Nature Biotechnology* 35 (2017), dec, Nr. 12, 1202–1210. http://dx.doi.org/10.1038/nbt.4006. – DOI 10.1038/nbt.4006

[11] Klamer, Sofieke ; Voermans, Carlijn: The role of novel and known extracellular matrix and adhesion molecules in the homeostatic and regenerative bone marrow microenvironment. In: *Cell Adhesion and Migration* 8 (2014), nov, Nr. 6, 563–577. http://dx.doi.org/10.4161/19336918.2014.968501. – DOI 10.4161/19336918.2014.968501

[12] Nilsson, Susan K. ; Debatis, Michelle E. ; Dooner, Mark S. ; Madri, Joseph A. ; Quesenberry, Peter J. ; Becker, Pamela S.: Immunofluorescence Characterization of Key Extracellular Matrix Proteins in Murine Bone Marrow In Situ. In: *Journal of Histochemistry and Cytochemistry* 46 (1998), mar, Nr. 3, 371–377. http://dx.doi.org/10.1177/002215549804600311. – DOI 10.1177/002215549804600311

[13] Gao, Yue ; Liu, Shuyun ; Huang, Jingxiang ; Guo, Weimin ; Chen, Jifeng ; Zhang, Li ; Zhao, Bin ; Peng, Jiang ; Wang, Aiyuan ; Wang, Yu ; Xu, Wenjing ; Lu, Shibi ; Yuan, Mei ; Guo, Quanyi: The ECM-Cell Interaction of Cartilage Extracellular Matrix on Chondrocytes. In: *BioMed Research International* 2014 (2014), 1–8. http://dx.doi.org/10.1155/2014/648459. – DOI 10.1155/2014/648459

[14] Hynes, Richard O.: The Extracellular Matrix: Not Just Pretty Fibrils. In: *Science* 326 (2009),

nov, Nr. 5957, 1216–1219. http://dx.doi.org/10.1126/science.1176009. – DOI 10.1126/science.1176009

[15] Florencio-Silva, Rinaldo ; Sasso, Gisela Rodrigues da S. ; Sasso-Cerri, Estela ; Simões, Manuel J. ; Cerri, Paulo S.: Biology of Bone Tissue: Structure, Function, and Factors That Influence Bone Cells. In: *BioMed Research International* 2015 (2015), Nr. 6, 1–17. http://dx.doi.org/10.1155/2015/421746. – DOI 10.1155/2015/421746

[16] Williams, Rebecca M. ; Zipfel, Warren R. ; Webb, Watt W.: Interpreting Second-Harmonic Generation Images of Collagen I Fibrils. In: *Biophysical Journal* 88 (2005), feb, Nr. 2, 1377–1386. http://dx.doi.org/10.1529/biophysj.104.047308. – DOI 10.1529/biophysj.104.047308

[17] Paris, Michael ; Götz, Andreas ; Hettrich, Inga ; Bidan, Cécile M. ; Dunlop, John W. ; Razi, Hajar ; Zizak, Ivo ; Hutmacher, Dietmar W. ; Fratzl, Peter ; Duda, Georg N. ; Wagermaier, Wolfgang ; Cipitria, Amaia: Scaffold curvature-mediated novel biomineralization process originates a continuous soft tissue-to-bone interface. In: *Acta Biomaterialia* 60 (2017), sep, 64–80. http://dx.doi.org/10.1016/j.actbio.2017.07.029. – DOI 10.1016/j.actbio.2017.07.029

[18] Grüneboom, Anika ; Hawwari, Ibrahim ; Weidner, Daniela ; Culemann, Stephan ; Müller, Sylvia ; Henneberg, Sophie ; Brenzel, Alexandra ; Merz, Simon ; Bornemann, Lea ; Zec, Kristina ; Wuelling, Manuela ; Kling, Lasse ; Hasenberg, Mike ; Voortmann, Sylvia ; Lang, Stefanie ; Baum, Wolfgang ; Ohs, Alexandra ; Kraff, Oliver ; Quick, Harald H. ; Jäger, Marcus ; Landgraeber, Stefan ; Dudda, Marcel ; Danuser, Renzo ; Stein, Jens V. ; Rohde, Manfred ; Gelse, Kolja ; Garbe, Annette I. ; Adamczyk, Alexandra ; Westendorf, Astrid M. ; Hoffmann, Daniel ; Christiansen, Silke ; Engel, Daniel R. ; Vortkamp, Andrea ; Krönke, Gerhard ; Herrmann, Martin ; Kamradt, Thomas ; Schett, Georg ; Hasenberg, Anja ; Gunzer, Matthias: A network of trans-cortical capillaries as mainstay for blood circulation in long bones. In: *Nature Metabolism* 1 (2019), feb, Nr. 2, 236–250. http://dx.doi.org/10.1038/s42255-018-0016-5. – DOI 10.1038/s42255–018–0016–5

[19] Chakraborty, Tonmoy ; Driscoll, Meghan K. ; Jeffery, Elise ; Murphy, Malea M. ; Roudot, Philippe ; Chang, Bo-Jui ; Vora, Saumya ; Wong, Wen M. ; Nielson, Cara D. ; Zhang, Hua ; Zhemkov, Vladimir ; Hiremath, Chitkale ; De La Cruz, Estanislao D. ; Yi, Yating ; Bezprozvanny, Ilya ; Zhao, Hu ; Tomer, Raju ; Heintzmann, Rainer ; Meeks, Julian P.

; Marciano, Denise K. ; Morrison, Sean J. ; Danuser, Gaudenz ; Dean, Kevin M. ; Fiolka, Reto: Light-sheet microscopy of cleared tissues with isotropic, subcellular resolution. In: *Nature Methods* 16 (2019), nov, Nr. 11, 1109–1113. http://dx.doi.org/10.1038/s41592-019-0615-4. – DOI 10.1038/s41592–019–0615–4

[20] Fratzl, P. ; Gupta, H. S. ; Paschalis, E. P. ; Roschger, P.: Structure and mechanical quality of the collagen–mineral nano-composite in bone. In: *J. Mater. Chem.* 14 (2004), Nr. 14, 2115–2123. http://dx.doi.org/10.1039/B402005G. – DOI 10.1039/B402005G

[21] Reznikov, Natalie ; Shahar, Ron ; Weiner, Steve: Three-dimensional structure of human lamellar bone: The presence of two different materials and new insights into the hierarchical organization. In: *Bone* 59 (2014), feb, 93–104. http://dx.doi.org/10.1016/j.bone.2013.10.023. – DOI 10.1016/j.bone.2013.10.023

[22] Liu, Yan ; Luo, Dan ; Wang, Tie: Hierarchical Structures of Bone and Bioinspired Bone Tissue Engineering. In: *Small* 12 (2016), sep, Nr. 34, 4611–4632. http://dx.doi.org/10.1002/smll.201600626. – DOI 10.1002/smll.201600626

[23] Weinkamer, Richard ; Kollmannsberger, Philip ; Fratzl, Peter: Towards a Connectomic Description of the Osteocyte Lacunocanalicular Network in Bone. In: *Current Osteoporosis Reports* 17 (2019), aug, Nr. 4, 186–194. http://dx.doi.org/10.1007/s11914-019-00515-z. – DOI 10.1007/s11914–019–00515–z

[24] Roschger, P. ; Paschalis, E. P. ; Fratzl, P. ; Klaushofer, K.: Bone mineralization density distribution in health and disease. In: *Bone* 42 (2008), Nr. 3, S. 456–466. http://dx.doi.org/10.1016/j.bone.2007.10.021. – DOI 10.1016/j.bone.2007.10.021

[25] Bouxsein, Mary L. ; Boyd, Stephen K. ; Christiansen, Blaine A. ; Guldberg, Robert E. ; Jepsen, Karl J. ; Müller, Ralph: Guidelines for assessment of bone microstructure in rodents using micro-computed tomography. In: *Journal of Bone and Mineral Research* 25 (2010), jun, Nr. 7, 1468–1486. http://dx.doi.org/10.1002/jbmr.141. – DOI 10.1002/jbmr.141

[26] Dong, Pei ; Haupert, Sylvain ; Hesse, Bernhard ; Langer, Max ; Gouttenoire, Pierre-Jean ; Bousson, Valérie ; Peyrin, Françoise: 3D osteocyte lacunar morphometric properties and distributions in human femoral cortical bone using synchrotron radiation micro-CT im-

ages. In: *Bone* 60 (2014), mar, 172–185. http://dx.doi.org/10.1016/j.bone.2013.12.008. – DOI 10.1016/j.bone.2013.12.008

[27] Tol, Alexander F. ; Roschger, A. ; Repp, F. ; Chen, J. ; Roschger, P. ; Berzlanovich, A. ; Gruber, G. M. ; Fratzl, P. ; Weinkamer, Richard: Network architecture strongly influences the fluid flow pattern through the lacunocanalicular network in human osteons. In: *Biomechanics and Modeling in Mechanobiology* (2019), dec. http://dx.doi.org/10.1007/s10237-019-01250-1. – DOI 10.1007/s10237–019–01250–1

[28] Schemenz, Victoria ; Gjardy, André ; Chamasemani, Fereshteh F. ; Roschger, Andreas ; Roschger, Paul ; Zaslansky, Paul ; Helfen, Lukas ; Burghammer, Manfred ; Fratzl, Peter ; Weinkamer, Richard ; Brunner, Roland ; Willie, Bettina M. ; Wagermaier, Wolfgang: Heterogeneity of the osteocyte lacuno-canalicular network architecture and material characteristics across different tissue types in healing bone. In: *Journal of Structural Biology* 212 (2020), nov, Nr. 2, 107616. http://dx.doi.org/10.1016/j.jsb.2020.107616. – DOI 10.1016/j.jsb.2020.107616

[29] Ayoubi, Mahdi ; Tol, Alexander F. ; Weinkamer, Richard ; Roschger, Paul ; Brugger, Peter C. ; Berzlanovich, Andrea ; Bertinetti, Luca ; Roschger, Andreas ; Fratzl, Peter: 3D Interrelationship between Osteocyte Network and Forming Mineral during Human Bone Remodeling. In: *Advanced Healthcare Materials* 10 (2021), jun, Nr. 12, 2100113. http://dx.doi.org/10.1002/adhm.202100113. – DOI 10.1002/adhm.202100113

[30] Sivaraj, Kishor K. ; Adams, Ralf H.: Blood vessel formation and function in bone. In: *Development* 143 (2016), aug, Nr. 15, 2706–2715. http://dx.doi.org/10.1242/dev.136861. – DOI 10.1242/dev.136861

[31] Morrison, Sean J. ; Scadden, David T.: The bone marrow niche for haematopoietic stem cells. In: *Nature* 505 (2014), jan, Nr. 7483, 327–334. http://dx.doi.org/10.1038/nature12984. – DOI 10.1038/nature12984

[32] Itkin, Tomer ; Gur-Cohen, Shiri ; Spencer, Joel A. ; Schajnovitz, Amir ; Ramasamy, Saravana K. ; Kusumbe, Anjali P. ; Ledergor, Guy ; Jung, Yookyung ; Milo, Idan ; Poulos, Michael G. ; Kalinkovich, Alexander ; Ludin, Aya ; Golan, Karin ; Khatib, Eman ; Kumari, Anju ; Kollet, Orit ; Shakhar, Guy ; Butler, Jason M. ; Rafii, Shahin ; Adams, Ralf H. ; Scadden, David T. ; Lin, Charles P. ; Lapidot, Tsvee: Distinct bone marrow blood vessels

differentially regulate haematopoiesis. In: *Nature* 532 (2016), apr, Nr. 7599, 323–328. http://dx.doi.org/10.1038/nature17624. – DOI 10.1038/nature17624

[33] Kusumbe, Anjali P. ; Ramasamy, Saravana K. ; Adams, Ralf H.: Coupling of angiogenesis and osteogenesis by a specific vessel subtype in bone. In: *Nature* 507 (2014), mar, Nr. 7492, 323–328. http://dx.doi.org/10.1038/nature13145. – DOI 10.1038/nature13145

[34] Ramasamy, Saravana K. ; Kusumbe, Anjali P. ; Itkin, Tomer ; Gur-Cohen, Shiri ; Lapidot, Tsvee ; Adams, Ralf H.: Regulation of Hematopoiesis and Osteogenesis by Blood Vessel–Derived Signals. In: *Annual Review of Cell and Developmental Biology* 32 (2016), oct, Nr. 1, 649–675. http://dx.doi.org/10.1146/annurev-cellbio-111315-124936. – DOI 10.1146/annurev–cellbio–111315–124936

[35] Grüneboom, Anika ; Kling, Lasse ; Christiansen, Silke ; Mill, Leonid ; Maier, Andreas ; Engelke, Klaus ; Quick, Harald H. ; Schett, Georg ; Gunzer, Matthias: Next-generation imaging of the skeletal system and its blood supply. In: *Nature Reviews Rheumatology* 15 (2019), sep, Nr. 9, 533–549. http://dx.doi.org/10.1038/s41584-019-0274-y. – DOI 10.1038/s41584–019–0274–y

[36] Ascenzi, A. ; Fabry, C.: Technique for dissection and measurement of refractive index of osteones. In: *The Journal of biophysical and biochemical cytology* 6 (1959), Nr. 1, S. 139–142. http://dx.doi.org/10.1083/jcb.6.1.139. – DOI 10.1083/jcb.6.1.139. – ISSN 00959901

[37] Stelzer, Ernst H. K. ; Strobl, Frederic ; Chang, Bo-Jui ; Preusser, Friedrich ; Preibisch, Stephan ; McDole, Katie ; Fiolka, Reto: Light sheet fluorescence microscopy. In: *Nature Reviews Methods Primers* 1 (2021), dec, Nr. 1, 73. http://dx.doi.org/10.1038/s43586-021-00069-4. – DOI 10.1038/s43586–021–00069–4

[38] Jansen, Lauren E. ; Birch, Nathan P. ; Schiffman, Jessica D. ; Crosby, Alfred J. ; Peyton, Shelly R.: Mechanics of intact bone marrow. In: *Journal of the Mechanical Behavior of Biomedical Materials* 50 (2015), oct, 299–307. http://dx.doi.org/10.1016/j.jmbbm.2015.06.023. – DOI 10.1016/j.jmbbm.2015.06.023

[39] Chen, Xinyue ; Hughes, Russell ; Mullin, Nic ; Hawkins, Rhoda J. ; Holen, Ingunn ; Brown, Nicola J. ; Hobbs, Jamie K.: Mechanical Heterogeneity in the Bone Microenvironment

as Characterized by Atomic Force Microscopy. In: *Biophysical Journal* 119 (2020), aug, Nr. 3, 502–513. http://dx.doi.org/10.1016/j.bpj.2020.06.026. – DOI 10.1016/j.bpj.2020.06.026

[40] Masic, Admir ; Bertinetti, Luca ; Schuetz, Roman ; Chang, Shu-Wei ; Metzger, Till H. ; Buehler, Markus J. ; Fratzl, Peter: Osmotic pressure induced tensile forces in tendon collagen. In: *Nature Communications* 6 (2015), may, Nr. 1, 5942. http://dx.doi.org/10.1038/ncomms6942. – DOI 10.1038/ncomms6942

[41] Engler, Adam J. ; Sen, Shamik ; Sweeney, H. L. ; Discher, Dennis E.: Matrix Elasticity Directs Stem Cell Lineage Specification. In: *Cell* 126 (2006), aug, Nr. 4, 677–689. http://dx.doi.org/10.1016/j.cell.2006.06.044. – DOI 10.1016/j.cell.2006.06.044

[42] Huebsch, Nathaniel ; Arany, Praveen R. ; Mao, Angelo S. ; Shvartsman, Dmitry ; Ali, Omar A. ; Bencherif, Sidi A. ; Rivera-Feliciano, José ; Mooney, David J.: Harnessing traction-mediated manipulation of the cell/matrix interface to control stem-cell fate. In: *Nature Materials* 9 (2010), jun, Nr. 6, 518–526. http://dx.doi.org/10.1038/nmat2732. – DOI 10.1038/nmat2732

[43] Trappmann, Britta ; Gautrot, Julien E. ; Connelly, John T. ; Strange, Daniel G. T. ; Li, Yuan ; Oyen, Michelle L. ; Cohen Stuart, Martien A. ; Boehm, Heike ; Li, Bojun ; Vogel, Viola ; Spatz, Joachim P. ; Watt, Fiona M. ; Huck, Wilhelm T. S.: Extracellular-matrix tethering regulates stem-cell fate. In: *Nature Materials* 11 (2012), jul, Nr. 7, 642–649. http://dx.doi.org/10.1038/nmat3339. – DOI 10.1038/nmat3339

[44] Chen, Christopher S. ; Mrksich, Milan ; Huang, Sui ; Whitesides, George M. ; Ingber, Donald E.: Geometric Control of Cell Life and Death. In: *Science* 276 (1997), may, Nr. 5317, 1425–1428. http://dx.doi.org/10.1126/science.276.5317.1425. – DOI 10.1126/science.276.5317.1425

[45] Fonta, Charlotte M. ; Arnoldini, Simon ; Jaramillo, Daniela ; Moscaroli, Alessandra ; Oxenius, Annette ; Behe, Martin ; Vogel, Viola: Fibronectin fibers are highly tensed in healthy organs in contrast to tumors and virus-infected lymph nodes. In: *Matrix Biology Plus* 8 (2020), nov, 100046. http://dx.doi.org/10.1016/j.mbplus.2020.100046. – DOI 10.1016/j.mbplus.2020.100046

[46] Parfitt, A. M.: Osteonal and hemi-osteonal remodeling: The spatial and temporal framework

for signal traffic in adult human bone. In: *Journal of Cellular Biochemistry* 55 (1994), jul, Nr. 3, 273–286. http://dx.doi.org/10.1002/jcb.240550303. – DOI 10.1002/jcb.240550303

[47] Frost, Harold M.: Tetracycline-based histological analysis of bone remodeling. In: *Calcified Tissue Research* 3 (1969), dec, Nr. 1, 211–237. http://dx.doi.org/10.1007/BF02058664. – DOI 10.1007/BF02058664

[48] Hattner, R. ; Epker, B. N. ; Frost, H. M.: Suggested Sequential Mode of Control of Changes in Cell Behaviour in Adult Bone Remodelling. In: *Nature* 206 (1965), may, Nr. 4983, 489–490. http://dx.doi.org/10.1038/206489a0. – DOI 10.1038/206489a0

[49] Frost, H. M.: Skeletal structural adaptations to mechanical usage (SATMU): 3. The hyaline cartilage modeling problem. In: *The Anatomical Record* 226 (1990), apr, Nr. 4, 423–432. http://dx.doi.org/10.1002/ar.1092260404. – DOI 10.1002/ar.1092260404

[50] Cao, Xu ; Chen, Di: The BMP signaling and in vivo bone formation. In: *Gene* 357 (2005), aug, Nr. 1, 1–8. http://dx.doi.org/10.1016/j.gene.2005.06.017. – DOI 10.1016/j.gene.2005.06.017

[51] Day, Timothy F. ; Guo, Xizhi ; Garrett-Beal, Lisa ; Yang, Yingzi: Wnt/β-Catenin Signaling in Mesenchymal Progenitors Controls Osteoblast and Chondrocyte Differentiation during Vertebrate Skeletogenesis. In: *Developmental Cell* 8 (2005), may, Nr. 5, 739–750. http://dx.doi.org/10.1016/j.devcel.2005.03.016. – DOI 10.1016/j.devcel.2005.03.016

[52] Glass, Donald A. ; Bialek, Peter ; Ahn, Jong D. ; Starbuck, Michael ; Patel, Millan S. ; Clevers, Hans ; Taketo, Mark M. ; Long, Fanxin ; McMahon, Andrew P. ; Lang, Richard A. ; Karsenty, Gerard: Canonical Wnt Signaling in Differentiated Osteoblasts Controls Osteoclast Differentiation. In: *Developmental Cell* 8 (2005), may, Nr. 5, 751–764. http://dx.doi.org/10.1016/j.devcel.2005.02.017. – DOI 10.1016/j.devcel.2005.02.017

[53] Crockett, J. C. ; Mellis, D. J. ; Scott, D. I. ; Helfrich, M. H.: New knowledge on critical osteoclast formation and activation pathways from study of rare genetic diseases of osteoclasts: focus on the RANK/RANKL axis. In: *Osteoporosis International* 22 (2011), jan, Nr. 1, 1–20. http://dx.doi.org/10.1007/s00198-010-1272-8. – DOI 10.1007/s00198–010–1272–8

[54] Kobayashi, S. ; Takahashi, H.E ; Ito, A. ; Saito, N. ; Nawata, M. ; Horiuchi, H. ; Ohta, H. ; Ito, A. ; Iorio, R. ; Yamamoto, N. ; Takaoka, K.: Trabecular minimodeling in human

iliac bone. In: *Bone* 32 (2003), feb, Nr. 2, 163–169. http://dx.doi.org/10.1016/S8756-3282(02)00947-X. – DOI 10.1016/S8756–3282(02)00947–X

[55] Yajima, Aiji ; Inaba, Masaaki ; Tominaga, Yoshihiro ; Ito, Akemi: Bone formation by minimodeling is more active than remodeling after parathyroidectomy. In: *Kidney International* 74 (2008), sep, Nr. 6, 775–781. http://dx.doi.org/10.1038/ki.2008.242. – DOI 10.1038/ki.2008.242

[56] Saito, Hitoshi ; Takeda, Satoshi ; Amizuka, Norio: Eldecalcitol and calcitriol stimulates 'bone minimodeling,' focal bone formation without prior bone resorption, in rat trabecular bone. In: *The Journal of Steroid Biochemistry and Molecular Biology* 136 (2013), jul, Nr. 1, 178–182. http://dx.doi.org/10.1016/j.jsbmb.2012.10.004. – DOI 10.1016/j.jsbmb.2012.10.004

[57] Parfitt, A. M. ; Drezner, Marc K. ; Glorieux, Francis H. ; Kanis, John A. ; Malluche, Hartmut ; Meunier, Pierre J. ; Ott, Susan M. ; Recker, Robert R.: Bone histomorphometry: Standardization of nomenclature, symbols, and units: Report of the asbmr histomorphometry nomenclature committee. In: *Journal of Bone and Mineral Research* 2 (1987), dec, Nr. 6, 595–610. http://dx.doi.org/10.1002/jbmr.5650020617. – DOI 10.1002/jbmr.5650020617

[58] Orhan, Kaan ; Orhan, Kaan (Hrsg.): *Micro-computed Tomography (micro-CT) in Medicine and Engineering*. Cham : Springer International Publishing, 2020. http://dx.doi.org/10.1007/978-3-030-16641-0. http://dx.doi.org/10.1007/978-3-030-16641-0. – ISBN 978–3–030–16640–3

[59] De Souza, Roberto L. ; Matsuura, Maiko ; Eckstein, Felix ; Rawlinson, Simon C. ; Lanyon, Lance E. ; Pitsillides, Andrew A.: Non-invasive axial loading of mouse tibiae increases cortical bone formation and modifies trabecular organization: A new model to study cortical and cancellous compartments in a single loaded element. In: *Bone* 37 (2005), dec, Nr. 6, 810–818. http://dx.doi.org/10.1016/j.bone.2005.07.022. – DOI 10.1016/j.bone.2005.07.022

[60] Fritton, J. ; Myers, E. ; Wright, T. ; Vandermeulen, M.: Loading induces site-specific increases in mineral content assessed by microcomputed tomography of the mouse tibia. In: *Bone* 36 (2005), jun, Nr. 6, 1030–1038. http://dx.doi.org/10.1016/j.bone.2005.02.013. – DOI 10.1016/j.bone.2005.02.013

[61] Boerckel, Joel D. ; Mason, Devon E. ; McDermott, Anna M. ; Alsberg, Eben: Micro-

computed tomography: approaches and applications in bioengineering. In: *Stem Cell Research and Therapy* 5 (2014), Nr. 6, 144. http://dx.doi.org/10.1186/scrt534. – DOI 10.1186/scrt534

[62] Cipitria, Amaia ; Boettcher, Kathrin ; Schoenhals, Sophia ; Garske, Daniela S. ; Schmidt-Bleek, Katharina ; Ellinghaus, Agnes ; Dienelt, Anke ; Peters, Anja ; Mehta, Manav ; Madl, Christopher M. ; Huebsch, Nathaniel ; Mooney, David J. ; Duda, Georg N.: In-situ tissue regeneration through SDF-1α driven cell recruitment and stiffness-mediated bone regeneration in a critical-sized segmental femoral defect. In: *Acta Biomaterialia* 60 (2017), 50–63. http://dx.doi.org/10.1016/j.actbio.2017.07.032. – DOI 10.1016/j.actbio.2017.07.032

[63] Reichert, Johannes C. ; Cipitria, Amaia ; Epari, Devakara R. ; Saifzadeh, Siamak ; Krishnakanth, Pushpanjali ; Berner, Arne ; Woodruff, Maria A. ; Schell, Hanna ; Mehta, Manav ; Schuetz, Michael A. ; Duda, Georg N. ; Hutmacher, Dietmar W.: A Tissue Engineering Solution for Segmental Defect Regeneration in Load-Bearing Long Bones. In: *Science Translational Medicine* 4 (2012), jul, Nr. 141, 141ra93–141ra93. http://dx.doi.org/10.1126/scitranslmed.3003720. – DOI 10.1126/scitranslmed.3003720

[64] Willie, Bettina M. ; Birkhold, Annette I. ; Razi, Hajar ; Thiele, Tobias ; Aido, Marta ; Kruck, Bettina ; Schill, Alexander ; Checa, Sara ; Main, Russell P. ; Duda, Georg N.: Diminished response to in vivo mechanical loading in trabecular and not cortical bone in adulthood of female C57Bl/6 mice coincides with a reduction in deformation to load. In: *Bone* 55 (2013), aug, Nr. 2, 335–346. http://dx.doi.org/10.1016/j.bone.2013.04.023. – DOI 10.1016/j.bone.2013.04.023

[65] Waarsing, J.H. ; Day, J.S. ; Linden, J.C. van d. ; Ederveen, A.G. ; Spanjers, C. ; De Clerck, N. ; Sasov, A. ; Verhaar, J.A.N. ; Weinans, H.: Detecting and tracking local changes in the tibiae of individual rats: a novel method to analyse longitudinal in vivo micro-CT data. In: *Bone* 34 (2004), jan, Nr. 1, 163–169. http://dx.doi.org/10.1016/j.bone.2003.08.012. – DOI 10.1016/j.bone.2003.08.012

[66] Birkhold, Annette I. ; Razi, Hajar ; Duda, Georg N. ; Weinkamer, Richard ; Checa, Sara ; Willie, Bettina M.: Mineralizing surface is the main target of mechanical stimulation independent of age: 3D dynamic in vivo morphometry. In: *Bone* 66 (2014), sep, 15–25. http://dx.doi.org/10.1016/j.bone.2014.05.013. – DOI 10.1016/j.bone.2014.05.013

[67] Schulte, Friederike A. ; Lambers, Floor M. ; Kuhn, Gisela ; Müller, Ralph: In vivo micro-computed tomography allows direct three-dimensional quantification of both bone formation and bone resorption parameters using time-lapsed imaging. In: *Bone* 48 (2011), mar, Nr. 3, 433–442. http://dx.doi.org/10.1016/j.bone.2010.10.007. – DOI 10.1016/j.bone.2010.10.007

[68] Altman, Allison R. ; Tseng, Wei-Ju ; Bakker, Chantal M. ; Chandra, Abhishek ; Lan, Shenghui ; Huh, Beom K. ; Luo, Shiming ; Leonard, Mary B. ; Qin, Ling ; Liu, X. S.: Quantification of skeletal growth, modeling, and remodeling by in vivo micro computed tomography. In: *Bone* 81 (2015), dec, 370–379. http://dx.doi.org/10.1016/j.bone.2015.07.037. – DOI 10.1016/j.bone.2015.07.037

[69] Lu, Yongtao ; Boudiffa, Maya ; Dall'Ara, Enrico ; Bellantuono, Ilaria ; Viceconti, Marco: Evaluation of in-vivo measurement errors associated with micro-computed tomography scans by means of the bone surface distance approach. In: *Medical Engineering and Physics* 37 (2015), nov, Nr. 11, 1091–1097. http://dx.doi.org/10.1016/j.medengphy.2015.08.017. – DOI 10.1016/j.medengphy.2015.08.017

[70] Birkhold, Annette I. ; Razi, Hajar ; Duda, Georg N. ; Weinkamer, Richard ; Checa, Sara ; Willie, Bettina M.: The influence of age on adaptive bone formation and bone resorption. In: *Biomaterials* 35 (2014), nov, Nr. 34, 9290–9301. http://dx.doi.org/10.1016/j.biomaterials.2014.07.051. – DOI 10.1016/j.biomaterials.2014.07.051

[71] Birkhold, Annette I.: *A 4D imaging approach to monitor bone remodeling [dissertation]*, Berlin: Technische Universität Berlin, Diss., 2015

[72] Birkhold, Annette I. ; Razi, Hajar ; Duda, Georg N. ; Weinkamer, Richard ; Checa, Sara ; Willie, Bettina M.: The Periosteal Bone Surface is Less Mechano-Responsive than the Endocortical. In: *Scientific Reports* 6 (2016), sep, Nr. 1, 23480. http://dx.doi.org/10.1038/srep23480. – DOI 10.1038/srep23480

[73] Birkhold, Annette I. ; Razi, Hajar ; Duda, Georg N. ; Checa, Sara ; Willie, Bettina M.: Tomography-Based Quantification of Regional Differences in Cortical Bone Surface Remodeling and Mechano-Response. In: *Calcified Tissue International* 100 (2017), mar, Nr. 3, 255–270. http://dx.doi.org/10.1007/s00223-016-0217-4. – DOI 10.1007/s00223–016–0217–4

[74] Rummler, Maximilian ; Ziouti, Fani ; Bouchard, Alice L. ; Brandl, Andreas ; Duda, Georg N. ; Bogen, Bjarne ; Beilhack, Andreas ; Lynch, Maureen E. ; Jundt, Franziska ; Willie, Bettina M.: Mechanical loading prevents bone destruction and exerts anti-tumor effects in the MOPC315.BM.Luc model of myeloma bone disease. In: *Acta Biomaterialia* 119 (2021), jan, 247–258. http://dx.doi.org/10.1016/j.actbio.2020.10.041. – DOI 10.1016/j.actbio.2020.10.041

[75] Johnson, Lindsay C. ; Johnson, Rachelle W. ; Munoz, Steve A. ; Mundy, Gregory R. ; Peterson, Todd E. ; Sterling, Julie A.: Longitudinal live animal micro-CT allows for quantitative analysis of tumor-induced bone destruction. In: *Bone* 48 (2011), jan, Nr. 1, 141–151. http://dx.doi.org/10.1016/j.bone.2010.05.033. – DOI 10.1016/j.bone.2010.05.033

[76] Torre, Lindsey A. ; Bray, Freddie ; Siegel, Rebecca L. ; Ferlay, Jacques ; Lortet-Tieulent, Joannie ; Jemal, Ahmedin: Global cancer statistics, 2012. In: *CA: A Cancer Journal for Clinicians* 65 (2015), mar, Nr. 2, 87–108. http://dx.doi.org/10.3322/caac.21262. – DOI 10.3322/caac.21262

[77] Coleman, Robert E.: Clinical Features of Metastatic Bone Disease and Risk of Skeletal Morbidity. In: *Clinical Cancer Research* 12 (2006), oct, Nr. 20, 6243s–6249s. http://dx.doi.org/10.1158/1078-0432.CCR-06-0931. – DOI 10.1158/1078–0432.CCR–06–0931

[78] Harbeck, Nadia ; Penault-Llorca, Frédérique ; Cortes, Javier ; Gnant, Michael ; Houssami, Nehmat ; Poortmans, Philip ; Ruddy, Kathryn ; Tsang, Janice ; Cardoso, Fatima: Breast cancer. In: *Nature Reviews Disease Primers* 5 (2019), dec, Nr. 1, 66. http://dx.doi.org/10.1038/s41572-019-0111-2. – DOI 10.1038/s41572–019–0111–2

[79] Perou, Charles M. ; Sørlie, Therese ; Eisen, Michael B. ; Rijn, Matt van d. ; Jeffrey, Stefanie S. ; Rees, Christian A. ; Pollack, Jonathan R. ; Ross, Douglas T. ; Johnsen, Hilde ; Akslen, Lars A. ; Fluge, Øystein ; Pergamenschikov, Alexander ; Williams, Cheryl ; Zhu, Shirley X. ; Lønning, Per E. ; Børresen-Dale, Anne-Lise ; Brown, Patrick O. ; Botstein, David: Molecular portraits of human breast tumours. In: *Nature* 406 (2000), aug, Nr. 6797, 747–752. http://dx.doi.org/10.1038/35021093. – DOI 10.1038/35021093

[80] Holliday, Deborah L. ; Speirs, Valerie: Choosing the right cell line for breast cancer research.

In: *Breast Cancer Research* 13 (2011), aug, Nr. 4, 215. http://dx.doi.org/10.1186/bcr2889. – DOI 10.1186/bcr2889

[81] Minn, Andy J. ; Gupta, Gaorav P. ; Siegel, Peter M. ; Bos, Paula D. ; Shu, Weiping ; Giri, Dilip D. ; Viale, Agnes ; Olshen, Adam B. ; Gerald, William L. ; Massagué, Joan: Genes that mediate breast cancer metastasis to lung. In: *Nature* 436 (2005), jul, Nr. 7050, 518–524. http://dx.doi.org/10.1038/nature03799. – DOI 10.1038/nature03799

[82] Simmons, J. K. ; Hildreth, B. E. ; Supsavhad, W. ; Elshafae, S. M. ; Hassan, B. B. ; Dirksen, W. P. ; Toribio, R. E. ; Rosol, T. J.: Animal Models of Bone Metastasis. In: *Veterinary Pathology* 52 (2015), sep, Nr. 5, 827–841. http://dx.doi.org/10.1177/0300985815586223. – DOI 10.1177/0300985815586223

[83] Wright, Laura E. ; Ottewell, Penelope D. ; Rucci, Nadia ; Peyruchaud, Olivier ; Pagnotti, Gabriel M. ; Chiechi, Antonella ; Buijs, Jeroen T. ; Sterling, Julie A.: Murine models of breast cancer bone metastasis. In: *BoneKEy Reports* 5 (2016), may, Nr. April, 309–330. http://dx.doi.org/10.1038/bonekey.2016.31. – DOI 10.1038/bonekey.2016.31

[84] Han, Yuxuan ; Nakayama, Jun ; Hayashi, Yusuke ; Jeong, Seongmoon ; Futakuchi, Mitsuru ; Ito, Emi ; Watanabe, Shinya ; Semba, Kentaro: Establishment and characterization of highly osteolytic luminal breast cancer cell lines by intracaudal arterial injection. In: *Genes to Cells* 25 (2020), feb, Nr. 2, 111–123. http://dx.doi.org/10.1111/gtc.12743. – DOI 10.1111/gtc.12743

[85] Coleman, Robert E. ; Croucher, Peter I. ; Padhani, Anwar R. ; Clézardin, Philippe ; Chow, Edward ; Fallon, Marie ; Guise, Theresa ; Colangeli, Simone ; Capanna, Rodolfo ; Costa, Luis: Bone metastases. In: *Nature Reviews Disease Primers* 6 (2020), dec, Nr. 1, 83. http://dx.doi.org/10.1038/s41572-020-00216-3. – DOI 10.1038/s41572–020–00216–3

[86] Kaplan, Rosandra N. ; Riba, Rebecca D. ; Zacharoulis, Stergios ; Bramley, Anna H. ; Vincent, Loïc ; Costa, Carla ; MacDonald, Daniel D. ; Jin, David K. ; Shido, Koji ; Kerns, Scott A. ; Zhu, Zhenping ; Hicklin, Daniel ; Wu, Yan ; Port, Jeffrey L. ; Altorki, Nasser ; Port, Elisa R. ; Ruggero, Davide ; Shmelkov, Sergey V. ; Jensen, Kristian K. ; Rafii, Shahin ; Lyden, David: VEGFR1-positive haematopoietic bone marrow progenitors initiate the pre-metastatic niche. In: *Nature* 438 (2005), Nr. 7069, S. 820–827. http://dx.doi.org/10.1038/nature04186. – DOI 10.1038/nature04186

[87] Psaila, Bethan ; Lyden, David: The metastatic niche: adapting the foreign soil. In: *Nature Reviews Cancer* 9 (2009), apr, Nr. 4, 285–293. http://dx.doi.org/10.1038/nrc2621. – DOI 10.1038/nrc2621

[88] Peinado, Héctor ; Zhang, Haiying ; Matei, Irina R. ; Costa-Silva, Bruno ; Hoshino, Ayuko ; Rodrigues, Goncalo ; Psaila, Bethan ; Kaplan, Rosandra N. ; Bromberg, Jacqueline F. ; Kang, Yibin ; Bissell, Mina J. ; Cox, Thomas R. ; Giaccia, Amato J. ; Erler, Janine T. ; Hiratsuka, Sachie ; Ghajar, Cyrus M. ; Lyden, David: Pre-metastatic niches: organ-specific homes for metastases. In: *Nature Reviews Cancer* 17 (2017), may, Nr. 5, 302–317. http://dx.doi.org/10.1038/nrc.2017.6. – DOI 10.1038/nrc.2017.6

[89] Cox, Thomas R. ; Bird, Demelza ; Baker, Ann-Marie ; Barker, Holly E. ; Ho, Melisa W. ; Lang, Georgina ; Erler, Janine T.: LOX-Mediated Collagen Crosslinking Is Responsible for Fibrosis-Enhanced Metastasis. In: *Cancer Research* 73 (2013), mar, Nr. 6, 1721–1732. http://dx.doi.org/10.1158/0008-5472.CAN-12-2233. – DOI 10.1158/0008–5472.CAN–12–2233

[90] Weilbaecher, Katherine N. ; Guise, Theresa A. ; McCauley, Laurie K.: Cancer to bone: a fatal attraction. In: *Nature Reviews Cancer* 11 (2011), jun, Nr. 6, 411–425. http://dx.doi.org/10.1038/nrc3055. – DOI 10.1038/nrc3055

[91] Chiou, Aaron E. ; Liu, Chuang ; Moreno-Jiménez, Inés ; Tang, Tengteng ; Wagermaier, Wolfgang ; Dean, Mason N. ; Fischbach, Claudia ; Fratzl, Peter: Breast cancer–secreted factors perturb murine bone growth in regions prone to metastasis. In: *Science Advances* 7 (2021), Nr. 12, S. 1–14. http://dx.doi.org/10.1126/sciadv.abf2283. – DOI 10.1126/sciadv.abf2283

[92] Karrison, Theodore G. ; Ferguson, Donald J. ; Meier, Paul: Dormancy of Mammary Carcinoma After Mastectomy. In: *JNCI Journal of the National Cancer Institute* 91 (1999), jan, Nr. 1, 80–85. http://dx.doi.org/10.1093/jnci/91.1.80. – DOI 10.1093/jnci/91.1.80

[93] Aguirre-Ghiso, Julio A.: Models, mechanisms and clinical evidence for cancer dormancy. In: *Nature Reviews Cancer* 7 (2007), nov, Nr. 11, 834–846. http://dx.doi.org/10.1038/nrc2256. – DOI 10.1038/nrc2256

[94] Sosa, María S. ; Bragado, Paloma ; Aguirre-Ghiso, Julio A.: Mechanisms of disseminated

cancer cell dormancy: an awakening field. In: *Nature Reviews Cancer* 14 (2014), sep, Nr. 9, 611–622. http://dx.doi.org/10.1038/nrc3793. – DOI 10.1038/nrc3793

[95] Dhawan, Abhishek ; Friedrichs, Jens ; Bonin, Malte von ; Bejestani, Elham P. ; Werner, Carsten ; Wobus, Manja ; Chavakis, Triantafyllos ; Bornhäuser, Martin: Breast cancer cells compete with hematopoietic stem and progenitor cells for intercellular adhesion molecule 1-mediated binding to the bone marrow microenvironment. In: *Carcinogenesis* 37 (2016), aug, Nr. 8, 759–767. http://dx.doi.org/10.1093/carcin/bgw057. – DOI 10.1093/carcin/bgw057

[96] Carlson, Patrick ; Dasgupta, Arko ; Grzelak, Candice A. ; Kim, Jeanna ; Barrett, Alexander ; Coleman, Ilsa M. ; Shor, Ryann E. ; Goddard, Erica T. ; Dai, Jinxiang ; Schweitzer, Emma M. ; Lim, Andrea R. ; Crist, Sarah B. ; Cheresh, David A. ; Nelson, Peter S. ; Hansen, Kirk C. ; Ghajar, Cyrus M.: Targeting the perivascular niche sensitizes disseminated tumour cells to chemotherapy. In: *Nature Cell Biology* 21 (2019), feb, Nr. 2, 238–250. http://dx.doi.org/10.1038/s41556-018-0267-0. – DOI 10.1038/s41556–018–0267–0

[97] Ghajar, Cyrus M. ; Peinado, Héctor ; Mori, Hidetoshi ; Matei, Irina R. ; Evason, Kimberley J. ; Brazier, Hélène ; Almeida, Dena ; Koller, Antonius ; Hajjar, Katherine A. ; Stainier, Didier Y R. ; Chen, Emily I. ; Lyden, David ; Bissell, Mina J.: The perivascular niche regulates breast tumour dormancy. In: *Nature Cell Biology* 15 (2013), jul, Nr. 7, 807–817. http://dx.doi.org/10.1038/ncb2767. – DOI 10.1038/ncb2767

[98] McCoy, Erin M. ; Hong, Huixian ; Pruitt, Hawley C. ; Feng, Xu: IL-11 produced by breast cancer cells augments osteoclastogenesis by sustaining the pool of osteoclast progenitor cells. In: *BMC Cancer* 13 (2013), dec, Nr. 1, 16. http://dx.doi.org/10.1186/1471-2407-13-16. – DOI 10.1186/1471–2407–13–16

[99] Thomas, Rachel J. ; Guise, Theresa A. ; Yin, Juan J. ; Elliott, Jan ; Horwood, Nicole J. ; Martin, T. J. ; Gillespie, Matthew T.: Breast Cancer Cells Interact with Osteoblasts to Support Osteoclast Formation 1. In: *Endocrinology* 140 (1999), oct, Nr. 10, 4451–4458. http://dx.doi.org/10.1210/endo.140.10.7037. – DOI 10.1210/endo.140.10.7037

[100] Mundy, Gregory R.: Mechanisms of bone metastasis. In: *Cancer* 80 (1997), 1546–1556. https://acsjournals.onlinelibrary.wiley.com/doi/full/10.1002/(SICI)1097-0142(19971015)80:8+%3C1546::AID-CNCR4%3E3.0.CO%3B2-I

[101] EILON, GABRIEL ; MUNDY, GREGORY R.: Direct resorption of bone by human breast cancer cells in vitro. In: *Nature* 276 (1978), dec, Nr. 5689, 726–728. http://dx.doi.org/10.1038/276726a0. – DOI 10.1038/276726a0

[102] Wang, Ning ; Reeves, Kimberley J. ; Brown, Hannah K. ; Fowles, Anne C M. ; Docherty, Freyja E. ; Ottewell, Penelope D. ; Croucher, Peter I. ; Holen, Ingunn ; Eaton, Colby L.: The frequency of osteolytic bone metastasis is determined by conditions of the soil, not the number of seeds; evidence from in vivo models of breast and prostate cancer. In: *Journal of Experimental and Clinical Cancer Research* 34 (2015), dec, Nr. 1, 124. http://dx.doi.org/10.1186/s13046-015-0240-8. – DOI 10.1186/s13046–015–0240–8

[103] He, Frank ; Chiou, Aaron E. ; Loh, Hyun C. ; Lynch, Maureen ; Seo, Bo R. ; Song, Young H. ; Lee, Min J. ; Hoerth, Rebecca ; Bortel, Emely L. ; Willie, Bettina M. ; Duda, Georg N. ; Estroff, Lara A. ; Masic, Admir ; Wagermaier, Wolfgang ; Fratzl, Peter ; Fischbach, Claudia: Multiscale characterization of the mineral phase at skeletal sites of breast cancer metastasis. In: *Proceedings of the National Academy of Sciences* 114 (2017), oct, Nr. 40, 10542–10547. http://dx.doi.org/10.1073/pnas.1708161114. – DOI 10.1073/pnas.1708161114

[104] Ponomarev, Vladimir ; Doubrovin, Michael ; Serganova, Inna ; Vider, Jelena ; Shavrin, Aleksander ; Beresten, Tatiana ; Ivanova, Anna ; Ageyeva, Ludmila ; Tourkova, Vilia ; Balatoni, Julius ; Bornmann, William ; Blasberg, Ronald ; Tjuvajev, Juri G.: A novel triple-modality reporter gene for whole-body fluorescent, bioluminescent, and nuclear noninvasive imaging. In: *European Journal of Nuclear Medicine and Molecular Imaging* 31 (2004), Nr. 5, S. 740–751. http://dx.doi.org/10.1007/s00259-003-1441-5. – DOI 10.1007/s00259–003–1441–5

[105] Young, Sarah A. ; Rummler, Maximilian ; Taïeb, Hubert M. ; Garske, Daniela S. ; Ellinghaus, Agnes ; Duda, Georg N. ; Willie, Bettina M. ; Cipitria, Amaia: In vivo microCT-based time-lapse morphometry reveals anatomical site-specific differences in bone (re)modeling serving as baseline parameters to detect early pathological events. In: *Bone* 161 (2022), aug, Nr. February, 116432. http://dx.doi.org/10.1016/j.bone.2022.116432. – DOI 10.1016/j.bone.2022.116432

[106] Otsu, Nobuyuki: A Threshold Selection Method from Gray-Level Histograms. In: *IEEE Transactions on Systems, Man, and Cybernetics* 9 (1979), jan, Nr. 1, 62–66. http://dx.doi.org/10.1109/TSMC.1979.4310076. – DOI 10.1109/TSMC.1979.4310076

[107] Nishiyama, Kyle K. ; Campbell, Graeme M. ; Klinck, Robert J. ; Boyd, Steven K.: Reproducibility of bone micro-architecture measurements in rodents by in vivo micro-computed tomography is maximized with three-dimensional image registration. In: *Bone* 46 (2010), jan, Nr. 1, 155–161. http://dx.doi.org/10.1016/j.bone.2009.09.023. – DOI 10.1016/j.bone.2009.09.023

[108] Glüer, C. C. ; Blake, G. ; Lu, Y. ; Blunt, B. A. ; Jergas, M. ; Genant, H. K.: Accurate assessment of precision errors: How to measure the reproducibility of bone densitometry techniques. In: *Osteoporosis International* 5 (1995), jul, Nr. 4, 262–270. http://dx.doi.org/10.1007/BF01774016. – DOI 10.1007/BF01774016

[109] Moreno-Jiménez, I. ; Garske, D.S. ; Lahr, C.A. ; Hutmacher, D.W. ; Cipitria, A.: Targeted 2D histology and ultrastructural bone analysis based on 3D microCT anatomical locations. In: *MethodsX* 8 (2021), 101480. http://dx.doi.org/10.1016/j.mex.2021.101480. – DOI 10.1016/j.mex.2021.101480

[110] Cole, Heather A. ; Yuasa, Masato ; Hawley, Gregory ; Cates, Justin M. ; Nyman, Jeffry S. ; Schoenecker, Jonathan G.: Differential development of the distal and proximal femoral epiphysis and physis in mice. In: *Bone* 52 (2013), jan, Nr. 1, 337–346. http://dx.doi.org/10.1016/j.bone.2012.10.011. – DOI 10.1016/j.bone.2012.10.011

[111] Vanderoost, Jef: From histology to micro-CT: Measuring and modeling resorption cavities and their relation to bone competence. In: *World Journal of Radiology* 6 (2014), Nr. 9, 643. http://dx.doi.org/10.4329/wjr.v6.i9.643. – DOI 10.4329/wjr.v6.i9.643

[112] Allocca, Gloria ; Hughes, Russell ; Wang, Ning ; Brown, Hannah K. ; Ottewell, Penelope D. ; Brown, Nicola J. ; Holen, Ingunn: The bone metastasis niche in breast cancer: potential overlap with the haematopoietic stem cell niche in vivo. In: *Journal of Bone Oncology* 17 (2019), aug, Nr. February, 100244. http://dx.doi.org/10.1016/j.jbo.2019.100244. – DOI 10.1016/j.jbo.2019.100244

[113] Butterfield, Natalie C. ; Curry, Katherine F. ; Steinberg, Julia ; Dewhurst, Hannah ; Komla-Ebri, Davide ; Mannan, Naila S. ; Adoum, Anne T. ; Leitch, Victoria D. ; Logan, John G. ; Waung, Julian A. ; Ghirardello, Elena ; Southam, Lorraine ; Youlten, Scott E. ; Wilkinson, J. M. ; McAninch, Elizabeth A. ; Vancollie, Valerie E. ; Kussy, Fiona ; White, Jacqueline K. ; Lelliott, Christopher J. ; Adams, David J. ; Jacques, Richard ;

Bianco, Antonio C. ; Boyde, Alan ; Zeggini, Eleftheria ; Croucher, Peter I. ; Williams, Graham R. ; Bassett, J. H.: Accelerating functional gene discovery in osteoarthritis. In: *Nature Communications* 12 (2021), Nr. 1, S. 1–18. http://dx.doi.org/10.1038/s41467-020-20761-5. – DOI 10.1038/s41467–020–20761–5

[114] Prasad, Jitendra ; Wiater, Brett P. ; Nork, Sean E. ; Bain, Steven D. ; Gross, Ted S.: Characterizing gait induced normal strains in a murine tibia cortical bone defect model. In: *Journal of Biomechanics* 43 (2010), oct, Nr. 14, 2765–2770. http://dx.doi.org/10.1016/j.jbiomech.2010.06.030. – DOI 10.1016/j.jbiomech.2010.06.030

[115] Zumwalt, Ann C. ; Hamrick, Mark ; Schmitt, Daniel: Force plate for measuring the ground reaction forces in small animal locomotion. In: *Journal of Biomechanics* 39 (2006), jan, Nr. 15, 2877–2881. http://dx.doi.org/10.1016/j.jbiomech.2005.10.006. – DOI 10.1016/j.jbiomech.2005.10.006

[116] Schmitt, Daniel ; Zumwalt, Ann C. ; Hamrick, Mark W.: The relationship between bone mechanical properties and ground reaction forces in normal and hypermuscular mice. In: *Journal of Experimental Zoology Part A: Ecological Genetics and Physiology* 313A (2010), apr, Nr. 6, 339–351. http://dx.doi.org/10.1002/jez.604. – DOI 10.1002/jez.604

[117] Main, Russell P. ; Shefelbine, Sandra J. ; Meakin, Lee B. ; Silva, Matthew J. ; Meulen, Marjolein C. H. ; Willie, Bettina M.: Murine Axial Compression Tibial Loading Model to Study Bone Mechanobiology: Implementing the Model and Reporting Results. In: *Journal of Orthopaedic Research* 38 (2020), feb, Nr. 2, 233–252. http://dx.doi.org/10.1002/jor.24466. – DOI 10.1002/jor.24466

[118] Kolb, Alexus D. ; Shupp, Alison B. ; Mukhopadhyay, Dimpi ; Marini, Frank C. ; Bussard, Karen M.: Osteoblasts are “educated” by crosstalk with metastatic breast cancer cells in the bone tumor microenvironment. In: *Breast Cancer Research* 21 (2019), dec, Nr. 1, 31. http://dx.doi.org/10.1186/s13058-019-1117-0. – DOI 10.1186/s13058–019–1117–0

[119] Brown, H. K. ; Ottewell, P. D. ; Evans, C. A. ; Holen, I.: Location matters: osteoblast and osteoclast distribution is modified by the presence and proximity to breast cancer cells in vivo. In: *Clinical and Experimental Metastasis* 29 (2012), dec, Nr. 8, 927–938. http://dx.doi.org/10.1007/s10585-012-9481-5. – DOI 10.1007/s10585–012–9481–5

[120] Zarrer, Jennifer ; Haider, Marie-therese ; Smit, Daniel J. ; Taipaleenmäki, Hanna: Pathological Crosstalk between Metastatic Breast Cancer Cells and the Bone Microenvironment. In: *Biomolecules* 10 (2020), feb, Nr. 2, 337. http://dx.doi.org/10.3390/biom10020337. – DOI 10.3390/biom10020337

[121] Wang, Ning ; Docherty, Freyja E. ; Brown, Hannah K. ; Reeves, Kimberley J. ; Fowles, Anne C. ; Ottewell, Penelope D. ; Dear, T. N. ; Holen, Ingunn ; Croucher, Peter I. ; Eaton, Colby L.: Prostate Cancer Cells Preferentially Home to Osteoblast-rich Areas in the Early Stages of Bone Metastasis: Evidence From In Vivo Models. In: *Journal of Bone and Mineral Research* 29 (2014), dec, Nr. 12, 2688–2696. http://dx.doi.org/10.1002/jbmr.2300. – DOI 10.1002/jbmr.2300

[122] Campbell, Graeme M. ; Tower, Robert J. ; Damm, Timo ; Kneissl, Philipp ; Rambow, Anna C. ; Schem, Christian ; Tiwari, Sanjay ; Glüer, Claus C.: Tracking the Progression of Osteolytic and Osteosclerotic Lesions in Mice Using Serial In Vivo μCT: Applications to the Assessment of Bisphosphonate Treatment Efficacy. In: *Journal of Bone and Mineral Research* 33 (2018), mar, Nr. 3, 410–418. http://dx.doi.org/10.1002/jbmr.3317. – DOI 10.1002/jbmr.3317

[123] Yin, Juan J. ; Pollock, Claire B. ; Kelly, Kathleen: Mechanisms of cancer metastasis to the bone. In: *Cell Research* 15 (2005), jan, Nr. 1, 57–62. http://dx.doi.org/10.1038/sj.cr.7290266. – DOI 10.1038/sj.cr.7290266

[124] Tonna, E. A.: Periosteal Osteoclasts, Skeletal Development and Ageing. In: *Nature* 185 (1960), feb, Nr. 4710, 405–407. http://dx.doi.org/10.1038/185405a0. – DOI 10.1038/185405a0

[125] Wang, Hai ; Yu, Cuijuan ; Gao, Xia ; Welte, Thomas ; Muscarella, Aaron M. ; Tian, Lin ; Zhao, Hong ; Zhao, Zhen ; Du, Shiyu ; Tao, Jianning ; Lee, Brendan ; Westbrook, Thomas F. ; Wong, Stephen T. ; Jin, Xin ; Rosen, Jeffrey M. ; Osborne, C. K. ; Zhang, Xiang H.-F.: The Osteogenic Niche Promotes Early-Stage Bone Colonization of Disseminated Breast Cancer Cells. In: *Cancer Cell* 27 (2015), feb, Nr. 2, 193–210. http://dx.doi.org/10.1016/j.ccell.2014.11.017. – DOI 10.1016/j.ccell.2014.11.017

[126] Phadke, Pushkar A. ; Mercer, Robyn R. ; Harms, John F. ; Jia, Yujiang ; Frost, Andra R. ; Jewell, Jennifer L. ; Bussard, Karen M. ; Nelson, Shakira ; Moore, Cynthia ; Kappes, John C. ; Gay, Carol V. ; Mastro, Andrea M. ; Welch, Danny R.: Kinetics of Metastatic

Breast Cancer Cell Trafficking in Bone. In: *Clinical Cancer Research* 12 (2006), mar, Nr. 5, 1431–1440. http://dx.doi.org/10.1158/1078-0432.CCR-05-1806. – DOI 10.1158/1078–0432.CCR–05–1806

[127] Christiansen, Blaine A.: Effect of micro-computed tomography voxel size and segmentation method on trabecular bone microstructure measures in mice. In: *Bone Reports* 5 (2016), dec, 136–140. http://dx.doi.org/10.1016/j.bonr.2016.05.006. – DOI 10.1016/j.bonr.2016.05.006

[128] Crist, Sarah B. ; Ghajar, Cyrus M.: When a House Is Not a Home: A Survey of Antimetastatic Niches and Potential Mechanisms of Disseminated Tumor Cell Suppression. In: *Annual Review of Pathology: Mechanisms of Disease* 16 (2021), jan, Nr. 1, 409–432. http://dx.doi.org/10.1146/annurev-pathmechdis-012419-032647. – DOI 10.1146/annurev–pathmechdis–012419–032647

[129] Aceto, Nicola ; Bardia, Aditya ; Miyamoto, David T. ; Donaldson, Maria C. ; Wittner, Ben S. ; Spencer, Joel A. ; Yu, Min ; Pely, Adam ; Engstrom, Amanda ; Zhu, Huili ; Brannigan, Brian W. ; Kapur, Ravi ; Stott, Shannon L. ; Shioda, Toshi ; Ramaswamy, Sridhar ; Ting, David T. ; Lin, Charles P. ; Toner, Mehmet ; Haber, Daniel A. ; Maheswaran, Shyamala: Circulating Tumor Cell Clusters Are Oligoclonal Precursors of Breast Cancer Metastasis. In: *Cell* 158 (2014), aug, Nr. 5, 1110–1122. http://dx.doi.org/10.1016/j.cell.2014.07.013. – DOI 10.1016/j.cell.2014.07.013

[130] Miller, Iain ; Min, Mingwei ; Yang, Chen ; Tian, Chengzhe ; Gookin, Sara ; Carter, Dylan ; Spencer, Sabrina L.: Ki67 is a Graded Rather than a Binary Marker of Proliferation versus Quiescence. In: *Cell Reports* 24 (2018), jul, Nr. 5, 1105–1112.e5. http://dx.doi.org/10.1016/j.celrep.2018.06.110. – DOI 10.1016/j.celrep.2018.06.110

[131] Astrof, Sophie ; Hynes, Richard O.: Fibronectins in vascular morphogenesis. In: *Angiogenesis* 12 (2009), jun, Nr. 2, 165–175. http://dx.doi.org/10.1007/s10456-009-9136-6. – DOI 10.1007/s10456–009–9136–6

[132] Di Martino, Julie S. ; Nobre, Ana R. ; Mondal, Chandrani ; Taha, Isra ; Farias, Eduardo F. ; Fertig, Elana J. ; Naba, Alexandra ; Aguirre-Ghiso, Julio A. ; Bravo-Cordero, Jose J.: A tumor-derived type III collagen-rich ECM niche regulates tumor cell dormancy. In: *Nature Cancer 2021* (2021), dec, 1–18. http://dx.doi.org/10.1038/s43018-021-00291-9. – DOI 10.1038/s43018–021–00291–9

[133] Wang, Karin ; Wu, Fei ; Seo, Bo R. ; Fischbach, Claudia ; Chen, Weisi ; Hsu, Lauren ; Gourdon, Delphine: Breast cancer cells alter the dynamics of stromal fibronectin-collagen interactions. In: *Matrix Biology* 60-61 (2017), jul, 86–95. http://dx.doi.org/10.1016/j.matbio.2016.08.001. – DOI 10.1016/j.matbio.2016.08.001

[134] Halder, Georg ; Dupont, Sirio ; Piccolo, Stefano: Transduction of mechanical and cytoskeletal cues by YAP and TAZ. In: *Nature Reviews Molecular Cell Biology* 13 (2012), sep, Nr. 9, 591–600. http://dx.doi.org/10.1038/nrm3416. – DOI 10.1038/nrm3416

Appendices

APPENDIX A

Experimental setup

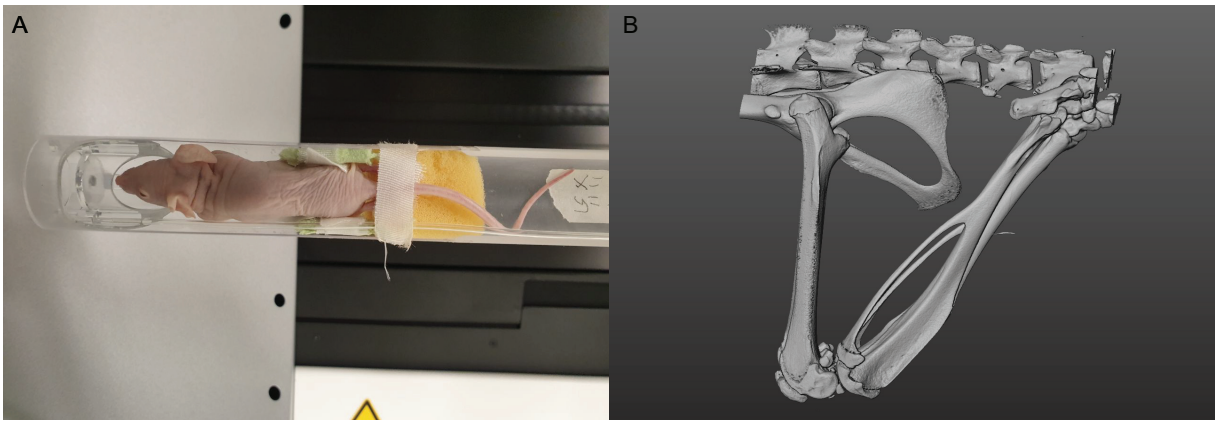

Fig. A.1: **Experimental setup and entire region scanned.** (A) Mouse placed on the animal bed for the microCT scan with the hind limbs restrained and (B) exemplary field of view for one entire scan including the entire femur and tibia of both hind limbs.[105]

APPENDIX B

Dynamic microcomputed tomography-based time-lapse morphometry

B.1 Influence of different threshold methods

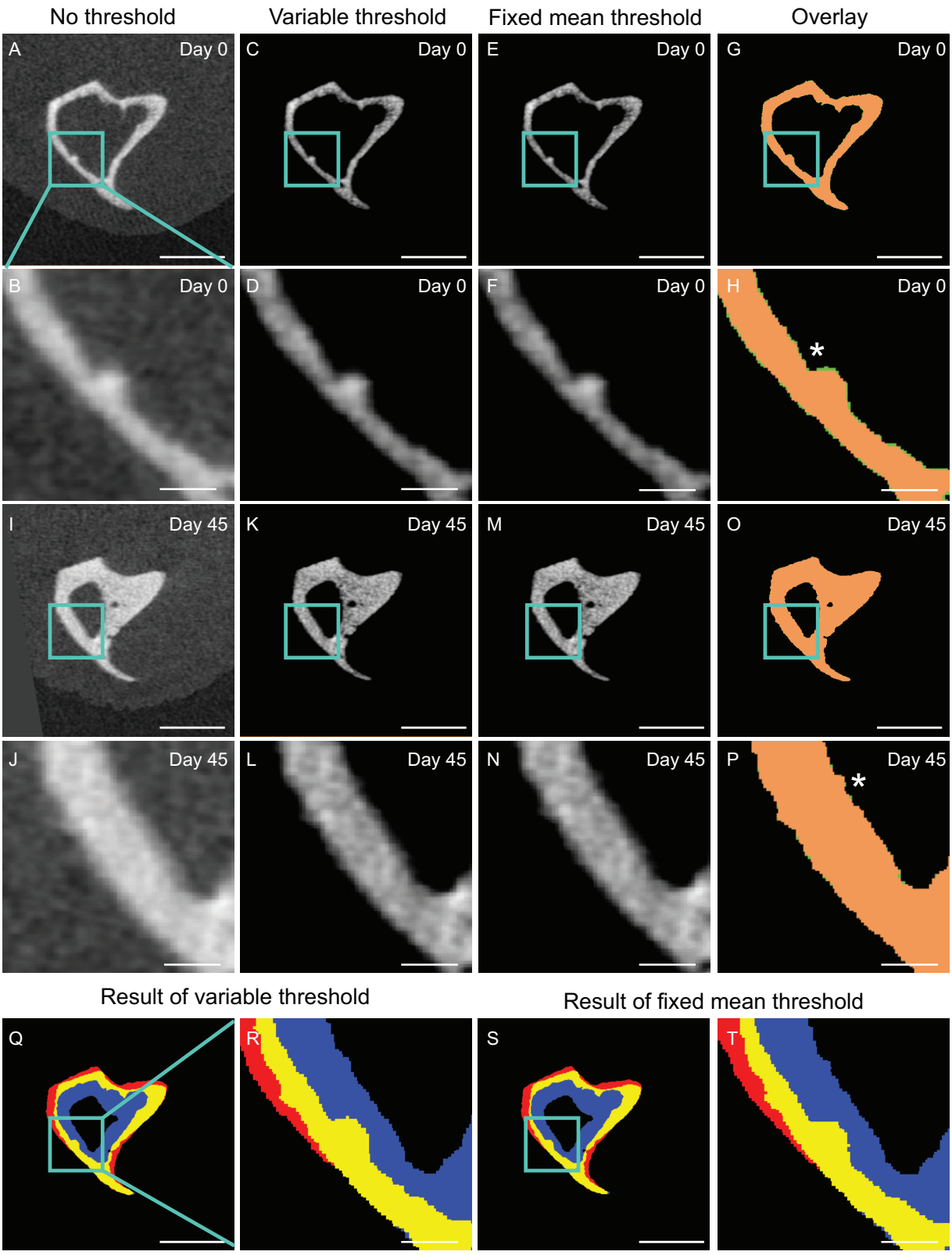

Fig. B.1

Fig. B.1: **The influence of different threshold approaches on the results of bone (re)modeling.** All images show the same section of the proximal tibia with only cortical bone. The tibia at day 0 is shown in A-H with no threshold in (A) and a close up in (B), variable threshold in (C) and a close up in (D), fixed mean threshold in (E) and a close up in (F), as well as an overlay of variable vs. fixed mean thresholds in (G) and a close up in (H), with overlapping voxels shown in orange and non-overlapping voxels in green (asterisk indicates an area with many non-overlapping voxels). The tibia at day 45 is shown in I-P with no threshold in (I) and a close up in (J), variable threshold in (K) and a close up in (L), fixed mean threshold in (M) and a close up in (N), as well as an overlay of variable vs. fixed mean thresholds in (O) and a close up in (P), with overlapping voxels shown in orange and non-overlapping voxels in green (asterisk indicates an area with many non-overlapping voxels). The results of the bone (re)modeling evaluation with variable threshold are depicted in (Q) and a close up in (R) and for a fixed mean threshold in (S) and a close up in (T), with mineralized bone in blue, eroded bone in red and constant bone in yellow. (Scale bars correspond to 1 mm for overview images and 0.2 mm for close up images.) [105]

B.1.1 Threshold per animal and time point

Tab. B.1: 3D-Otsu defined thresholds used for the left tibia ROI for each control animal and time point

Animal / Day	0	17	20	24	27	31	34	38	41	45
1	1958	1969	1787	2126	2101	2238	2153	2245	2261	2320
2	1986	2131	2178	2138	2260	2219	2332	2310	2274	2406
3	2067	2145	2158	2173	2179	2298	2407	2495	2476	2463
4	2020	2081	2154	2040	2251	2271	2351	2427	2377	2437
5	1797	1952	1971	2058	1933	2077	2231	2287	2284	2384
6	1942	2062	2108	2060	2166	2184	2222	2335	2352	2342
7	1843	2018	1990	2054	2058	2089	2158	2245	2281	2264

Tab. B.2: 3D-Otsu defined thresholds used for the right tibia ROI for each control animal and time point

Animal / Day	0	17	20	24	27	31	34	38	41	45
1	1871	2071	2103	2173	2109	2269	2206	2247	2210	2276
2	1921	2101	1986	2199	2266	2195	2201	2241	2239	2396
3	2165	2072	2242	2275	2278	2327	2430	2449	2497	2456
4	2009	2142	2159	2230	2302	2319	2372	2410	2375	2497
5	1917	2008	1998	2066	2039	2125	2227	2300	2231	2379
6	1959	2152	2134	1989	2198	2218	2262	2337	2315	2333
7	1816	2070	2064	2072	2096	2127	2231	2213	2209	2344

Tab. B.3: 3D-Otsu defined thresholds used for the left femur ROI for each control animal and time point

Animal / Day	0	17	20	24	27	31	34	38	41	45
1	2276	2216	2196	2351	2202	2253	2177	2253	2321	2413
2	2101	2188	2205	2265	2270	2191	2307	2332	2460	2432
3	2080	2212	2261	2326	2342	2403	2407	2482	2559	2458
4	2076	2183	2225	2073	2311	2292	2338	2432	2395	2471
5	1957	2081	2146	2218	2205	2246	2330	2399	2430	2461
6	1931	2116	2134	2110	2227	2257	2300	2334	2334	2369
7	1935	2122	2156	2186	2255	2244	2325	2317	2361	2447

Tab. B.4: 3D-Otsu defined thresholds used for the right femur ROI for each control animal and time point

Animal / Day	0	17	20	24	27	31	34	38	41	45
1	2099	2185	2207	2274	2241	2438	2328	2353	2377	2455
2	2016	2148	2060	2310	2290	2237	2358	2308	2403	2503
3	2139	2217	2287	2408	2378	2438	2474	2499	2618	2476
4	2075	2233	2334	2273	2369	2305	2394	2382	2451	2520
5	2009	2031	2121	2235	2272	2196	2259	2293	2379	2532
6	1976	2152	2213	2028	2237	2257	2293	2322	2327	2386
7	1896	2110	2168	2194	2274	2294	2287	2342	2340	2544

Tab. B.5: 3D-Otsu defined thresholds used for the left tibia ROI for each tumor animal and time point

Animal / Day	0	17	20	24	27	31	34	38
1	2023	2091	1991	2139	2177	2188	2149	
2	2057	2205	2121	2280	2369			
3	2038	2161	2187	2148	2223			
4	2082	2075	2179					
5	2030	2176						
6	1834	2053						
7	2027	2035	2097	2153	2204	2183	2196	
8	1918	1926	1943	2010	2036	2078	2149	
9	1953	2036	2134	2183				
10	2104	2113						
11	1854	1927	1968	2037	1993	2103	2139	2170

Tab. B.6: 3D-Otsu defined thresholds used for the right tibia ROI for each tumor animal and time point

Animal / Day	0	17	20	24	27	31	34	38
1	2089	2127	2089	2237	2246	2211	2297	
2	2088	2138	2131	2260	2308			
3	2071	2195	2234	2188	2121			
4	2069	2032	2200					
5	1993	1866						
6	1997	2065						
7	2018	2087	2068	2042	2196	2156	2207	
8	1932	1911	2005	2084	2054	2100	2131	
9	1922	2066	2146	2157				
10	2139	2182						
11	1917	1872	2024	2082	2075	2177	2177	2199

Tab. B.7: 3D-Otsu defined thresholds used for the left femur ROI for each tumor animal and time point

Animal / Day	0	17	20	24	27	31	34	38
1	2109	2162	2160	2255	2277	2251	2289	
2	2175	2346	2279	2352	2433			
3	2106	2246	2286	2304	2356			
4	2029	2196	2279					
5	2052	2243						
6	1970	2201						
7	2048	2146	2263	2259	2304	2290	2311	
8	2003	2043	2135	2225	2208	2222	2329	
9	2113	2275	2221	2290				
10	2228	2233						
11	1973	2088	2169	2233	2152	2243	2284	2299

Tab. B.8: 3D-Otsu defined thresholds used for the right femur ROI for each tumor animal and time point

Animal / Day	0	17	20	24	27	31	34	38
1	2083	2215	2177	2297	2361	2338	2392	
2	2183	2341	2298	2375	2401			
3	2137	2203	2369	2318	2355			
4	2032	2241	2298					
5	2017	2066						
6	1985	2174						
7	2036	2121	2217	2240	2281	2230	2294	
8	1958	2056	2179	2147	2190	2274	2350	
9	1997	2198	2188	2225				
10	2172	2300						
11	1930	2047	2107	2161	2139	2260	2259	2279

B.2 Reproducibility of image processing

All possible combinations of registration, $(n-1)!$ with n being the number of scans were performed. We then calculated mean, standard deviation (SD), precision error (PE) as absolute value (PE_{SD}) and as coefficient of variation (PE_{CV} in %) as well as confidence interval (CI) (using a chi-squared distribution, with df as the total degrees of freedom) for both cortical and trabecular bone volume and surface.

Tab. B.9: Validation data of the registration and segmentation process for the metaphysis, showing the matching of bone volume (BV) and bone surface (BS) for cortical and trabecular bone respectively. 6 bones x 4 scans; 36 registrations; df = 30. [105]

	Mean ± SD	PE_{SD}	PE_{CV}	$CI_{95\%PE,SD}$
ΔBV (Cortical)	3.14 ± 1.40 %	0.397	13.04 %	0.34 – 0.60
ΔBS (Cortical)	11.51 ± 4.63 %	1.463	12.77 %	1.26 – 2.21
ΔBV (Trabecular)	5.30 ± 2.22 %	0.904	15.93 %	0.78 – 1.37
ΔBS (Trabecular)	10.78 ± 4.23 %	1.704	15.31 %	1.46 – 2.58

Tab. B.10: Validation data of the registration and segmentation process for the epiphysis, showing the matching of bone volume (BV) and bone surface (BS) for cortical and trabecular bone respectively. 6 bones x 4 scans; 36 registrations; df = 30. [105]

	Mean ± SD	PE_{SD}	PE_{CV}	$CI_{95\%PE,SD}$
ΔBV (Cortical)	2.52 ± 0.98 %	0.359	13.53 %	0.31 – 0.54
ΔBS (Cortical)	13.24 ± 5.07 %	1.627	11.97 %	1.40 – 2.46
ΔBV (Trabecular)	3.56 ± 1.41 %	0.685	17.55 %	0.59 – 1.04
ΔBS (Trabecular)	11.11 ± 4.34 %	1.872	15.84 %	1.61 – 2.83

APPENDIX C

Static microcomputed tomography-based morphometry for physiological bone (re)modeling

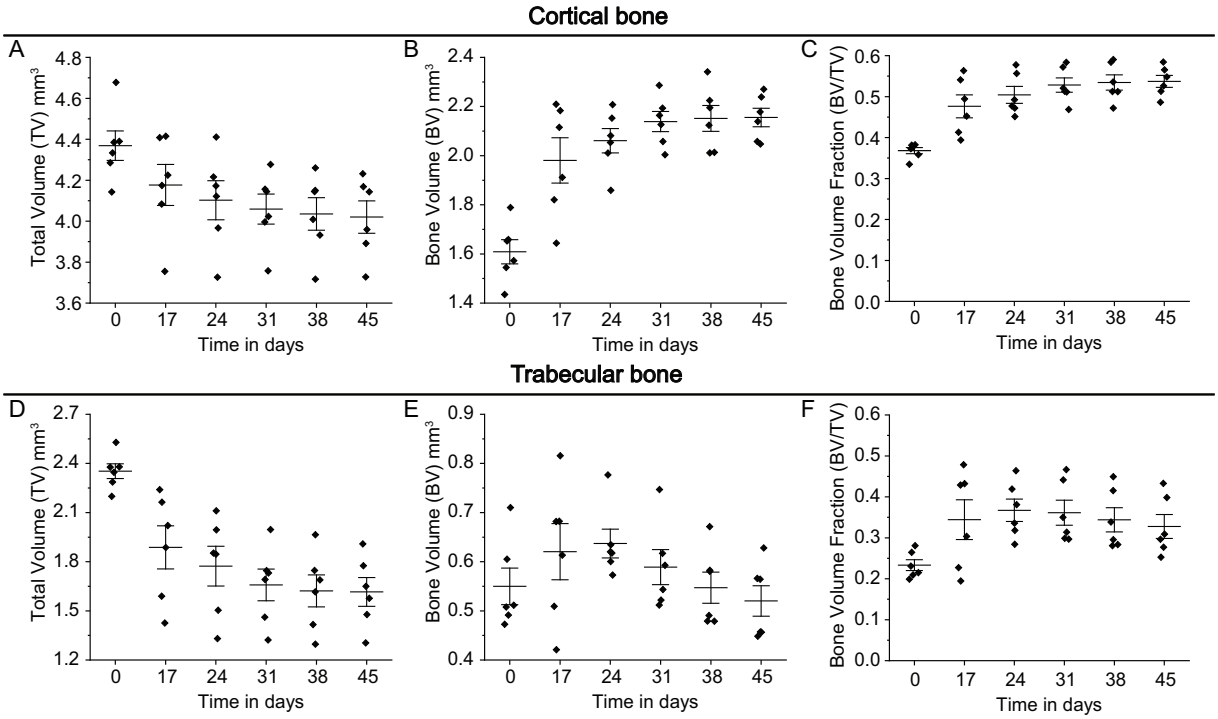

Fig. C.1: **Spatial evaluation of gradients in bone (re)modeling of femur and tibia reveals significant differences in mineralized regions.** Shown are for cortical bone (A) total volume, (B) bone volume and (C) bone volume fraction over time; for trabecular bone (D) total volume, (E) bone volume and (F) bone volume fraction over time. (N = 6 bones from six control animals.) [105]

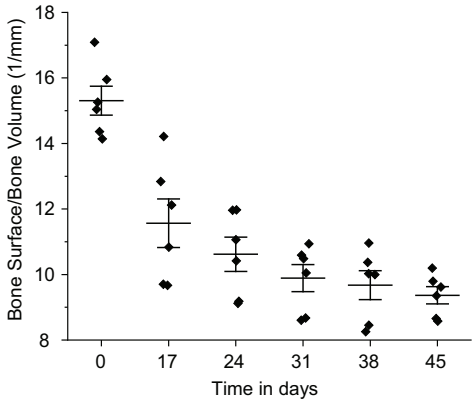

Fig. C.2: **Static microCT analysis of the tibial proximal metaphysis bone surface over bone volume in cortical bone over time.** (N = 6 bones from six control animals.) [105]

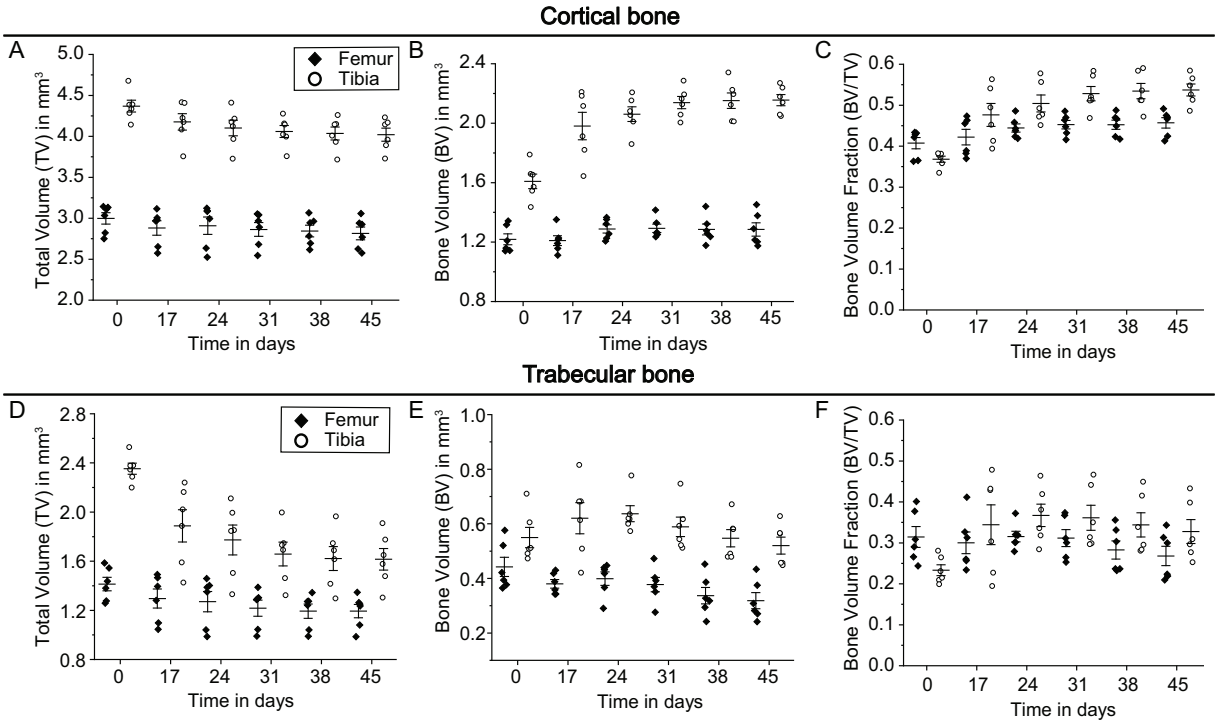

Fig. C.3: **Static microCT analysis for the tibial proximal metaphysis and the femoral distal metaphysis over time for cortical and trabecular bone.** Shown are for cortical bone (A) total volume, (B) bone volume and (C) bone volume fraction over time; for trabecular bone (D) total volume, (E) bone volume and (F) bone volume fraction over time for femur (diamond) and tibia (empty circle). (N = 6 bones from six control animals.) [105]

APPENDIX D

Bone (re)modeling after cancer cell injection in cortical bone

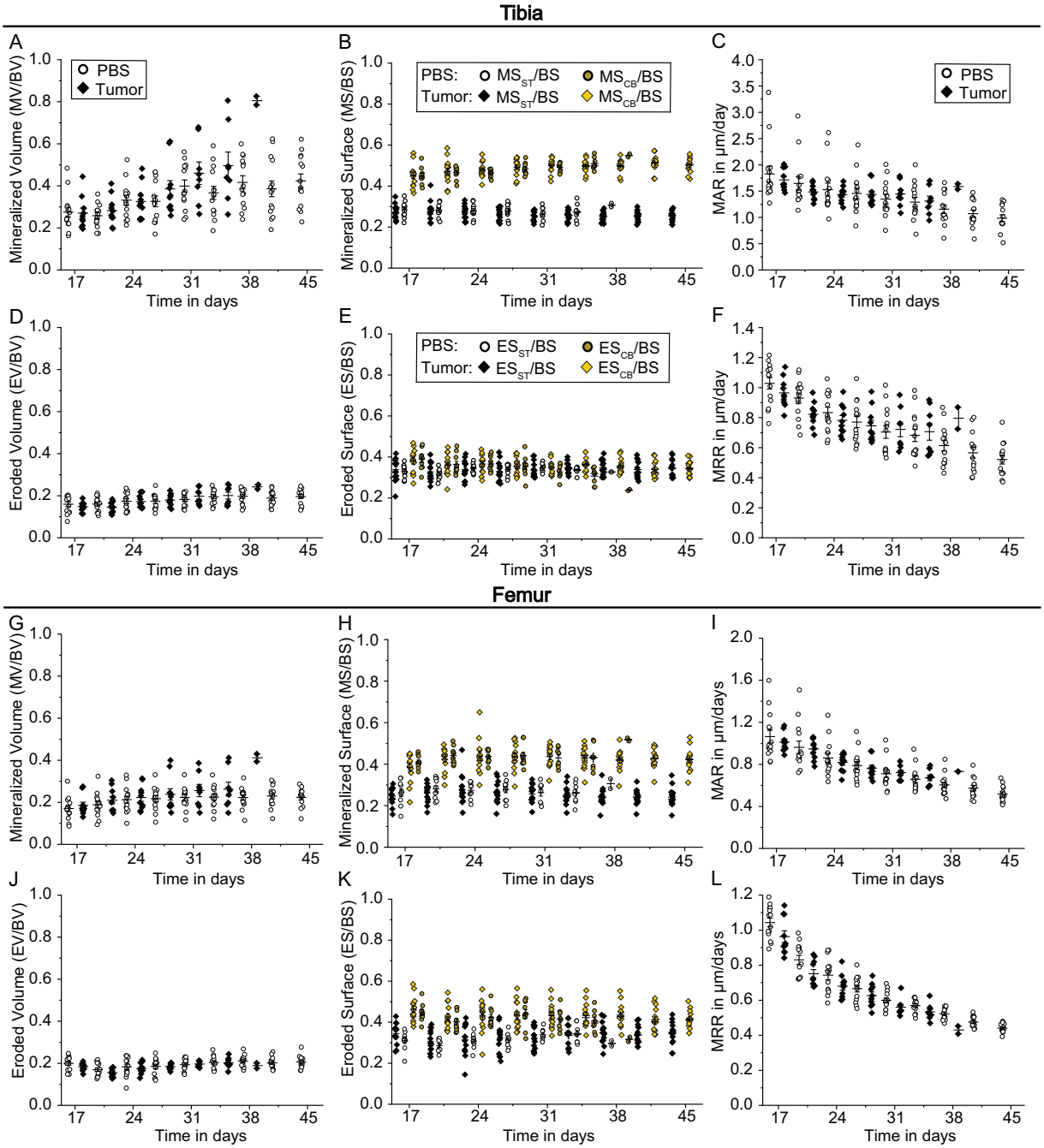

Fig. D.1: **Bone (re)modeling analysis of animals injected with cancer cells (without detectable osteolytic lesions) in comparison to healthy control animals in trabecular bone.** Results in cortical bone of tibial proximal metaphysis are shown for (A) MV/BV, (B) MS/BS and (C) MAR, as well as (D) EV/BV, (E) ES/BS and (F) MRR. Results of bone (re)modeling analysis in cortical bone of the femoral distal metaphysis. Shown are (G) MV/BV, (H) MS/BS and (I) MAR, as well as (J) EV/BV, (K) ES/BS and (L) MRR. (All plots show mean and standard deviation. PBS animals: N = 14 bones from seven animals, Tumor: N = 10 bones from five animals for tibia and femur respectively.)

APPENDIX E

Pilot animal with large osteolytic lesion

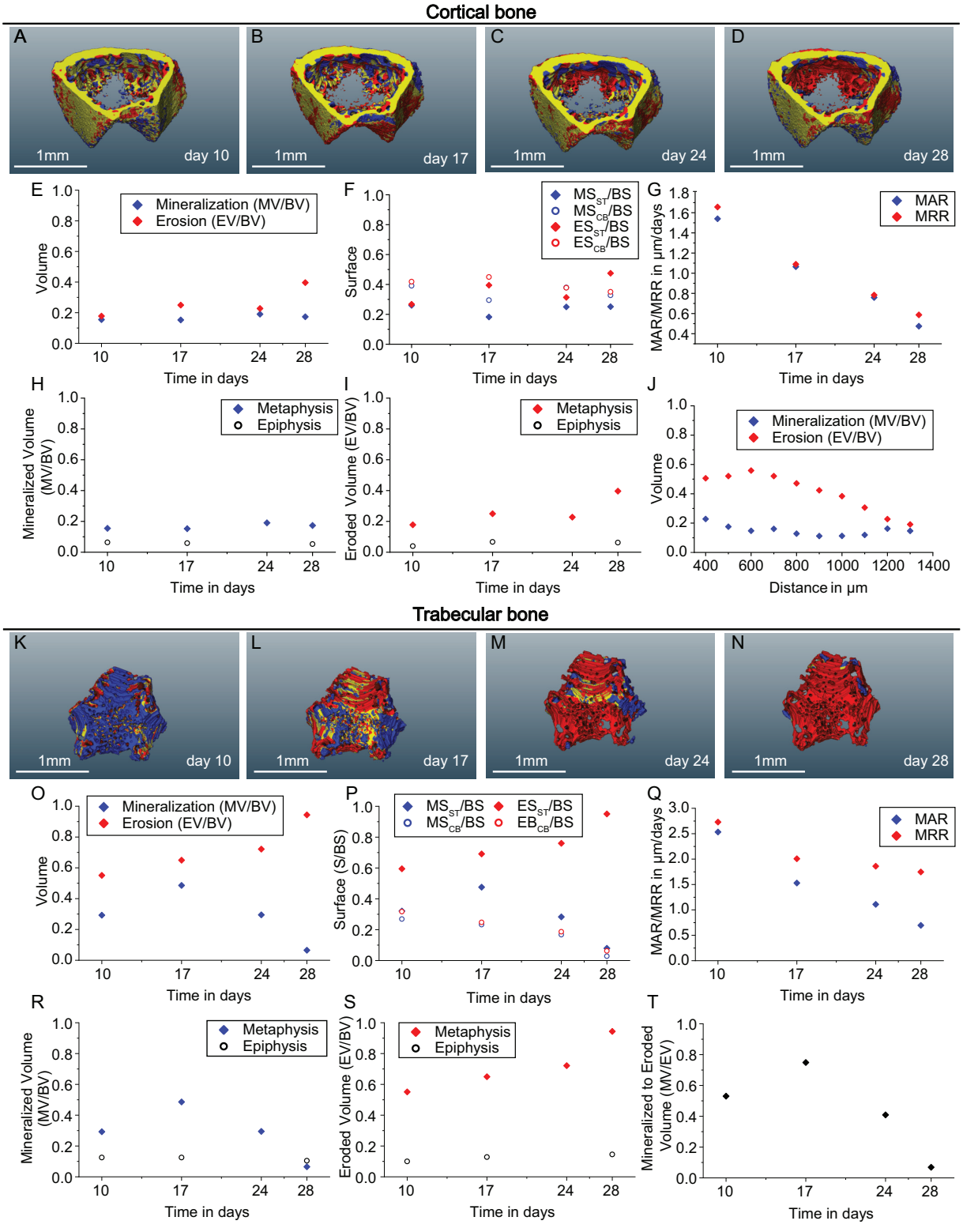
Cortical bone
A
B
C
D
1mm
day 10
day 17
day 24
day 28
E
Mineralization (MV/BV)
Erosion (EV/BV)
Volume
Time in days
F
MS_ST/BS
MS_CB/BS
ES_ST/BS
ES_CB/BS
Surface
G
MAR
MRR
MAR/MRR in µm/days
H
Metaphysis
Epiphysis
Mineralized Volume (MV/BV)
I
Eroded Volume (EV/BV)
J
Distance in µm
Trabecular bone
K
L
M
N
O
P
EB_CB/BS
Surface (S/BS)
Q
R
S
T
Mineralized to Eroded Volume (MV/EV)

Fig. E.1

Fig. E.1: **Bone (re)modeling in a pilot animal with a breast cancer metastatic osteolytic event in the distal femoral metaphysis.**Evaluation of bone (re)modeling of cortical bone at (A) day 10, (B) day 17, (C) day 24 and (D) day 28. Shown are normalized (E) volume, (F) surfaces (soft tissue interface as diamond and constant bone interface as empty circle) and (G) MAR/MRR over time with mineralization in blue and erosion in red. Comparison of metaphysis (diamond) and epiphysis (empty circle) for normalized (H) mineralized (blue) and (I) eroded (red) volume, as well as (J) spatial volume analysis of 100 µm sections with mineralization in blue and erosion in red. Evaluation of bone (re)modeling of trabecular bone at (K) day 10, (L) day 17, (M) day 24 and (N) day 28. Shown are normalized (O) volume, (P) surfaces (soft tissue interface as diamond and constant bone interface as empty circle) and (Q) MAR/MRR over time with mineralization in blue and erosion in red. Comparison of metaphysis (diamond) and epiphysis (empty circle) for normalized (R) mineralized (blue) and (S) eroded (red) volume, as well as (T) a ratio of mineralized and eroded volume. (For interpretation of the references to color in this figure legend, the reader is referred to the web version of this article.) [105]
For methodological details, please refer to the paper by Young et al. [105]

APPENDIX F

Cancer cell analysis in the bone marrow

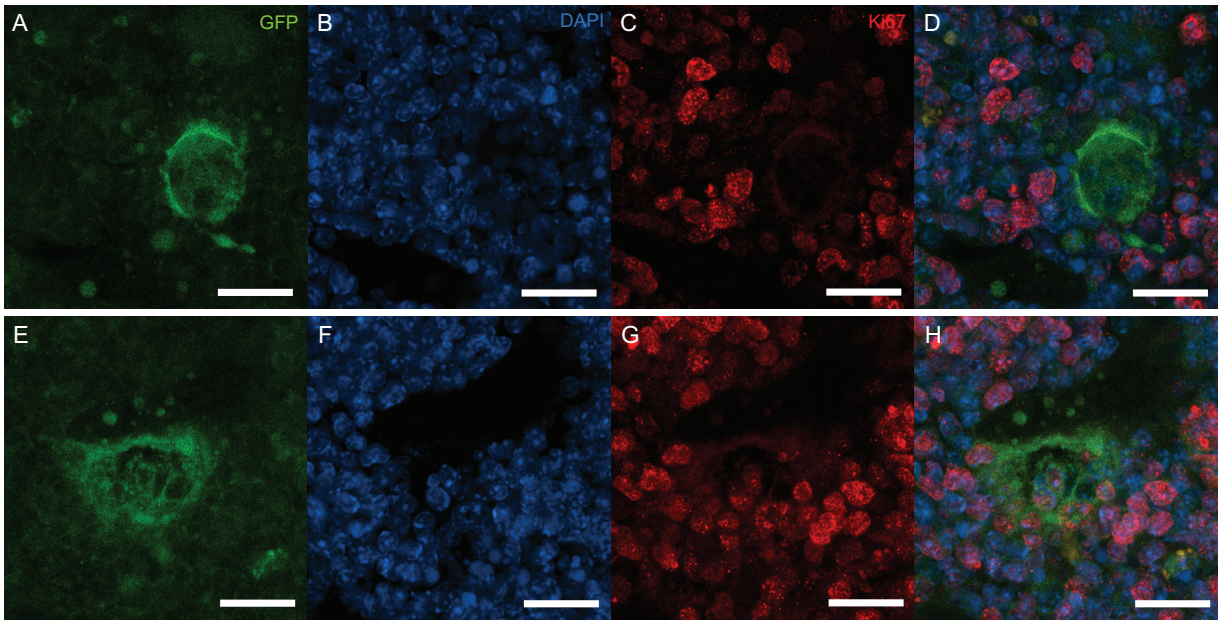

Fig. F.1: **Different proliferation status of cancer cell clusters in the bone marrow (Ki67).** (A) eGFP labeled cancer cell cluster in the bone marrow (green), (B) with corresponding nuclear DAPI signal (blue) and (C) corresponding nuclear Ki67 signal (red). (D) Overlap of all three signals showing a Ki67 negative cancer cell cluster. (E) eGFP labeled cancer cell cluster in the bone marrow (green), (F) with corresponding nuclear DAPI signal (blue) and (G) corresponding nuclear Ki67 signal (red). (H) Overlap of all three signals showing a Ki67 positive cancer cell cluster. (Scale bar corresponds to 20 µm. N = 4 bones form four tumor animals, representative images from animal 3.)

APPENDIX G

Influence of the osteolytic lesion on the biophysical microenvironment

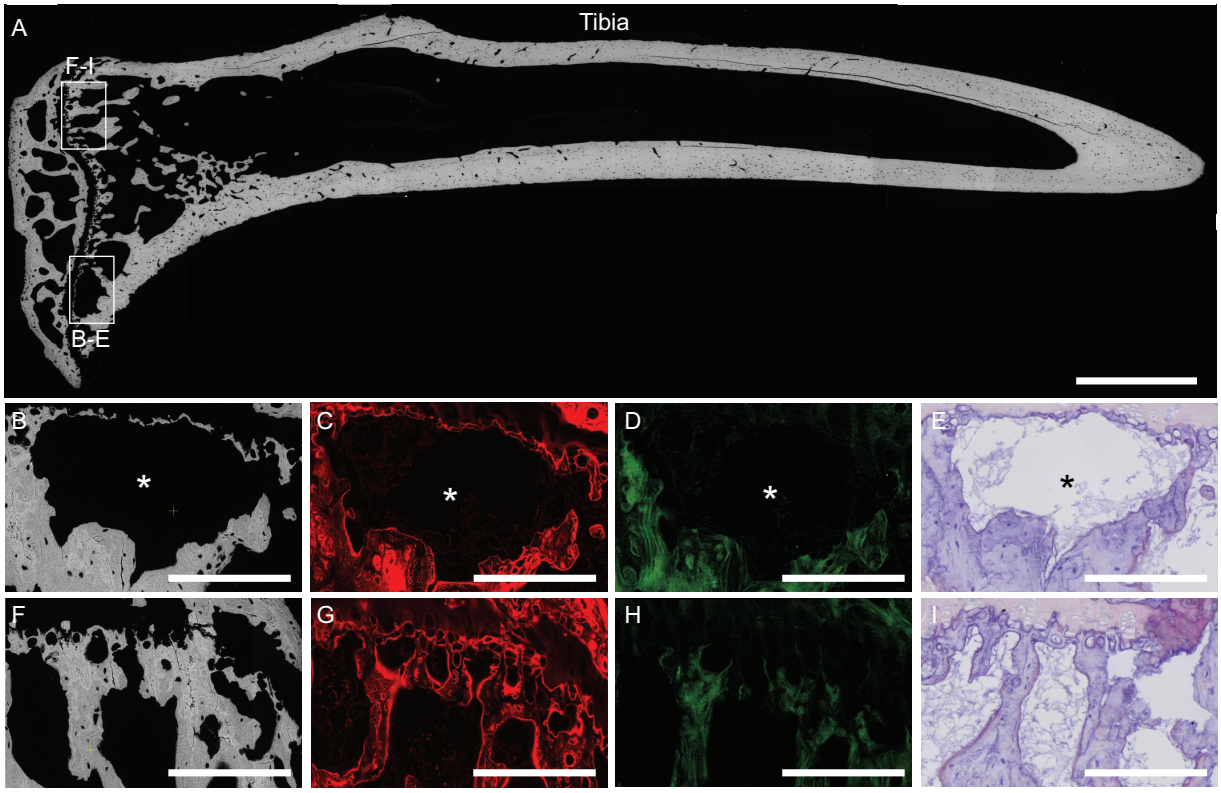

***Fig. G.1: Ex vivo* characterization of a trabecular lesion and comparison to healthy tissue in the same bone.** (A) Overview BSE microscopy image of a tibia with (B) enlargement of a trabecular lesion, as well as (C) CLSM (rhodamine staining), (D) SHG imaging of collagen fibers and (E) H&E stain. (F) BSE microscopy enlargement of a healthy trabecular region, as well as (G) CLSM (rhodamine staining), (H) SHG imaging of collagen fibers and (I) H&E stain. (Asterisk indicates the presence of a lesion, scale bars correspond to 1 mm and 200 µm in the enlargements. N = 5 bones from five tumor animals containing an osteolytic lesion, representative images from animal 2.)